The Relationship Between Flagellar Motor Dynamics and the Proton Motive Force

Murray John Tipping

A thesis submitted in partial fulfillment of
the requirements for the degree of
Doctor of Philosophy at the University of Oxford



Merton College
University of Oxford
Trinity Term 2011

Abstract

The Relationship Between Flagellar Motor Dynamics and the Proton Motive Force

Murray J. Tipping

Thesis submitted for the degree of Doctor of Philosophy,
University of Oxford, Trinity Term 2011

The bacterial flagellar motor is one of the few rotary motors found in nature, and an excellent example of a complex molecular machine. Flagellar motors in the model organism *Escherichia coli* are products of the coordinated expression of ∼50 different genes. The *E. coli* flagellar motor is powered by the proton-motive force (*pmf*), an electrochemical gradient across the cell membrane. Motor torque is generated by proton flow through membrane-embedded stator units which bind to the basal body of the motor.

This thesis aimed to investigate the relationship between the *pmf* and the flagellar motor. A novel *pmf* control system was developed, based on the light-driven proton pump proteorhodopsin (pR). This system enabled *pmf*-dependent changes in motor behaviour to be precisely monitored *in vivo*. Expression of pR in *E. coli* was shown to be sufficient to drive the flagellar motor at wild-type speeds. Using the pR-based *pmf* control system, the motor was shown to respond to changes in *pmf* on a timescale of milliseconds. Surprisingly, motor speed increase was observed when *pmf* was increased above the physiological norm. Reduction of *pmf* to low levels enabled individual steps in motor rotation to be observed.

Motor response to loss of *pmf* was investigated. Motors were shown to exhibit a two-stage speed decrease after disruption of *pmf*, with motor speed falling to ∼20 % of its initial value within milliseconds, reaching a complete stop after 1 s. Extended periods of *pmf* loss was shown to lead to disengagement of stators from the motor, with motor speed increasing in a stepwise fashion after *pmf* restoration.

The integrity of the motor at different *pmf* levels was investigated by using TIRF microscopy to directly image positioning of fluorescently tagged motor components. The stator protein MotB was shown to physically leave and rejoin the motor after *pmf* disruption and restoration, with MotB dispersal following motor stop.

Declaration

The work in this thesis was undertaken at the University of Oxford; in the Microbiology Unit, Department of Biochemistry and in the Clarendon Laboratory, Department of Physics. Work was performed from October 2007 to September 2011 under the supervision of Prof. J.P. Armitage. All the work in this thesis is my own unless stated and has not been submitted for a degree at this or any other university.

Publications

M.J. Tipping, N.S. Delalez, R.M. Berry and J.P. Armitage, *Stator stability and proton motive force in the E. coli flagellar motor*, In preparation.

Acknowledgements

Firstly, thank you to Prof Judith Armitage for giving me the opportunity and the freedom to work on such a fascinating project. Thanks must also go to Dr Richard Berry for his invaluable advice and support.

I'd like to thank all the past and present members of both labs – not only for all their help during the last four years, but also for making the DPhil experience such a rewarding one. Particular thanks must go to Dr Nicolas Delalez for important help with the fluorescence imaging, and to Dr Teuta Pilizota for all her guidance at the start of the project.

Special thanks go to my mother and sister, who have patiently put up with me through it all, and to Courtney over the water.

Abbreviations

AFM	atomic-force microscopy
Amp^R	ampicillin resistant
AODs	acousto-optical deflectors
ATP	adenosine triphosphate
BFP	back-focal plane
BPR	blue-absorbing proteorhodopsin
bR	bacteriorhodopsin
BSA	bovine serum albumin
c-di-GMP	cyclic-diguanidine monophosphate
CAP	catabolite activator protein
CCCP	carbonyl cyanide 3-chlorophenylhydrazone
CCD	charge-coupled device
CCW	counter-clockwise
CheY-P	phosphorylated CheY
Cm^R	chloramphenicol resistant
CW	clockwise
cyt bo_3	cytochrome bo_3
DIG	dioxygenin
DNA	deoxyribonucleic acid
dNTP	deoxynucleoside-5'-triphosphate
DSP	digital signal processing
$\Delta\psi$	membrane electrical potential
Δ pH	H^+ chemical gradient
EDTA	ethylenediaminetraacetic acid
eGFP	enhanced GFP
EM	electron microscopy
FCCP	carbonyl cyanide-p-trifluoromethoxyphenylhydrazone
FLIP	fluorescence loss in photobleaching
FRAP	fluorescence recovery after photobleaching
GFP	green fluorescent protein
GMP	guanidine monophosphate
GPR	green absorbing proteorhodopsin
imf	ion-motive force
IPTG	isopropyl β-D-thiogalactosidase
LB	Luria-Bertani medium
MCP	methyl-accepting chemotaxis protein
NA	numerical aperture
ND	neutral-density
OD_{600}	optical density at wavelength 600 nm
ω	angular velocity

PCR	polymerase chain reaction
pmf	proton-motive force
pR	proteorhodopsin
smf	sodium-motive force
SOB	super optimal broth with catabolite repression
SOC	super optimal broth
$\mathrm{Suc}^{\mathrm{R}}$	sucrose resistance
TB	tryptone broth
TBE	Tris-borate-EDTA
TFB	Transformation buffer
TIRF	total internal reflection fluorescence
TMRM	tetramethyl rhodamine methyl ester
Tris	tris(hydroxymethyl)aminomethane
θ	angle
UV	ultraviolet
w.t.	wild-type

for my father

Contents

1 Introduction **1**

1.1 Prokaryotic Motility . . . 1
1.1.1 Why is Motility Important? . . . 1
1.1.2 Motility Systems . . . 3
1.2 Chemotaxis in *E. coli* . . . 6
1.2.1 The *E. coli* Chemotaxis System . . . 6
1.3 The Bacterial Flagellar Motor . . . 9
1.3.1 Flagellar Assembly . . . 11
1.3.2 Export Apparatus . . . 12
1.3.3 Flagellar Filament and Hook . . . 13
1.3.4 The Basal Body . . . 15
1.3.5 The Switch Complex . . . 15
1.3.6 Stators . . . 17
1.4 Torque Generation and Switching in the Flagellar Motor 19
1.4.1 The Rotor/Stator Interface . . . 19
1.4.2 Motor Rotation . . . 20
1.4.3 The Torque/Speed Curve of the Flagellar Motor . 20
1.4.4 Theoretical Models for Motor Rotation . . . 22
1.4.5 Motor Switching . . . 22
1.5 Motor Dynamics . . . 23
1.5.1 Motor Resurrection . . . 23
1.5.2 Turnover of Motor Components . . . 24
1.5.3 The Relationship between Motors and the *imf* . . . 24
1.6 *E. coli* Bioenergetics . . . 27
1.6.1 The Proton Motive Force . . . 27
1.6.2 Methods of *pmf* Production in *E. coli* . . . 29
1.7 Proteorhodopsin . . . 30
1.7.1 Discovery and Diversity . . . 30
1.7.2 Mechanism of Proton Pumping . . . 31
1.7.3 Utilities . . . 32
1.8 Experimental Techniques . . . 33
1.8.1 Measuring Motor Rotation . . . 33
1.8.2 Fluorescence Microscopy . . . 34

1.8.3 Fluorescent Proteins . . . 36
1.8.4 Total Internal Reflection Fluorescence (TIRF) Microscopy . . . 37
1.9 Aims of This Study . . . 38

2 Materials and Methods 39
2.1 Strains and Plasmids . . . 40
2.1.1 Bacterial Growth Conditions . . . 40
2.1.2 Storage of Strains . . . 41
2.2 Genetic Techniques . . . 41
2.2.1 DNA Manipulation . . . 41
2.2.2 Transforming *E. coli* . . . 44
2.2.3 Gene Replacement with pDS132 . . . 45
2.3 Phenotypic Analysis of *E. coli* Strains . . . 46
2.3.1 Soft Agar Swim Plates . . . 46
2.3.2 Preparing Cells for Microscopy . . . 46
2.4 Microscopy . . . 49
2.4.1 TIRF Microscopy . . . 49
2.4.2 Microscopy and BFP Interferometry of Attached Beads . . . 50
2.4.3 Data Analysis . . . 50

3 Development of a pR-Based Motor Assay 53
3.1 Aims . . . 54
3.2 Construction of Strains . . . 55
3.2.1 Reconstruction of Plasmid pDS-*fliC*st . . . 56
3.2.2 Incorporation of pDS-*fliC*st onto the Genome . . . 56
3.2.3 Phenotypic Characterisation of Strains MT02 and MT03 . . . 58
3.2.4 Expression of pR in Experimental Strains . . . 60
3.3 Light-Powering of *E. coli* . . . 61
3.3.1 Inhibiting *pmf* Generation in *E. coli* . . . 61
3.3.2 A pR-Based Cell Assay . . . 62
3.4 Conclusions . . . 64

4 Motor Control with pR 66
4.1 Aims . . . 67
4.2 Effects of Light-Powering *E. coli* Cells . . . 67
4.3 Effects of Different Illumination Levels on the Motor . . . 69
4.4 Investigating the Stepping Action of the *E. coli* Motor . . . 72
4.5 Discussion . . . 75

5 Resurrection Studies of Wild-Type *E. coli* Motors 77
5.1 The Effects of *pmf* Loss on the Flagellar Motor . . . 78
5.1.1 Characterising The Effects of *pmf* Loss on the Motor . . . 78

5.1.2 Time at Zero *pmf*: Effects on the Motor 81
5.2 Motor Resurrection in De-Energised *E. coli* 84
5.3 Discussion 87

6 Visualising Motor Integrity **89**
6.1 Aims 90
6.2 Strain Construction 90
6.2.1 Construction and Testing of Strains MT04 and MT05 91
6.2.2 Construction and Testing of Strain MT06 93
6.3 Motor Integrity and *pmf* 96
6.3.1 Adaptation of the pR System for Fluorescence Microscopy 96
6.3.2 Analysis of MT04 Motor Integrity 97
6.3.3 Analysis of MT05 Motor Integrity 99
6.4 Conclusions 102

7 Discussion and Future Work **104**

Bibliography **108**

A Appendix - Media Recipes and Reagents **126**

B Appendix - Primer Sequences **129**

C Appendix - Supplementary Data **131**

Chapter 1

Introduction

> "... and the whole water seemed to be alive with the multitudinous animalcules. For me this was among all the marvels that I have discovered in nature the most marvellous of all, and I must say that, for my part, no more pleasant sight has yet met my eye than this of so many thousands of living creatures in one small drop of water, all huddling and moving, but each creature having its own motion."
>
> *Antoine van Leeuwenhoek, letter to H. Oldenburg, 1676*

A typical bacterium is only a couple of micrometres long. How can such minuscule creatures be capable of concerted motion? This thesis investigates an ingenious bacterial solution to the problem of microscopic motility – the bacterial flagellar motor. Comprising only protein, which interact with the cell wall and inner and outer membranes, it is able to convert an electrochemical potential difference across a cell membrane into useful mechanical work. This intricate molecular machine is therefore one of the few electric motors found in nature. In this work, I explore the relationship between the *Escherichia coli* flagellar motor and the ion-motive force which drives it.

1.1 Prokaryotic Motility

1.1.1 Why is Motility Important?

Many bacteria have the ability to detect changes in their environment, and are able to react to those changes by moving to conditions which are more favourable to

growth. This ability is known as taxis, and is a response to many different stimuli, such as light (phototaxis), magnetic fields (magnetotaxis) or chemical gradients (chemotaxis). Whatever the stimulus, taxis is ultimately dependent on motility – the ability of bacteria to navigate around their surroundings. Different species have evolved different methods of moving around; the most common is to swim using one or more flagella, but several other methods have been observed.

Bacterial motility plays a key role in many interactions between bacteria, the environment, and other organisms. *Helicobacter pylori* is a prevalent human pathogen which is present in the stomachs of ∼50 % of people worldwide, capable of causing gastric ulcers and increasing the risk of gastric cancer. Non-motile and non-chemotactic *H. pylori* mutants display much reduced colonisation ability, and are unable to compete against their wild-type counterparts [108]. Motility has been implicated as an aid to virulence in several other pathogens, such as *Vibrio cholerae, Salmonella enterica* and *Legionella pneumophila* [64].

More benignly, motility can be important in establishing symbiotic relationships. One example is nodule formation in legumes, one of the most successful families of flowering plants [40]. These nodules provide an ideal environment for nitrogen-fixing bacteria, providing carbon sources and minimising oxygen levels [33],and releasing chemotactic attractants to encourage symbiosis. Non-chemotactic and non-motile mutants of bacterial species such as *Rhizobium leguminosarum* are unable to spontaneously initiate root nodule colonisation [99], and so cannot take advantage of the symbiotic opportunity.

The presence of flagella also closely associated with biofilm formation in many bacteria. Biofilms are natural aggregates of bacteria which form on solid surfaces, and are commonly found in many natural, clinical and industrial environments [61]. In *E. coli*, aflagellate mutants are markedly poorer at forming biofilms [164], and motility is necessary for biofilm formation in many species such as *Agrobacterium tumefaciens* [98].

The importance of chemotaxis and motility in so many different areas has led to intense study of these phenomena in many species. The chemotactic pathway of *E. coli* and its regulated flagellar motor have been especially well-characterised. [123] However, several puzzling questions still remain unanswered. The *E. coli* flagellar motor seems to be in constant flux, with several component proteins undergoing constant turnover [36] [79]. Why this should be so is unclear. The exact mechanism of torque generation – how proton translocation translates to rotary motion – is also unknown, although several models have been developed [165] [94].

1.1.2 Motility Systems

Microbes have evolved several ways to move around their environment. Gliding is used by bacteria to travel across solid surfaces, while swimming through a liquid medium is typically done using one or more flagella, powered by flagellar motors. Although superficially similar, the bacterial and archaeal flagella are quite different in operation. The comparatively poorly-understood archaeal system is described here along with twitching and gliding motility, while the bacterial flagellar motor is described in more detail in a later section. A general overview of motility can be found at [62].

Twitching Motility

The term "gliding motility" refers to several methods evolved by bacteria to move along solid surfaces. The most widespread seems to be "twitching" motility (also known as S-, for social, motility), where movement is achieved by extending and retracting type IV pili at the cell poles. This system, present in many species including *V. cholerae, Neisseria gonorrhoeae* and *Synechocystis* PCC6803 has been best studied in *Pseudomonas aeruginosa* and *Myxococcus xanthus* [65]. Twitching motility only occurs during cell swarming and is much slower than swimming; typical speeds are 1.5 - 6 μm min^{-1} [146].

The type IV pili required for twitching motility are typically 5 - 7 nm in diameter and can extend to several μm long [92]. Pili are formed from multiple copies of PilA, a protein comprising a long N-terminal α-helix and a C-terminal β-sheet. As pili form, multiple PilA hydrophobic α-helices interact to form coiled coils protected by the β-sheets, creating a strong fibre [32].

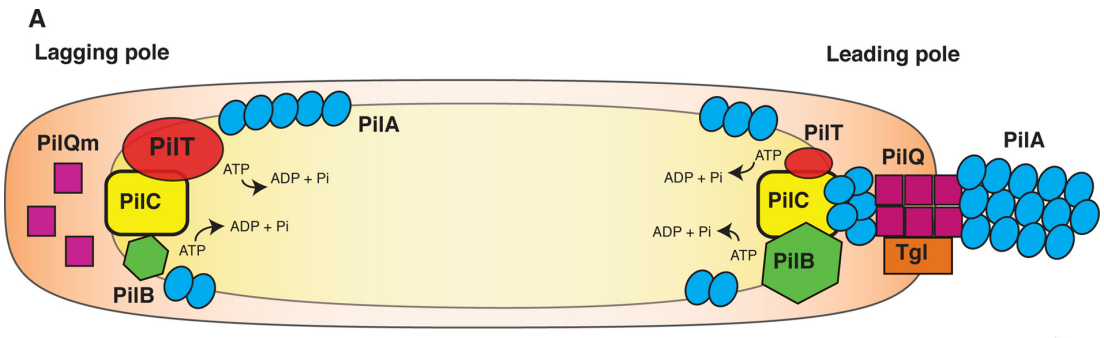


Figure 1.1: A cartoon schematic of the components of the S-motility system. PilB primarily localises to the leading pole, where it catalyses type IV pilus production. PilT localises to the lagging pole and catalyses pilus retraction.Adapted from [93]

Pilus extension and retraction is controlled by an ATP-driven complex. During extension at the leading pole, individual PilA monomers are polymerised by an ATPase, PilB, and translocated outside the cell by PilQ and Tgl lipoprotein. At the lagging pole, pili are retracted by coordinated disassembly by PilT, another ATPase [93]. The adhesin PilC acts as a scaffold for this complex. A schematic of gliding motility can be seen in Figure 1.1.

Adventurous Gliding Motility

M. xanthus displays a second form of gliding motility, known as A- (for adventurous) motility. A-motility is required for movement of isolated cells, and requires the concerted expression of ∼40 different genes.

A-motility has been shown to be powered by rotation of a helical structure formed from protein AgmU [105]. This helix is associated with the actin-like protein MreB and loops around the cell body, forming a single "track" around the cell. Rotation of the AgmU helix has been shown to depend on *pmf*; cells treated with the protonophore CCCP do not move, and helix rotation cannot be seen.

Helix rotation seems to be powered by a molecular motor. Two gene pairs, *aglXaglV* and *aglRaglS* have been shown to be essential for A-motility [170]. These proteins are homologous to the torque-generating units of the flagellar motor, MotA and MotB. Based on these data, a model for A-motility has been proposed where helix rotation is driven by individual motors carrying "cargo" proteins. As these cargo molecules move with the helix, they deform the cells wall, generating drag on the cell substrate. High drag causes motors and their cargo to collect in clusters, which appear to generate transverse waves of deformation on the cell as they move [150]. Movement of this transverse wave in a stepping motion is ultimately thought to drive the cell forward.

Other Forms of Gliding Motility

Other forms of gliding motility have been observed in the *Mycoplasma*. *Mycoplasma mobile* is capable of moving at 20 μm s^{-1} using a "centipede" mechanism composed of many protein "legs" which attach and detach to the substratum in an ATP-driven process [103]. The related *Mycoplasma pneumoniae* uses a different, "inchworm" system, where motor proteins cause an attachment organelle to cyclically contract and extend, pushing the cell along [56].

The Archaeal Flagellum

Superficially similar, the archaeal flagellum is in fact unrelated to its bacterial counterpart. Although it comprises a long filament connected to the cell by a hook, and is capable of bidirectional rotary motion [9], the archaeal flagellum is actually more closely related to the type IV pili extension system [106]. A comparison between the two systems can be seen in Figure 1.2. Archaea make use of flagella in several ways, such as swimming [152], surface adhesion [178] and biofilm formation [71].

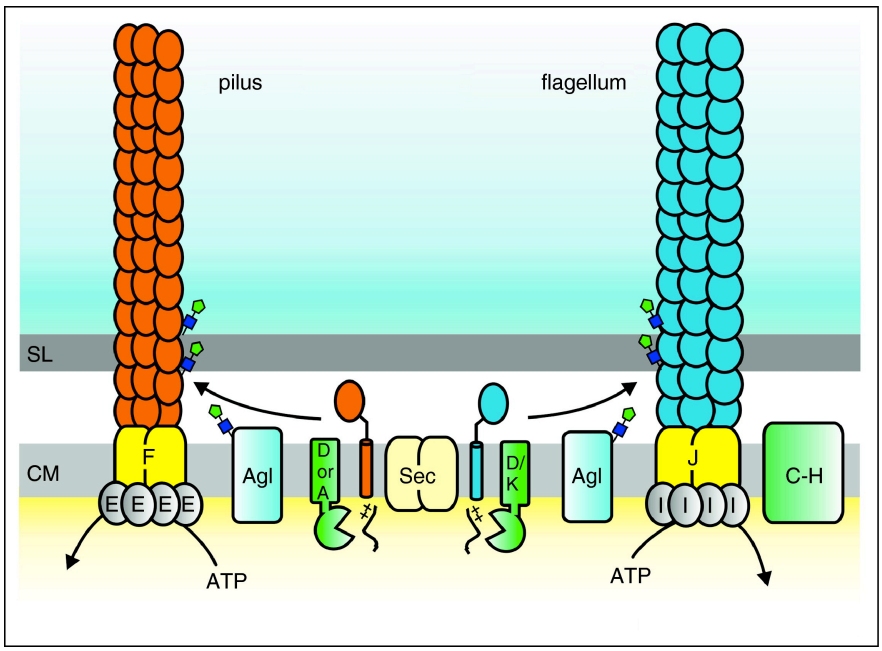


Figure 1.2: A comparison between the components required for synthesis of archaeal flagellar and type IV pili. The Sec pathway transports pre-flagellins and pre-pilins to the cytoplasmic membrane, where they are processed by prepilin peptidases (PibD, FlaK or EppA). Archaeal flagella are N-glycoylated by the archaeal glycosylation machinery (Agl), and incorporated by membrane bound ATPases (E and I) and integral membrane proteins (F and J). Adapted from [121]

Archaeal flagella are constructed, like type IV pili, by extrusion of filaments from the cell body [29][30]. Individual flagellin molecules bear sequence similarity to, and are processed like, bacterial pilins [156]. Unlike bacterial pilins, however, archaeal flagellins often require N-glycosylation for correct assembly [121]. Compared to bacterial flagella, archaeal flagella lack a central channel and are consistently much thinner (10 - 13 nm compared to 20 nm [155][169]).

Very little is known about the method of action of the archaeal flagellar motor. One important finding, and a major difference between the archaeal and bacterial

flagellar motors, is that motor rotation in the archaeon *Halobacterium salinarum* is dependent on the presence of ATP [149]. The flagellar-associated ATPase, FlaI, is proposed to drive flagellar assembly and movement; however, all that is known is that its activity is stimulated by archaeal lipids and its oligomerisation is dependent on ATP [51]

1.2 Chemotaxis in *E. coli*

E. coli has proven to be a useful model organism for many areas of microbiology and molecular biology, and the *E. coli* chemotaxis system has provided the paradigm for biological signal transduction [123]. In chemotaxis, organisms migrate towards favourable chemicals and away from unfavourable chemicals. Microbes the size of a typical *E. coli* cell are unable to detect chemical gradients along their length, so are unable to orient themselves directly. Instead, *E. coli* uses temporal sensing to bias a "random walk" through its environment. Cells compare the concentration of chemicals at any given time to the concentration 3 - 4 s earlier, and respond accordingly [135].

E. coli swims through its environment using 4 - 6 flagella. During a "run" phase, all motors spin counter-clockwise (CCW), and the flagellar filaments come together to form a single bundle. A "tumble" occurs when one or more of the motors switches direction and spins clockwise (CW). This switch causes the flagellar filament to change handedness and wavelength, throwing the bundle apart [157]. Brownian motion then jostles the cell into a new orientation, and a new run begins as the motors revert to CCW rotation. At steady state, runs typically last 1 s, with a mean tumble interval of 0.1 s [20].

The frequency of motor switching is controlled by the chemotaxis pathway. As cells travel in a favourable direction, the chemotaxis system biases swimming to increase run length and suppress direction changing. If cells begin to move in an unfavourable direction, the probability of direction changing increases. A schematic of how this biased random walk corresponds to flagellar bundle formation can be seen in Figure 1.3.

1.2.1 The *E. coli* Chemotaxis System

Compared to other organisms, such as *Rhodobacter sphaeroides*, the *E. coli* chemotaxis system is relatively simple, and provides an excellent model of a two-component

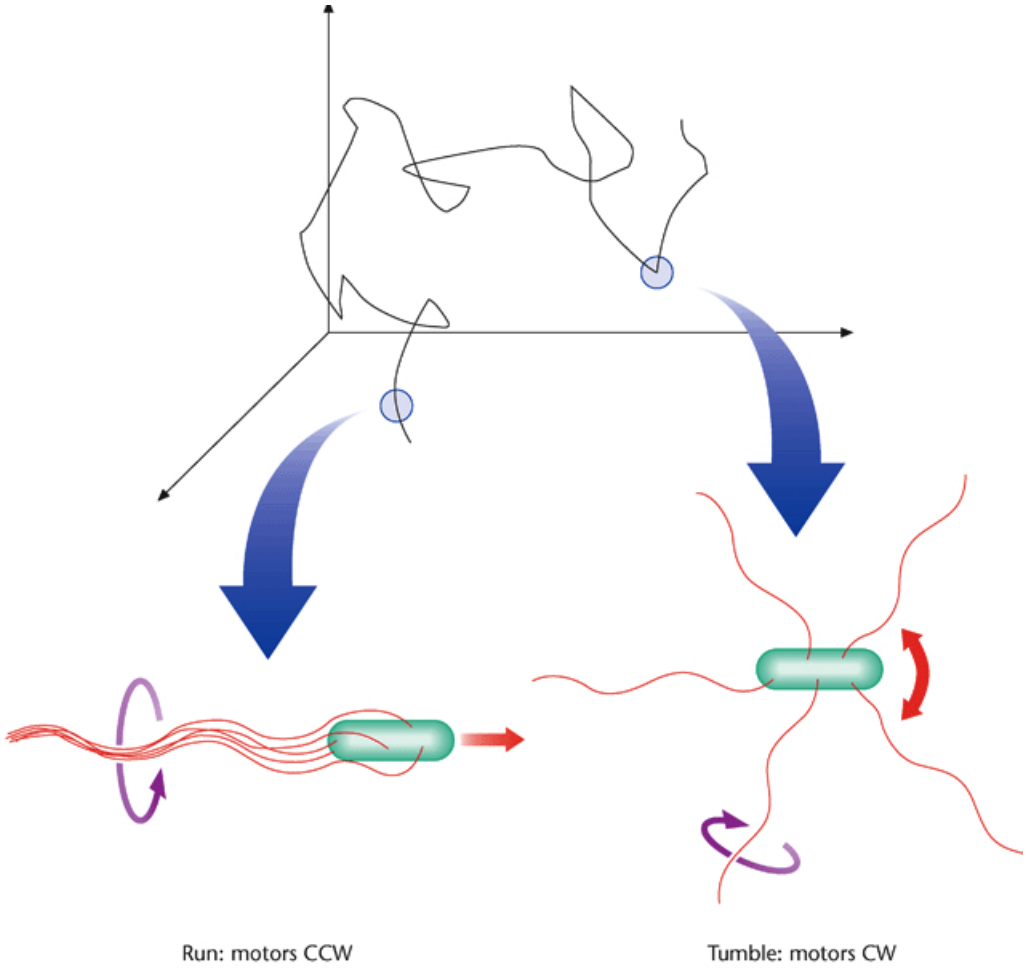


Figure 1.3: The random walk. *E. coli* cells swim by a series of long runs followed by tumbles, where a switch in motor direction causes dispersal of the flagellar bundle with a resulting change in swimming direction. The chemotaxis system alters the bias of run length to tumble frequency. Adapted from [160].

signalling pathway, capable of modulating motor response over a wide range of chemical concentrations. [122] A visual overview of the system can be seen in Figure 1.4. Chemicals are detected by thousands of copies of four different transmembrane chemoreceptors, known as MCPs (methyl-accepting chemotaxis proteins). These proteins form multimeric complexes of "trimers of dimers" in the inner membrane [68], which in turn combine to form large sensor cluster arrays near the cell poles.[175]. Array formation allows any signal to be amplified through allosteric effects, giving cells the ability to respond to small changes in chemical concentration [142].

CheA, a soluble dimeric histidine protein kinase, provides the link between the

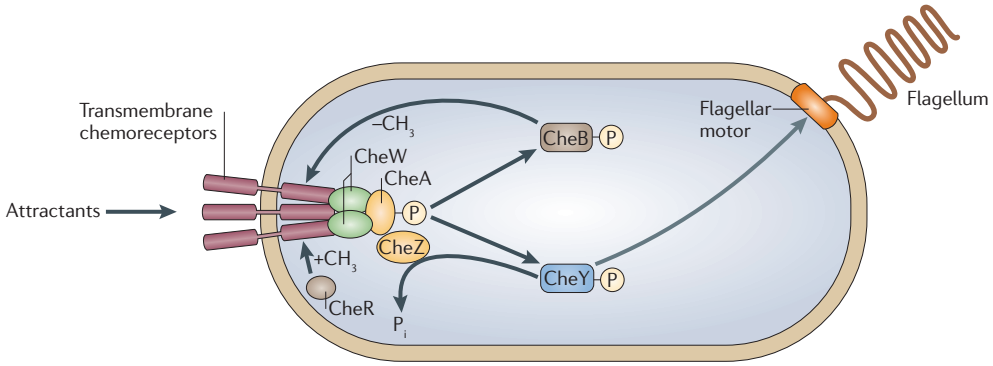


Figure 1.4: The *E. coli* chemotaxis pathway. Attractants bind to transmembrane chemoreceptors, which signal to CheA via in a ligand-dependent fashion. CheA phosphorylates the response regulators CheB and CheY. CheY-P binds to the flagellar motor, where it induces switching. CheB-P is a methylesterase which is involved in adaptation of the chemotaxis pathway. CheR is a constitutively active methyltransferase. CheZ dephosphorylates CheY. Adapted from [123]

MCPs and the rest of the chemotaxis system, and binds to MCPs via a linker protein, CheW. Attractant binding in the periplasmic domain of an MCP causes a conformational change in its transmembrane domain, which is transmitted to CheA through CheW [55]. CheA is capable of autophosphorylation, and in turn phosphorylates the two response regulator proteins, CheY and CheB. MCPs respond to decreased attractant binding by promoting CheA autophosphorylation [22]. Phosphorylated CheY (CheY-P) releases from the sensor cluster and diffuses to the flagellar motor, where it binds to the C-ring and causes motor switching (described in detail in Section 1.4.5). CheB is a methylesterase which is involved in adaptation of the chemotaxis pathway. Additional sensitivity through signal termination is provided by a phosphatase, CheZ. CheY-P naturally autodephosphorylates slowly after around 10 s. CheZ increases this rate by ∼100-fold, decreasing response time for effective motor control [140].

Adaptation acts as a primitive memory for chemotaxis, resetting the signalling state to the chemical concentation experienced in the recent past. This allows the cell to compare the current conditions to those experienced previously [159]. The chemotaxis pathway adapts by reversibly methylating key glutamate residues in the cytoplasmic domains of MCPs. Phosphorylated CheB (CheB-P) removes methyl groups, decreasing MCPs' ability to activate CheA. This is balanced by a constitutively active methyltransferase, CheR, which continually methylates sites on MCPs [39]. As attractants bind to MCPs, their ability to phosphorylate CheA decreases,

in turn reducing the levels of CheY-P and increasing run length. However, the level of CheB-P also falls, increasing MCP methylation. In this way, CheA activity is returned to its former level at the new attractant concentration. CheB phosphorylation therefore acts as a negative feedback loop, enabling effective motor control [1].

1.3 The Bacterial Flagellar Motor

A complex nanomachine in its own right, the bacterial flagellar motor itself is the output device for the chemotaxis pathway. Bacterial flagellar motors are typically made up of around 20 different proteins, with an additional ∼25 more needed for correct expression and assembly. Torque is generated by a transmembrane flux of ions through stator units bound to the motor (discussed in more depth in Sections 1.3.6 and 1.4.2); this torque is transmitted through a basal body complex to a long flagellar filament, which is connected to the motor by a flexible hook. Most known motors are bidirectional; the mechanics of direction switching are discussed in depth in Section 1.4.5

The structure and mechanism of the flagellar motor is very well conserved between the many different bacterial species in which it is found. A schematic of a completed, intact motor can be seen in Figure 1.3. The basal body of the motor can be described as a central rod surrounded by a series of rings, which are usually named for the cellular fractions they co-purify with: [37] the L-, P-, MS- and C- rings correspond to the parts of the basal body which are associated with lipopolysaccharide (outer membrane), peptidoglycan, (inner) membrane and cytoplasm respectively. There is evidence that other cytoplasmic proteins transiently interact with the flagellar motor: a cyclic di-GMP dependent protein, YcgR, binds to the motor and reduces rotation rate [21] [116], and the respiratory protein fumarate reductase binds to the motor and affects switching rate [28].

Although motor structure is highly conserved, different species use motors in different ways. The motor of the monotrichous bacterium, *R. sphaeroides*, is unidirectional [3], with changes in swimming direction effected by a flagellar brake mechanism [120]. Flagella in the Spirochetes are enclosed in the periplasm, and are used to flex and rotate the entire spiral cell [26]. *Aquifex aeolicus*, a hyperthermophile, appears to have a functioning flagellum but no corresponding chemotaxis system [34]. The driving ion for flagellar rotation can be either H^+ (e.g. in *E. coli* or *Streptococcus* [77] [89]), Na^+ (e.g. in *V. alginolyticus* [88]), or, in rare cases, both:

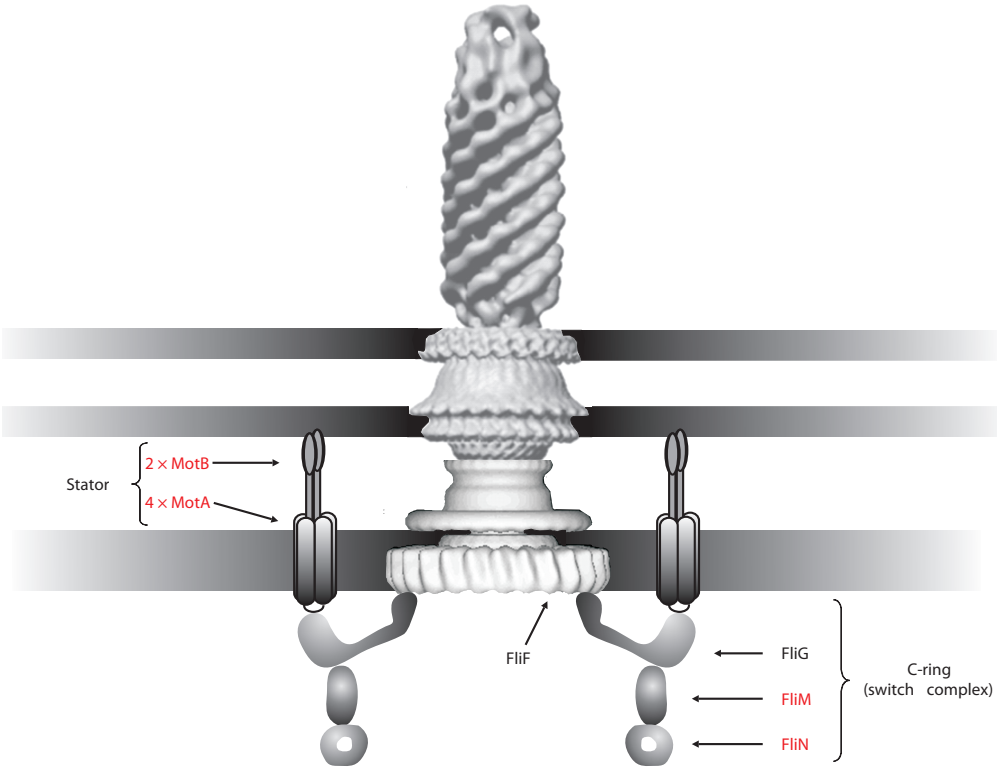


Figure 1.5: A diagram of the structure of the bacterial flagellar motor, showing the positions of the switch complex (FliG, FliM and FliN) and the stators (MotA and MotB) in relation to the basal body and hook. A close-up of the stator/rotor interface can be seen in Figure 1.10.

one striking example is the bacterium *Shewanella oneidensis*, which can use either an H^+ or Na^+ gradient to power a single flagellum located at the cell pole [117].

The intricacy of the flagellar motor is such that proponents of creationism have cited it as an example of "irreducible complexity"; that is, because no part of the motor is useful on its own, it is unlikely to be a product of evolution [10]. However, like several other systems of motility, the bacterial flagellar motor appears to have evolved partly from a secretion system [109], and partly from other pieces of the cellular apparatus. The export apparatus and rotor protein FliM and FliN are homologous to elements of the type III secretion system [110], while the proteins which form the stator complex (MotA and MotB in *E. coli*) are homologous to the ExbBD family of outer membrane receptor energisers [174]. *M. xanthus* A-motility and flagellar rotation appear to share a common method of torque generation; research into the similarities between the two system should provide further insights into the common evolutionary history of cell motility.

This section will discuss the individual components of the flagellar motors in detail, with special attention paid to the motor stators and their role in torque generation. Unless otherwise stated, all component names are from the motor of *E. coli*; homologous proteins in other species may be named differently.

1.3.1 Flagellar Assembly

Although the completed flagellar motor contains ∼20 different proteins, more than 40 genes are involved in flagellar assembly and function. Most of these genes encode proteins that are involved in controlling transcription and/or assembly of the flagellum itself. Strict regulation of flagellar assembly is required to ensure correct copy number of flagellar components and correct motor assembly. The order of gene expression corresponds to the gene products' location in the motor. Flagellar motors are constructed in an "inside out" fashion; that is, the proximal rod and basal body are constructed first, followed by the type III export apparatus and flagella hook. Components like the flagellum and torque-generating stators are synthesised only when motors are ready to be used. Two export pathways are used during flagellar assembly: the integral membrane components are mainly exported using the Sec pathway, while periplasmic and extracellular components are exported using the flagellar export apparatus (for more detail, see Section 1.3.2).

The genes for flagellar assembly in *E. coli* are contained within 15 different operons, arranged in three hierarchical classes [86]. Class 1 contains the master operon for flagellar synthesis, *flhDC*. This master operon is controlled by several environmental factors such as environmental temperature and catabolites. Examples of proteins which activate flagellar synthesis include histone-like protein H-NS [18] and the catabolite activator protein (CAP) [73]. Expression of FlhC and FlhD begins expression of the Class 2 flagellar operons, which encode for the proteins of the hook and basal body. The σ-factor controlling expression of the Class 3 genes, FliA (σ^{28}), is also expressed from a Class 2 operon. Class 3 product expression is delayed until hook completion by FlgM, an anti-σ-factor which inhibits FliA activity. FlgM is encoded on a Class 3 operon, but is expressed at a low level by readthrough from the Class 2 promoter FlgA. Once the hook is completed, FlgM is exported out of the cell, enabling expression of the Class 3 operons. These encode proteins such as FliC, which forms the flagellar filament, the stator proteins MotA and MotB, and several components of the chemotaxis pathway.

1.3.2 Export Apparatus

The flagellar export apparatus is involved in flagellar assembly and translocates those motor components located outside the cytoplasmic membrane. Flagellar components are secreted in a logical order, exactly following the order of assembly [100]. It comprises three cytoplasmic proteins (FliH, FliI and FliJ) and six inner membrane proteins (FlhA, FlhB, FliO, FliP, FliQ and FliR). Together, these form a complex which sits inside the MS and C rings. A diagram of the complex can be seen in Figure 1.3.2.

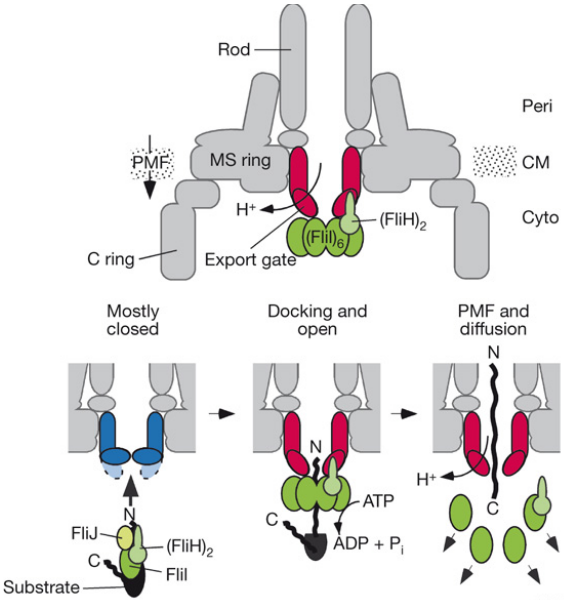


Figure 1.6: The flagellar export apparatus. The FliH-FliI complex and FliJ deliver substrates to the export gate. ATP hydrolysis induces dissocation of FliH, FliI and FliJ from the substrate. A *pmf*-dependent process then induces substrate unfolding and translocation through the export pore. Taken from [102].

The proteins of the export apparatus share a striking homology to those of the type III secretion system of the bacterial injectisome; in some species, their functions overlap, with the flagellar export apparatus also being used to secrete virulence factors [171]. Proteins FliH and FliI, and their homologues in the injectisome, have a strong similarity to parts of the F_1 subunit of ATP synthase [42].

Protein translocation through the flagellar export apparatus is driven by a combination of ATP hydrolysis and the *imf*. A complex of chaperone protein FliJ, regulator protein FliH and the ATPase FliI acts as a pilot, delivering substrates and their chaperones to the narrow pore of the transmembrane export gate. This process is not absolutely required for flagellar assembly, as *fliI-fliH* double mutants are ca-

pable of forming flagella (although the probability of correct formation is very low) [102]. Once proteins pass through the export gate, further translocation appears to be *imf* driven [115].

1.3.3 Flagellar Filament and Hook

A flagellar motor generates torque to power rotation of its attached filament. The flagellar filament acts as a corkscrew; because the filament bundle is asymmetrical, rotation causes a net force which pushes the cell forward [1]. Flagellar filaments can extend up to 10 cell bodies in length, and are typically around 20 nm wide. In *E. coli*, flagellar filaments are homopolymers of FliC (flagellin), with up to 20,000 monomers being incorporated in a single filament.

Flagellar filaments are formed by incorporating FliC monomers at the distal end (i.e. at the flagellar tip). Individual FliC molecules are transported through a channel in the flagellum stretching through the nascent filament through to the export apparatus in the cytoplasm. There is no length-control mechanism in *E. coli*, but a flagellar cap formed by a pentamer of FliD guides individual FliC molecules to the correct binding site and prevents loss to the medium [168].

The filament is arranged in 11 parallel protofilaments, each of which can be in either a left handed (L-type) or right handed (R-type) conformation. When all protofilaments are in the same conformation, the filament takes the form of a straight rod. If one or more protofilaments are in the opposite conformation, the filament is helical in form [66]. To form a flagellar bundle in *E. coli*, all filaments must be left-handed; a switch in motor direction from CW to CCW causes the filaments in that flagellum to change handedness, disrupting the bundle and forcing a cell "tumble" [87].

The flagellar hook is located at the base of the flagellar filament, and is a homopolymer of hook protein FlgE. Unlike the flagellar filament, hook development and hook length are tightly regulated – wild-type hooks in *E. coli* are always 55 nm long [58]. This tight regulation is achieved by proteins FliK and FlhB, which together act as a "tape measure" by measuring nascent hook length and changing FlgE export efficiency accordingly [100]. Flagellar hooks act as a universal joint between the basal body and the filament, and in *E. coli* are much more flexible than the filament itself. The junction between the hook and filament is formed by mediator proteins FlgK and FlgL, which act as an adapter between the two different

[1] The counterintuitive physics of swimming at microbial scales are discussed by E.M Purcell in *Life at Low Reynolds Number [124].*

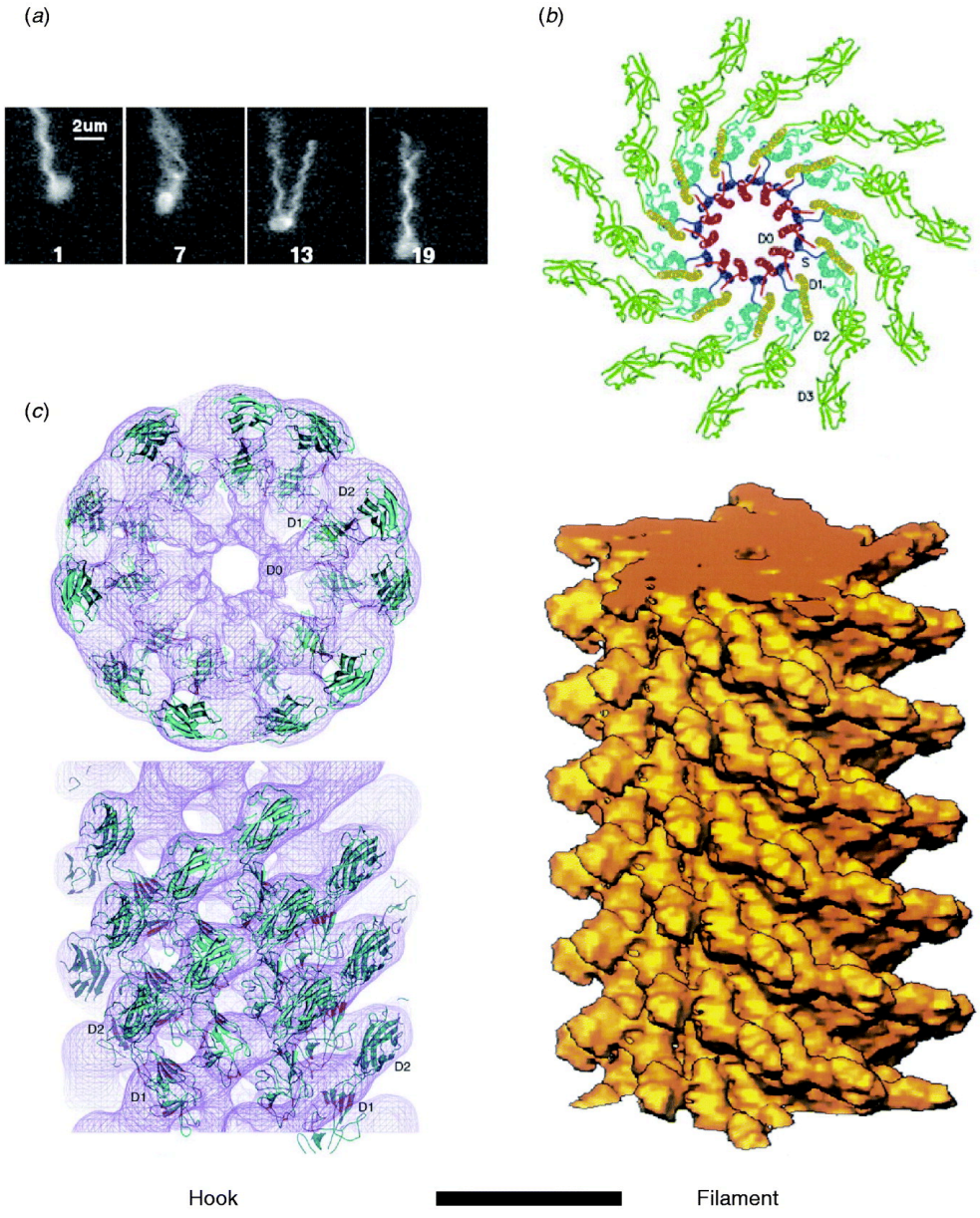


Figure 1.7: The flagellar filament and hook. *(a)* Images of an *E. coli* cell with fluorescently-labelled flagella; the polymorphic transition between "run" and "tumble" can be seen. *(b)* and (c) are structural images of the flagellar hook and filament respectively, revealed by EM and X-ray crystallography. Scale bar is 10 nm. Figure taken from [143]

polymer types [57].

1.3.4 The Basal Body

The basal body of the flagellum comprises a central rod and the L, P, MS and C-rings. Cryo-electron microscopy and tomography have allowed the structure of the basal body to be reconstructed in detail. It acts as a drive shaft to transmit torque from the C-ring, where it is produced, through the cell membranes and wall to the hook and filament. The rod comprises five proteins, FlgB, FlgC, FlgF FlgG and FliE, and rotates with the MS- and C-ring. The L- and P- rings, made of FlgH and FlgI proteins respectively, are anchored in place and act as bushings, enabling motor rotation through the cell wall and outer membrane. Some species which use Na^+ as the driving ion for motor rotation, such as *V. alginolyticus*, contain an extra ring, the T-ring [154]. This ring sits beneath the LP-ring and is made up of two proteins, MotX and MotY, both of which are necessary for stator localisation.

The MS-ring, formed from protein FliF , sits in and above the cell membrane: it connects the C-ring to the rod, and acts as a transmission between the two. Biochemical analysis revealed that the copy number of FliF in the MS-ring is 26 [63], a figure later confirmed by electron microscopy [151].

1.3.5 The Switch Complex

The switch complex sits at the cytoplasmic face of the flagellar motor. It is composed of three cytoplasmic proteins: FliG, FliM and FliN, which together form a large ring (the C-ring) associated with the inner face of the plasma membrane. A schematic of the C-ring and its relation to the rest of the flagellar motor can be seen in Figure 1.8. Mutational, biochemical and structural data have shown that the proteins of the C-ring are involved in the most fundamental processes in motor rotation: the ring as a whole is responsible for motor switching (discussed in Section 1.4), and torque generation depends on interactions between the stator complexes and FliG. The exact stoichiometry and structure of the C-ring remains a topic of debate; there is a mismatch in symmetry between the two components of the ring (FliG and the FliM-FliN complex) which is yet to be adequately explained [80] [114].

FliG

FliG acts as an interface between the stators, the MS-ring, and FliM and FliN. Gene fusions have been made between FliF and FliG, resulting in a single long

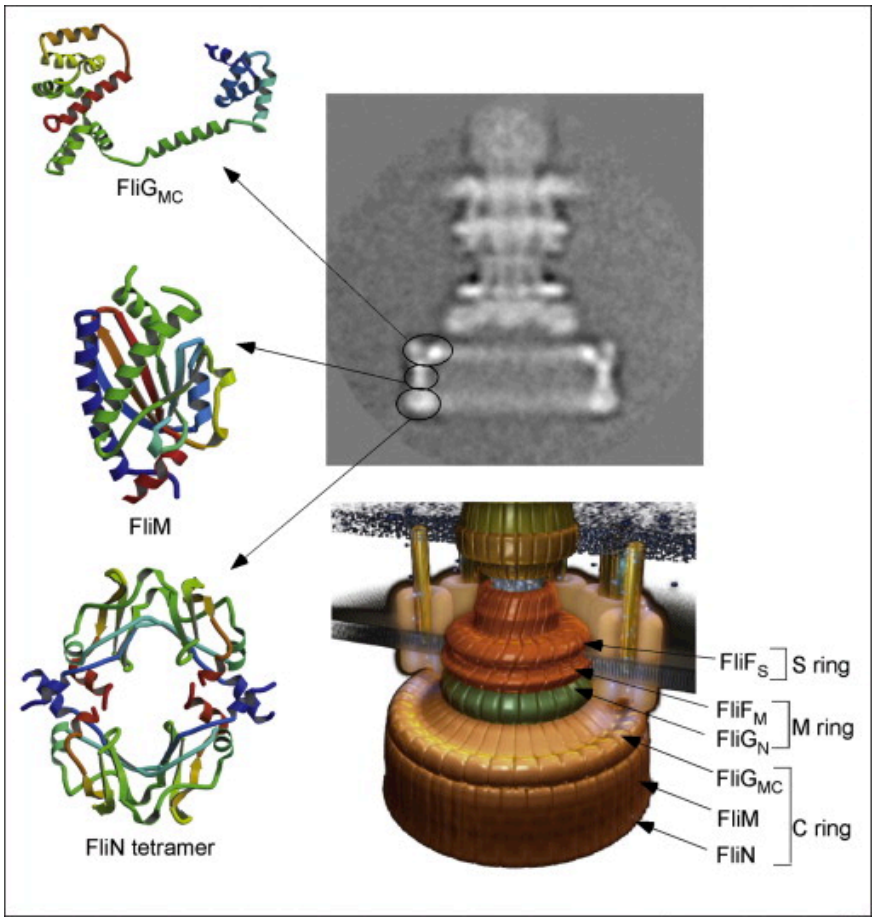


Figure 1.8: The switch complex. *(Left)* The crystal structures of the M- and C- domains of FliG (FliG$_{MC}$), FliM and FliN from *T. maritima*. *(Upper right)* An averaged image of the hook and basal body from cryo-electron microscopy images, showing the positions of the proteins in the C-ring. *(Lower right)* Proposed location of the proteins in relation to the MS-ring. Figure adapted from [101].

polypeptide, FliFG. This fusion, somewhat surprisingly, folds and locates successfully into a functioning flagellar motor [43]. From this, it is thought that the copy number of FliG is 26, with a 1:1 relationship between FliG and FliF in wild-type motors. Initially, the only available FliG structural data was of a fragment missing the N-terminal domain, from *Thermatoga maritima* [23]. The complete structure of the FliG of the hyperthermophile *Aquifex aeolicus* has since been published, which depicted a putative organisation of the FliF-, MotA- and FliM-binding domains. Based on the complete *A. aeolicus* structure, a model C-ring has been proposed which contains 34 FliG monomers [80].

FliM

FliM interacts with FliG, FliN and CheY-P, and forms a ring of around 34 monomers beneath FliG in the switch complex. The crystal structure of the FliM of *T. maritima* has been solved [111], and revealed homology with the CheY-P phosphatases CheC and CheX; FliM, however, does not have any catalytic activity. Binding of CheY-P is thought to cause a conformational change in FilM which can spread to adjacent molecules in the ring, eventually leading to an switch in motor direction.

FliN

The role of the third protein in the switch complex, FliN, is unclear, although it is essential for flagellar assembly and motor switching. The *T. maritima* FliN structure is known, and showed that it forms a natural doughnut-shaped homotetramer [24]. This tetramer associates with a single molecule of FliM to form a stable complex with a stoichiometry of $FliM_1FliN_4$ [113].

1.3.6 Stators

The stator units of the bacterial membrane are stable complexes comprising two integral membrane proteins, MotA and MotB (in sodium-driven motors such as that of *V. alginolyticus*, PomA and PomB). Stators do not have a role in motor assembly, but are vital for torque generation. *motAmotB* deletions are non-motile but not aflagellate, [4] and expression of MotA and MotB from a inducible plasmid results in recovery of motility [19] (discussed in detail in Section 1.5).

MotA is a 4-transmembrane helix protein, with a small cytoplasmic domain between helices 2 and 3. MotB has a single transmembrane helix, with a long linker to a peptidoglycan-binding domain. Each stator is a hexamer of 4 MotA and 2 MotB, which together form two ion channels across the plasma membrane [133]. Although structures of the stator complex are unavailable, extensive cysteine cross-linking studies have provided insights into the internal arrangement of the individual proteins [67]. A schematic of stator organisation can be seen in Figure 1.3.6.

The structure and stoichiometry of the stator complex is well-conserved across many different bacterial species. Depending on species, stator ion channels can conduct either H^+ or Na^+ ions across the membrane. Stators in *Bacillus subtilis* have been shown to be able to use both ion types to power the motor [153]. Furthermore, motor rotation of *V. alginolyticus* in *pomApomB* deletion strains can be restored by induced expression of *E. coli* MotA and MotB [5].

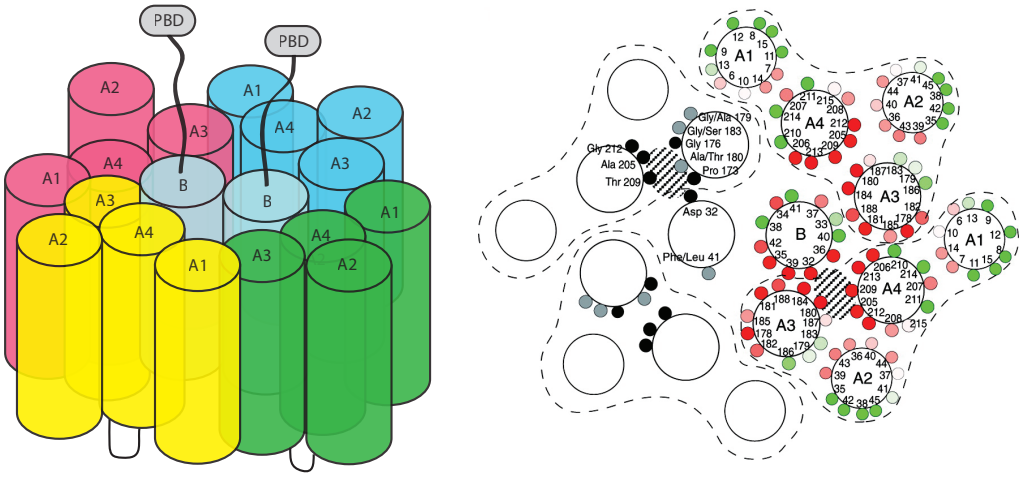


Figure 1.9: A top-down view of an *E. coli* MotAB stator complex. Those residues in red eliminate function if replaced by Trp residues, with shading representing degree of dominance compared to wild type. Residues in green do not eliminate function when replaced, with shading representing relative function. Shaded residues on the left are conserved between many species. Adapted from [67].

Ion-selectivity in stators is mediated by the transmembrane domain of MotB. The bifunctional stator of some *B. subtilis* strains can be converted to act as an exclusively H^+- or Na^+-conducting channel by mutating residues on the outside of the transmembrane helix [153]. This principle has been extended by the design and construction of "chimeric" stators, which combine the C-terminal domain of *E. coli* MotB with the N-terminal domain of *V. alginolyticus* PomB, forming a new protein PotB. Expression of PotB in a *motB* deletion strain converts the *E. coli* motor to one driven by Na^+ ions [5].

Not all stator complexes present in a cell are attached to flagellar motors. At any given time, a "pool" of inactive stators is present in the plasma membrane [79]. Overexpression of stator proteins does not result in lowered growth rate, which suggests that unattached stators do not act as ion channels. [148]. A region of MotB, either the peptidoglycan-binding domain or a section of the linker, is thought to detach from the cell wall in inactive stators, moving down to act as a "plug" which inactivates the ion channel [59] [72]. The mechanism for such a conformation change is unknown, but perhaps involves the loss of interactions between MotA, FliF and FliG [72].

1.4 Torque Generation and Switching in the Flagellar Motor

The mechanisms of torque generation in the flagellar motor have been relatively well-studied compared to other molecular rotary motors such as the F_OF_1 ATP synthase or the archaeal flagellar motor. Motor switching (and the closely related mechanism of motor stopping in unidirectional motors) has also been studied in detail.

1.4.1 The Rotor/Stator Interface

A cluster of charged residues on MotA and FliG form the interface between the rotor and the stator. The details of these interactions differ slightly between species [166]; a schematic of those of *E. coli*, along with other residues important for torque generation, is shown in Figure 1.10. Cross-linking and site-directed mutagenesis studies have shown that the effect of these interactions are together necessary for torque generation, but no single residue is essential – individual mutations result in partial loss of motor function [176]. The charges at the interface between the two proteins can be reversed without significant loss of function [84].

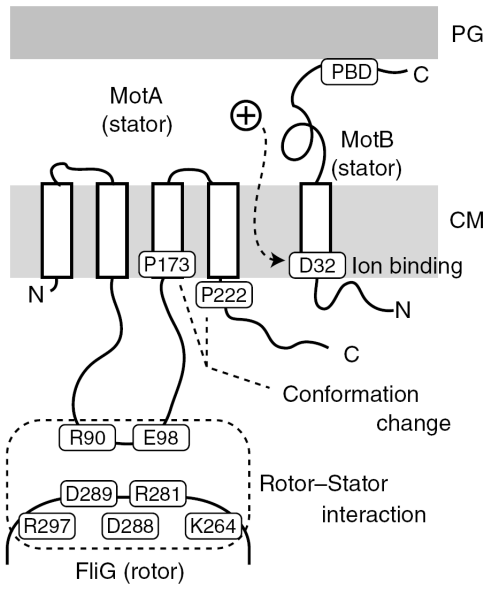


Figure 1.10: A diagram of functionally important residues for torque generation in *E. coli*. Mutation analysis shows that the electrostatic interaction between FliG and MotA is vital for torque generation. The conserved Asp32 residue of MotB appears to play a direct role in proton transfer. Adapted from [143]

Changes in these interactions are driven by association and dissociation of the

H^+ or Na^+ driving ion at a single conserved Asp residue in MotB. Mutation of this Asp residue results in almost total loss of motor activity, with only the Asp/Glu mutation retaining slight functionality [177]. Transit of an ion through the stator via this Asp residue is thought cause a conformational change in MotA, which is then transmitted to FliG; the details of this process are still unknown.

1.4.2 Motor Rotation

Given that motor rotation is driven by transit of individual ions through the stator units, it is assumed that rotation occurs in discrete increments; that is, that the flagellar motor is a stepping motor. Observation of steps in rotation is difficult for several reasons: motor speed can be very high (the *V. alginolyticus* motor can rotate at speeds up to 1700 Hz), many torque-generating units are present under physiological conditions, rotation is observed via an elastic linkage (the flagellar hook), and step size is predicted to be small (from the 26-fold symmetry of the rotor) [165].

Steps in rotation were observed for the first time by attachment of small beads to the flagellar hooks of chimeric *E. coli* Na^+-driven motors [145]. Stators were expressed at low level from an inducible plasmid, and motor speed was controlled by lowering *smf* through the reduction of sodium concentration in the external buffer. By lowering motor speed to ∼10 Hz, 26 steps could be observed, a figure consistent with the putative periodicity of the rotor.

1.4.3 The Torque/Speed Curve of the Flagellar Motor

Torque production in the motor is dependent on several factors, such as motor load, viscocity of the medium and the isotope of the driving ion. The load on the motor varies depending on the method used to measure motor rotation – the most common method used is to attach beads of varying sizes to flagellar filaments. An important test for theoretical models of the mechanical cycle of the motor is to replicate the relationship between motor torque and rotation speed under different operating conditions. Much work has therefore gone into accurately measuring the torque-speed curve of the flagellar motor in different species [13][17][144][60]. A graph summarising the main results of torque-speed studies in *E. coli*, *V. alginolyticus* *Caulobacter crescentus* and *Streptococcus* can be seen in Figure 1.11.

Most measurements of the torque-speed curve display a characteristic pattern. Torque remains almost constant (the "plateau") up to a "knee" speed (∼160 Hz in

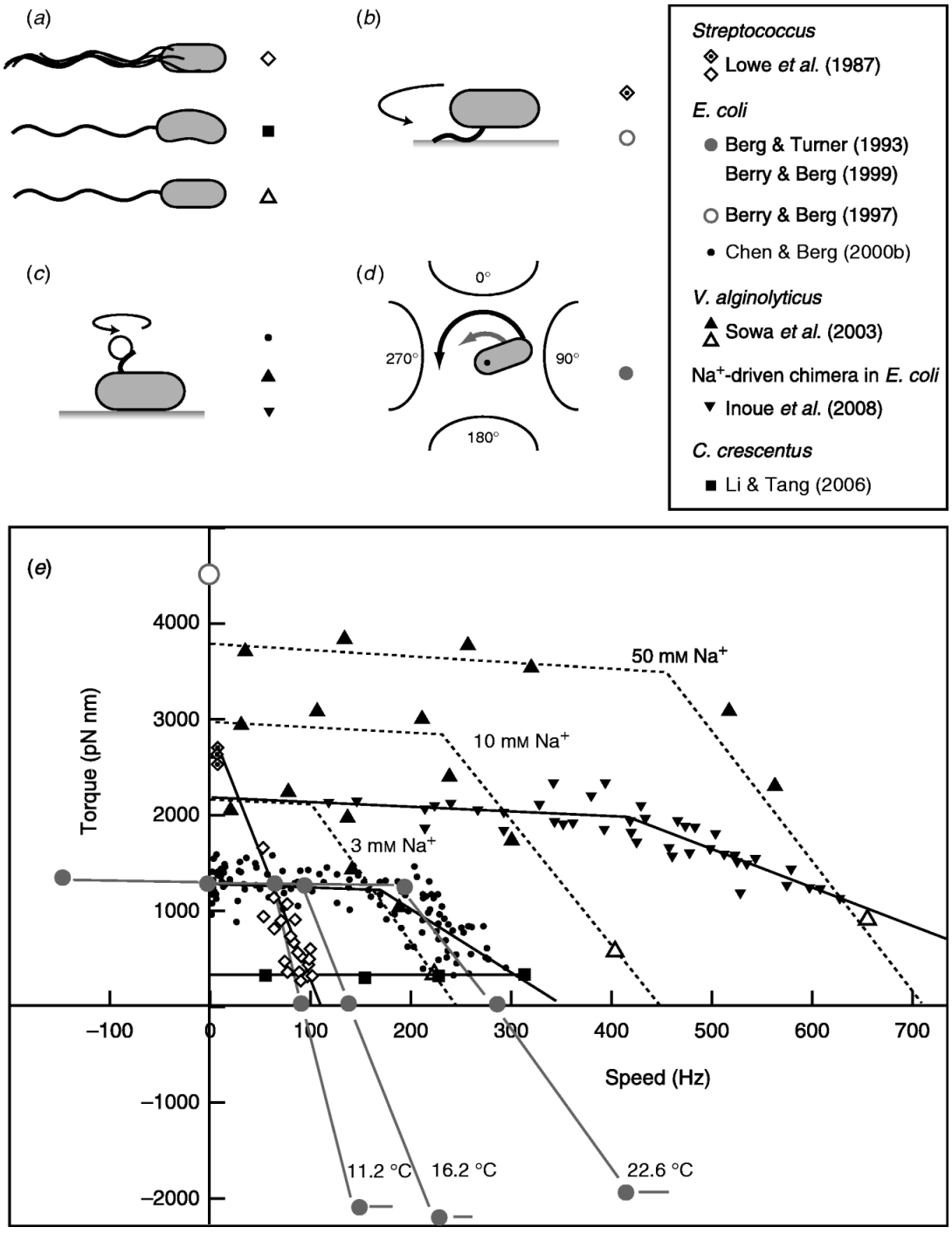


Figure 1.11: Motor torque *vs.* speed. Different techniques have been used to measure the torque-speed relationship: *(a)* Microscopy of swimming cells; *(b)* Tethered cells; *(c)* Bead assay; *(d)* Electrorotation of tethered cells. *(e)* shows torque-speed curves measured using various methods in various species. All measurements were taken at room temperature unless indicated otherwise. Taken from [143].

the *E. coli* motor), then falls linearly to the zero-torque speed. This pattern holds for cells at "negative" speeds, where CCW-biased motors are forced to run backwards, translocating ions from the cytoplasm to the periplasm [17]. In the plateau region, the speed is thought to be limited by mechanical load on the motor. At speeds faster than the "knee", the rate-limiting step appears to be conformational change in the motor [143].

Surprisingly, the relationship between torque and speed has been shown to be different for CW rotation in bidirectional motors. Measurements of CW-biased motors in CheY-overexpressing *E. coli* cells found a torque-speed curve which is linear, without a "knee" transition speed [173]. The reason for this difference is unknown; one hypothesis is that there is an asymmetry in interaction potentials between the stator and rotor for CW- and CCW- biased motors [94].

1.4.4 Theoretical Models for Motor Rotation

Several different models have been put forward to explain motor rotation in terms of detailed electrostatic interactions between the stator and the rotor [78] [96] [15] [162] [134]. Newer models attempt to describe motor properties, such as stepping in rotation and the torque-speed curve's "knee" more generally, leaving the exact mechanism as an open question. The most current model assumes that the two force-generating components of a stator (corresponding to the two ion channels) sequentially change conformation, moving the rotor in a series of power strokes [95][94]. This model reproduces several important motor characteristics, such as the shape of the torque-speed curve during CW and CCW rotation, and the results of resurrection experiments at varying loads.

1.4.5 Motor Switching

The mechanism for motor switching is not yet fully understood. The motor has been shown to be ultrasensitive to CheY-P concentration, with a Hill coefficient of $\sim$10 [27]. Motor switching is very quick – *S. typhimurium* was observed to switch from 100 Hz in one direction to 100 Hz in the other in less than 1 ms [75]. Switching is thought to depend on an induced conformational change in FliM after binding of CheY-P. With 34 FliM subunits in the motor, any conformational change in a single FliM has to be somehow transmitted throughout the ring. Any model for motor switching must therefore account for cooperativity between FliM subunits during conformational change.

The "conformational spread" model is the most commonly accepted as a mechanism for motor switching [41]. In this model, a single CheY-FliM binding event forces a change in conformation in one part of the ring. This "nucleus" for conformational change biases its neighbouring FliM molecules to switch; the new conformation either spreads through entire ring, or collapses, restoring the initial ring state. Evidence for this model is provided by the observation of "incomplete" switching events in wild-type *E. coli* motors [7].

1.5 Motor Dynamics

1.5.1 Motor Resurrection

A full complement of stator units around the motor is not necessary for motor function. The first "resurrection" study, where rotation in stopped motors was restored by induced expression of stators [19] revealed that one torque-generating unit was sufficient to drive motor rotation. Discrete increments in speed were observed as stator units entered the motor. In tethered cells, a maximum of eight speed increments were observed, leading to the hypothesis that eight stators could fit around the motor basal body.

Further analysis [125], measuring resurrection of motors with beads attached to flagellar filaments, indicated that the maximum number of stators around the basal body was at least 11 (see Figure 1.12). Measurement of individual stator contribution to motor speed during resurrection showed that speed increments decreased with stator number. This may represent interference between individual stators in the motor at high stator number. During extended observations of resurrected cells, transient speed drops were observed, probably corresponding to the loss of the contribution of the single stator. This finding was the first evidence that stator binding may be reversible, and that stators may not necessarily bepermanently bound to functioning motors.

Flagellar motors also display resurrection behaviour upon disruption and restoration of *imf*. Initial studies used lysed filamentous cells inside a micropipette. By applying a command voltage across the membrane, motor function in the lysed cell could be restored [48]. After application of the external voltage, speed increased discretely – this was ascribed to sequential activation of bound stators. Similar behaviour was observed in intact *E. coli* cells expressing chimeric stators; by lowering the external Na^+ concentration, motors were made to stop. Restoration of Na^+

resulted in stepwise increase in motor speed [145].

Resurrection behaviour differs with the load on the motor. As load decreases, the effect of multiple stators reduces; at very low loads, one stator is capable of rotating the motor as rapidly as many [172] (see Section C of Figure 1.12). This finding showed that the stators have a high duty ratio; that is, stators remain linked to the motor for most of their mechanical cycle [129].

1.5.2 Turnover of Motor Components

The naïve view that completed flagellar motors were fixed and unchanging complexes was challenged by the discovery of stator turnover in *E. coli* cells [79]. Creation of a functional GFP-MotB fusion allowed stator dynamics to be observed *in vivo*. By monitoring fluorescence recovery after photobleaching (FRAP) and fluorescence loss in photobleaching fluorescence loss in photobleaching using total internal reflection (TIRF) microscopy (described in Section 1.8), MotB turnover between the motor and a membrane pool of ∼200 diffusing MotB molecules could be seen. The average lifetime of a stator in the motor was estimated at 30 seconds.

The same method was later used to investigate the dynamic behaviour of the rotor switch protein, FliM. Fluorescence loss in photobleaching (FLIP) and FRAP studies indicated the presence of two distinct populations of FliM in functioning motors: one which remained permanently associated with the motor, and one which underwent stochastic turnover [36]. Turnover of this dynamic population was shown to be dependent on the presence of CheY. "Incomplete" FliM complexes were also observed in the cell cytoplasm with a stoichiometry of ∼18 FliM molecules; the function of these is unknown. Turnover of overexpressed GFP-tagged FliM and FliN has also been observed in *E. coli* [46]; in the same study, no turnover of FliG was observed.

1.5.3 The Relationship between Motors and the *imf*

The relationship between motor speed, motor dynamics and the *imf* is complex and not yet fully understood. At high load, motor speed is directly proportional to the strength of the *imf* [48] [49]. The *imf* across a cell membrane has two components: a chemiosmotic gradient, and an electrostatic voltage (discussed in detail in Section 1.6.1); at high load, the contribution of these is equivalent [90]. At low load, however, the relationship is not identical, and speed is dependent on ion concentration [85].

Ion-flux experiments with the *Streptococcus* motor allowed an estimate of the

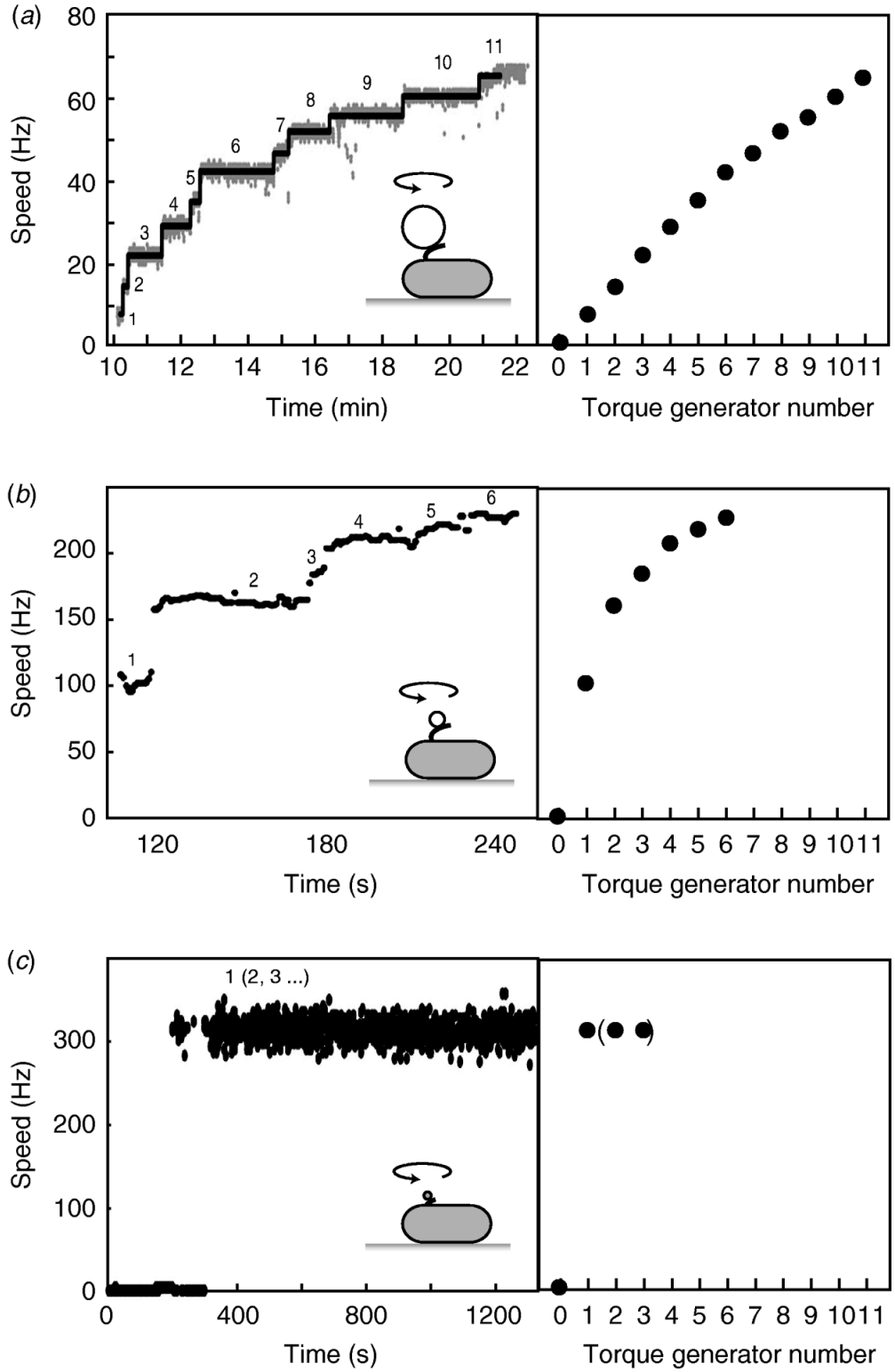


Figure 1.12: Resurrection experiments in *E. coli*, showing the discrete nature of the torque-generating unit and the effects of load. *(Left)* Speed/time traces following induced expression of stators in *motAmotB* deletion strains. *(Right)* Speed *vs* stator number. *(a)* Motors at high load (1 μm bead) show up to 11 speed increments. *(b)* At lower load, fewer speed increments are observed. *(c)* At very low load (60 nm bead) one stator is sufficient to drive the motor at full speed. Taken from [143].

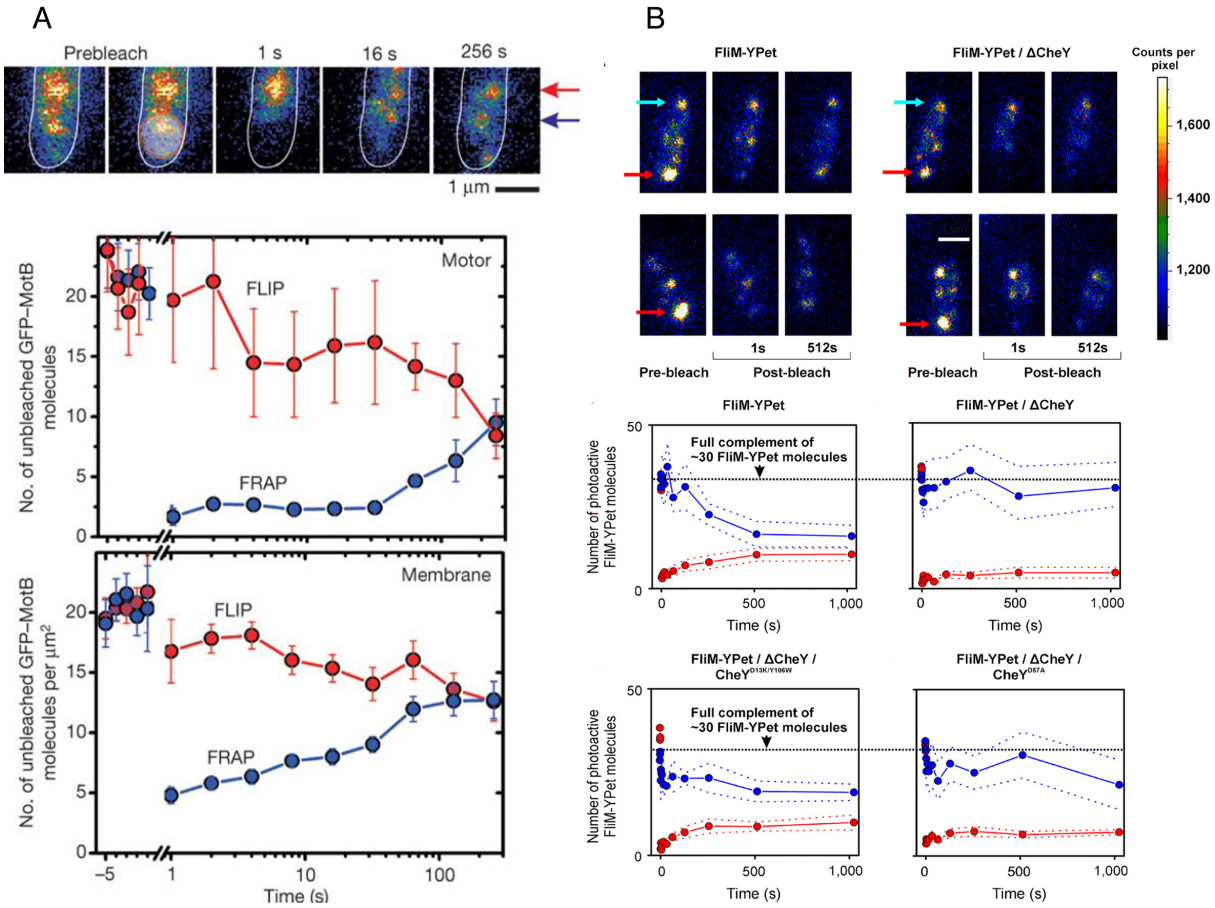


Figure 1.13: Turnover of components in functioning *E. coli* flagellar motors. *(A) (Top)* Successive TIRF microscopy images of a GFP-MotB cell before and after photobleaching. Arrows show position of motors showing FRAP (blue) and FLIP (red). *(Bottom)* Mean numbers of unbleached GFP-MotB molecules in the motor and membrane over time. Convergence of FRAP and FLIP lines indicate complete turnover of stators between motor and membrane. *(B) (Top)* Successive TIRF images of YPet-FliM in w.t. (left) and $\Delta cheY$ strains (right). *(Bottom)* Mean numbers of unbleached YPet-FliM molecules in the motor and in the cell background over time. Partial turnover is seen in w.t cells, and there is no turnover in the $\Delta cheY$ strain. Adapted from [79] and [36]

.

number of ions through the flagellar motor to be made. Estimated flux was around 1200 ions per motor revolution, for flagellar speeds of 20-60 Hz [97]. The thermodynamic efficiency of the motor at high load is close to 100 % [165]. Lower loads appear to reduce the efficiency, so that the number of ions transiting across the membrane is greater than that needed to drive the motor [85].

There is evidence that integrity of the motor is partially dependent on the *imf*. Fluorescently-tagged non-functional PomA molecules are reliant on an external sodium concentration for localisation to the pole of *V. alginolyticus* cells [47]. The monoflagellate bacterium *S. oneidensis* expresses two sets of stators, PomAB and MotAB, which translocate Na^+ and H^+ ions respectively. Localisation of PomAB to the motor was found to be dependent on the external sodium concentration, and was capable of displacing bound MotAB stators after induced expression in a *pomAB* deletion strain [117].

1.6 *E. coli* BIOENERGETICS

The field of bioenergetics first arose to answer the question of how the free energy obtained from metabolic reactions was made available to "uphill" reactions, such as ATP synthesis, or ion transport [107]. This question was answered by the development of the chemiosmotic theory, which posits that energy from metabolism is stored in a proton gradient across the plasma membrane of cells or organelles. The energy stored by this gradient is known as the proton motive force, or *pmf*, and is used to drive many vital processes other than motor rotation. The F_OF_1 ATP synthase uses the *pmf* to drive production of ATP from ADP and Pi [104], and transport of ions across the membrane is largely *pmf* driven [163]. This section will provide a brief theoretical description of the *pmf*, and detail how it is produced in *E. coli*.

1.6.1 THE PROTON MOTIVE FORCE

The *pmf* is essentially an ion gradient across an impermeable barrier (the plasma membrane). The gradient has two components: a concentration gradient, which for protons can be described as a pH difference (ΔpH) across the membrane, and an electrostatic potential difference, resulting from the charge distribution in the aqueous phases either side of the membrane (the membrane potential, $\Delta\psi$).

The Gibbs free energy change for the transfer of 1 mol of protons across a membrane with concentration difference ΔpH, in the absence of any membrane potential,

can be described thus:

$$\Delta G \text{ (kJ mol}^{-1}) = 2.3RT \ \Delta\text{pH}$$

where R = the ideal gas constant ($\sim$8.31 J K^{-1} mol^{-1}) and T = the absolute temperature.

The contribution of the membrane potential can also be calculated. For 1 mol of protons, the Gibbs free energy change from being transported down an electrical potential of $\Delta\psi$ mV can be described thus:

$$\Delta G \text{ (kJ mol}^{-1}) = -F\Delta\psi$$

where F = the Faraday constant ($\sim 98,465$ C mol^{-1}).

In most physiological situations, the *pmf* comprises both a chemical and electrostatic gradient. For the *pmf*, the Gibbs free energy change is often expressed as an ion electrochemical gradient, $\Delta\tilde{\mu}_{\text{H}^+}$, and can be calculated by adding the two components together:

$$\Delta\tilde{\mu}_{\text{H}^+} = F\Delta\psi + 2.3RT \ \Delta\text{pH}$$

The *pmf* is usually given as a voltage figure which can be easily calculated from the ion electrochemical gradient:

$$\Delta P \text{ (mV)} = -\frac{\Delta\tilde{\mu}_{\text{H}^+}}{F}$$

Using ΔP and substituting the variable T with the room temperature, 25 °C (298 K), gives a final useful equation:

$$\Delta P \text{ (mV)} = \Delta\psi - 59 \ \Delta\text{pH}$$

This equation shows the relationship between the two components of the *pmf*. Typically, a mid-log phase aerobically-grown *E. coli* cell maintains a *pmf* of around -150 mV. Processes which make use of the *pmf* can be likened to electric circuits, with sources of *pmf* as batteries and *pmf* sinks as resistors. Like electric circuits, the physiological *pmf* can be "short-circuited". This is done by inoculating cells with an protonophore such as CCCP, which makes the plasma membrane permeable to protons. Individual components of the *pmf* can also be collapsed, so that only the pH gradient or membrane potential remains. Valinomycin is a natural antibiotic which collapses membrane potential by transporting K^+ or NH_4^+ ions across membrane,

so that ΔpH is the only component of *pmf*. Nigericin, another antibiotic, has the opposite effect: it is a K^+-H^+ antiporter which equalises total cation concentrations across a membrane, abolishing the chemical gradient. By using these molecules and others, the effects of individual components of the *pmf* on motor behaviour can be studied.

1.6.2 METHODS OF *pmf* PRODUCTION IN *E. coli*

Since *E. coli* has no native photosynthetic apparatus, the main source of *pmf* is the respiratory apparatus. *E. coli* is a facultative aerobic bacterium which can utilise many different substrates. The respiratory chains of *E. coli* comprise 15 primary dehydrogenases and ten terminal reductases, mediated by three different quinones [137]; however, due to energetic constraints, not all of these can be coupled with each other [158].

When grown aerobically, *E. coli* uses cytochrome bo_3 (cyt bo_3) as its terminal oxidase, which accepts electrons from ubiquinol. A second oxidase, cyt *bd*, is expressed under low-oxygen conditions. The electron transfer chain can be seen in 1.14. Cytochrome bo_3 is a haem-copper oxidase, and functions as a proton pump, directly transporting two protons across the membrane upon ubiquinol oxidation. Cyt bo_3, as a haem-copper oxidase, is inhibited by sodium azide; inoculating aerobically-grown cells in a NaN_3 solution effectively disrupts native p.m.f. generation [81].

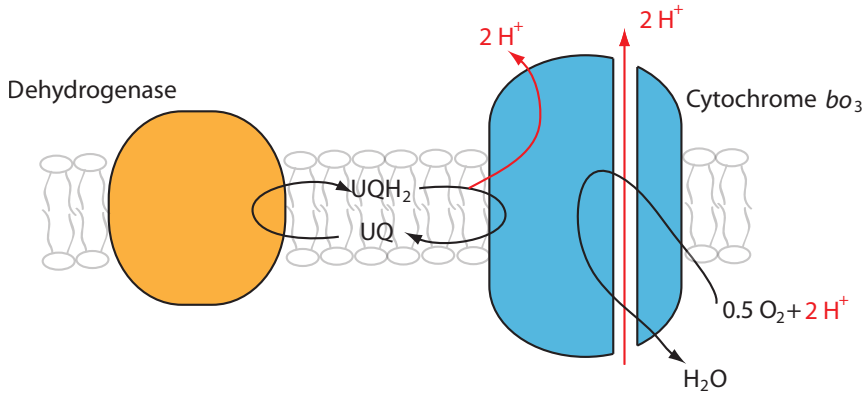


Figure 1.14: The *E. coli* aerobic electron transport chain, showing proton pumping and terminal reduction of molecular oxygen.

1.7 Proteorhodopsin

Many different organisms can make use of light energy to power cellular processes. The principal method found in nature, and for a long time the only method known to science, was chlorophyll-mediated photosynthesis. There are several other important mechanisms, however; the most widespread of these are the opsins. The opsins are a family comprising mainly light-driven proton pumps, and are found in many different species in all three domains. All opsins share a similar structure, being formed from seven transmembrane helices. The first example of a microbial opsin to be found, and the best studied, is bacteriorhodopsin (bR), found in halophilic *Archaea*. Several other related proteins with similar mechanisms of action have since been discovered; perhaps the most widely distributed is proteorhodopsin (pR), the native opsin of bacteria.

1.7.1 Discovery and Diversity

Proteorhodopsin was first discovered using the nascent technique of community metagenomics, where DNA from a large microbial community is purified and sequenced without first culturing the organisms present. The first pR gene found was extracted from the genome of marine bacterium clade SAR86. Sequence analysis revealed it to be homologous to other opsins, and when expressed in *E. coli*, was found to fold correctly and insert into the cell membrane [11].

Since the discovery of the first pR, many other variants have been found. Proteorhodopsin has been found in a diverse range of bacterial species, including the extremely abundant SAR11 clade [52], and in many different marine habitats [130]. Through lateral gene transfer, pR has spread to marine archaeal species [45]; and has even been found in eukaryotic dinoflagellates [141]. pR appears to give a marked selective advantage in the resource-scarce oceanic ecosystem; for example, marine *Vibrio* species are more resistant to starvation when pR is expressed [53].

The diversity of species utilising pR is testament to its versatility. Different "spectrally-tuned" variants have evolved which absorb different frequencies of light. Those species expressing blue-absorbing pR are typically found in deeper ocean, while green-absorbing variants are found in surface-dwelling species. This adaptation matches well with the solar spectrum at these depths. The green-absorbing pR has an absorption maximum of 540 nm, similar to the solar maximum [11], while blue light penetrates furthest to the ocean depths. Other species appear to have adapted pR further to act as a light-sensor, rather than a proton-pump [147]

– these variants do not have a proton-translocation mechanism and are generally cotranscribed with their transducer.

1.7.2 Mechanism of Proton Pumping

Despite their differing spectral properties, all proton-pumping pRs isolated share the same proton-translocation mechanism. Studies of the pR photocycle have focused on two variants, green-pumping pR (GPR) and blue-pumping pR (BPR), named for their absorption maxima. Site-directed mutagenesis studies and spectroscopic analysis have shown show that the proton-pumping mechanism of both GPR and BPR are similar to that of bR, the prototypical light-driven proton pump. This section will concentrate on the mechanics of GPR: as the first variant isolated, it is the best studied.

Similarly to bR, the seven transmembrane helices of pR surround a bound retinal cofactor. A map of pR secondary structure can be seen in Figure 1.15. This retinal is attached to the polypeptide by formation of a protonated Schiff base with a key lysine residue. A proton translocation channel extends through the centre of the protein, forming a complete route from cytoplasm to periplasm. This channel is lined by "carrier" amino acid residues and water molecules which together form a path across the membrane [69]. Light-induced structural changes in pR cause these carriers to pass a proton from one functional group to another in a manner well-defined by the pKa of each key residue [38]. No crystal structure of pR has yet been found; however, atomic-force microscope (AFM) unfolding analysis of pR reveals a similar folding pattern to bR [70], and the pR sequence can be mapped onto the bR crystal structure [2].

The GPR reaction cycle begins when pR absorbs light energy through photoisomeration of the retinal co-factor. This event causes transfer of a proton from the Schiff base to a key aspartate residue (Asp97). Unlike bR, deprotonation of the Schiff base in pR does not cause immediate proton release to the periplasm, as pR lacks the required proton release group (Glu194 and Glu204 in bR) [44]. Instead, the Schiff base is quickly reprotonated by a glutamate residue, Glu108. Proton release is mediated by a histidine residue (His75), which interacts with Asp97 and is deprotonated in response to protonation of Asp97 [14].

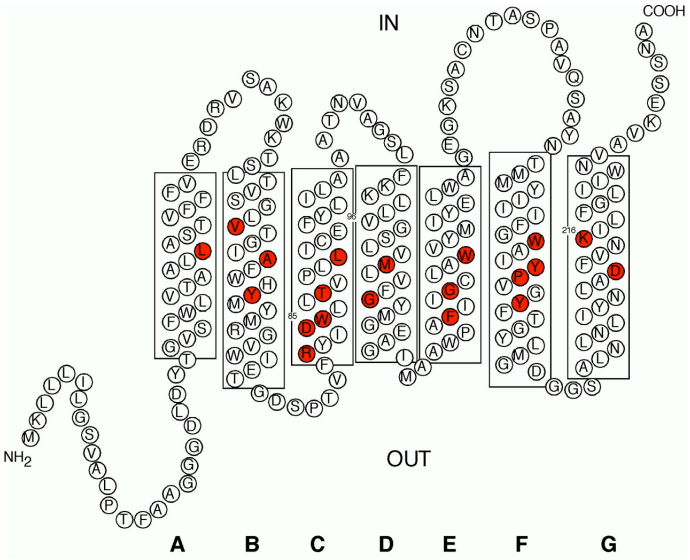


Figure 1.15: The secondary structure of GPR, showing the amino acids forming the seven α-helices. Residues in red are thought to be essential for retinal binding. Taken from [52].

1.7.3 UTILITIES

pR can be used as a robust and simple photosystem in *E. coli*. A complete pR-based photosystem is encoded by only six genes – pR, and five retinal biosynthesis genes. Fosmid incorporation of these genes into wild-type *E. coli* produced cells capable of photophosphorylation of ATP [91]. By supplementing growth medium with retinal, expression of the pR polypeptide alone has been shown to be sufficient for light-driven proton pumping in *E. coli* [161]. The pR-generated *pmf* in the latter experiment was shown to be capable of powering rotation of flagella in tethered cells, providing a striking demonstration of pR's capabilities.

GPR has been modified to act as a voltage sensor in bacterial membranes. By mutating Asp97 to arginine, proton pumping is abolished. The protonation state of the Schiff base is then dependent on membrane voltage, and can be measured using fluorescence microscopy. In this way, electrical "spiking" corresponding to rapid depolarisation of the *E. coli* cell membrane was observed for the first time [74].

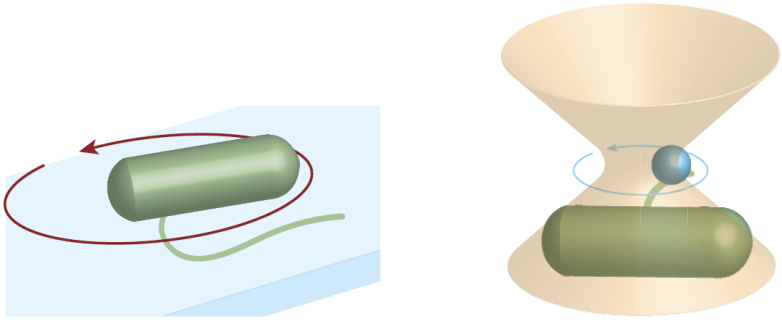
1.8 Experimental Techniques

1.8.1 Measuring Motor Rotation

Although the speed of the flagellar filament can be measured directly [127], most studies into motor rotation measure the rotation of either an attached marker (bead assays) or the cell body itself (tethered cell assays). For diagrams of each method, see Figure 1.16. Tethered cells and beads can be accurately measured, allowing easier measurement of motor speed or rotary angle.

Tethered Cell Assays

In a tethered cell assay, whole cells are attached to a glass coverslip by their flagella using either anti-filament antibodies or mutant "sticky" flagellin, which are hydrophobic and have an affinity for glass [76]. Since the flagellar filament is fixed in place, motor torque causes the entire cell to rotate around the point of tethering. Rotation of the entire cell places a much higher load on the motor than rotation of the filament alone – this results in observed speeds much slower than in swimming cells.



(a) A "tethered cell" (b) Bead on a filament stub

Figure 1.16: Two different methods of measuring motor output. *(a)* A cell tethered by its flagellum to a glass coverslip. The cell body rotates around the point of tethering. *(b)* A polystyrene bead bound to a mutant "sticky" flagellar filament. Load on the motor can be varied by changing bead size.

Bead Assays

Greater angle and speed resolution, and variance in load, is possible by measuring the rotation of beads attached to truncated flagellar stubs. Either "sticky" flagellin or anti-filament antibodies can be used to ensure adhesion. The viscous drag of a

300 nm polystyrene bead is approximately equivalent to that of a flagellar filament; load can be increased or decreased by varying the size of the bead, allowing accurate torque/speed curves to be measured. Bead position over time is typically measured either with a high-speed camera or by back-focal-plane (BFP) interferometry.

BFP Interferometry

BFP interferometry is a method used to accurately measure the behaviour of a rapidly rotating object using a light microscope. A light source (typically a low-power laser) is focused on the object being observed. A photodiode in the back-focal-plane of the microscope's imaging path outputs a current in response to detected photons. The photodiode is split into four quadrants, which together make a circle. Output currents from the four quadrants are converted to four voltage figures which are proportional to the intensity of the light detected. The amplified voltage signals, V_a, V_b, V_c and V_d are processed into an object x, y position, P_x and P_y, using the following formulae:

$$P_x = \frac{(V_b + V_d) - (V_a + V_c)}{V_a + V_b + V_c + V_d}$$

$$P_y = \frac{(V_a + V_b) - (V_c + V_d)}{V_a + V_b + V_c + V_d}$$

BFP interferometry has been used to measure the rotation of whole cells of *R. sphaeroides* [16], but has proven most useful for measuring the rotation of small beads bound to flagellar filaments [129].

There are two methods of obtaining object speed from the x, y data collected by BFP interferometry. A power spectrum of the combined data set can be taken to form a complex signal (for details, see Section 1.3.4 of [126]), or, for objects with clean and consistent trajectories, bead position can be mapped to a $d\theta/dt$ trace directly.

1.8.2 Fluorescence Microscopy

Fluorescence is a property of some molecules whereby they are capable of absorbing light of one wavelength and emitting light of another. Photons of light are absorbed by electrons in the molecule, raising them to an excited state. The energy possessed by an individual photon is given by the formula:

$$E = h(\frac{c}{\lambda})$$

where E = photon energy, h = Planck's constant ($\sim 6.63 \times 10^{-34}$ J s), c = the speed of light in vacuum ($\sim 3 \times 10^8$ m s^{-1}) and λ = light wavelength.

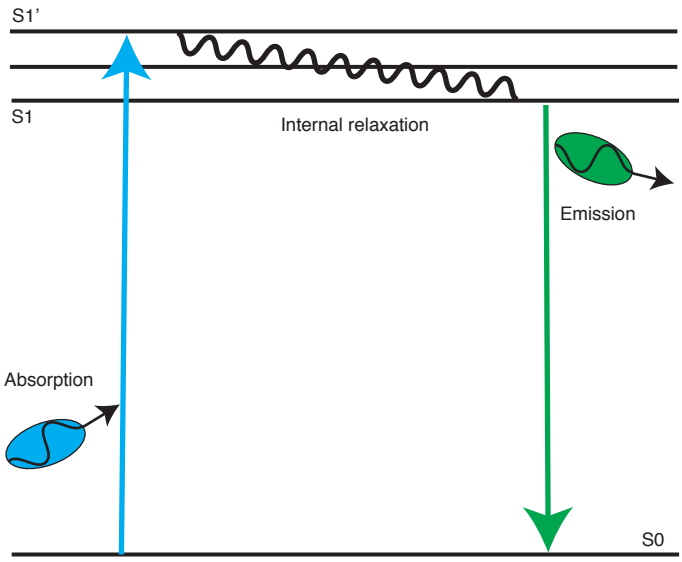


Figure 1.17: A Jablonski diagram of the electron transitions involved in fluorescence. First, a photon is absorbed by a molecule, transitioning from the ground state S0 to excited state S1' (or higher) The molecule then transitions to the lowest-energy level of state S1 by internal relaxation. Finally, the molecule transitions from S1 back to the ground state, releasing a photon as it does so. In fluorescence, the emitted photon is of longer wavelength than the photon absorbed.

For fluorescent emission to occur, photon energy must be at least enough for the molecule to transition from the ground state, S_0, to the first singlet excitation state, S_1. The molecule then relaxes to the ground state in a two-stage process: first, the molecules relaxes to the lowest-energy level of S_1 by internal conversion or vibrational relaxation. This process takes a picosecond or less, and does not result in radiance emission. Second, after a period of nanoseconds, the molecule relaxes from the lowest-energy level of S_1 to the ground state S_0 by emission of a photon. Because this transition releases less energy than the initial excitation, the photon released is of longer wavelength than the photon observed. A Jablonski diagram showing the electronic transitions in fluorescence can be seen in 1.17.

In fluorescence microscopy, the light emitted by excited fluorescent molecules is used to form an image, rather than the light reflected or absorbed by the sample. Fluorescence microscopy allows individually-tagged subunits to be visualised with a high degree of specificity, and the detection of individual fluorescent molecules can be used to bypass the natural diffraction limits of light microscopy. Biological subunits, such as proteins or DNA, can be made fluorescent by the addition of dyes;

additionally, proteins can be fused with a naturally fluorescent protein such as GFP.

1.8.3 Fluorescent Proteins

The green fluorescent protein (GFP) was first isolated in 1962 from the jellyfish *Aequorea victoria* [138]. Since then, it has become one of the most useful tools in biology with many different uses [82]. Many different derivatives have been engineered from the original wild-type GFP (wtGFP): stability and specificity has been greatly improved (such as in "enhanced" eGFP), and fluorescent proteins are now available which span the entire visual spectrum [136]. Due to its high stability and independence in folding, GFP can be used to "tag" proteins of interest. Typically, the gene for GFP or a derivative is fused with that of the protein of interest so that it forms a new domain at the N- or C-terminal end of the polypeptide. Fused GFP typically does not interfere with tagged protein activity. Although wild-type GFP is dimeric, most derivative proteins are monomeric, allowing them to be used as tools for studying stoichiometries of protein complexes.



Figure 1.18: The structure of eGFP. *(Left)* A side-view of the molecule. β-sheets are coloured in green; α-helices in red. *(Right)* A top-down view. The fluorophore can be seen in the protein centre. Structure solved by Royant *et al*, PDB number 2Y0G [128].

The structure and mechanism of GFP has been well-studied. A ribbon diagram can be seen in 1.8.3. 11 strands of β-sheet form a cylindrical β-barrel around the outside of the protein. Two short α-helices cap the top and bottom of the β-barrel, and provide a scaffold for the fluorophore in the centre of the protein [167]. The fluorophore is spontaneously formed from three residues (Ser65, Tyr66 and Gly67 in

wtGFP), in the presence of molecular oxygen. Complete maturation of GFP after translation typically takes 20-30 minutes [31].

1.8.4 Total Internal Reflection Fluorescence (TIRF) Microscopy

The phenomenon of total internal reflection occurs when a light wave strikes a boundary between two media with different refractive indices n_1 and n_2 (for example, glass and air). If the angle of incidence is greater than a "critical" angle, θ_c, it will not refract, but instead undergo total internal reflection. This critical angle can be calculated using the formula:

$$\theta_c = \sin^{-1}(\frac{n_1}{n_2})$$

An important side effect of total internal reflection is the generation of an evanescent electromagnetic field at the boundary surface, which propagates into the less dense medium. Depth of propagation, δ, is a function of incidence angle θ_i, refractive index ratio $(\frac{n_1}{n_2})$ and incident light wavelength λ_i. Wave intensity, I_z, decreases exponentially with distance z. These two parameters are defined by the formulae:

$$\delta = \frac{\lambda i}{2\pi n_1 \sqrt{\sin^2\theta_i - (\frac{n_1}{n_2})^2}}$$

$$I_z = I_0 e^{-(\frac{z}{\delta})}$$

For biological samples, this results in an evanescent wave which typically propagates only ∼100 nm into the cell. This level of propagation is ideal for imaging samples on cell surfaces, as only fluorophores within the 100 nm field are excited [6]. The lack of whole-cell excitation results in a high signal-to-noise ratio compared to conventional fluorescence microscopy, allowing detection of single fluorescent molecules *in vivo* [131].

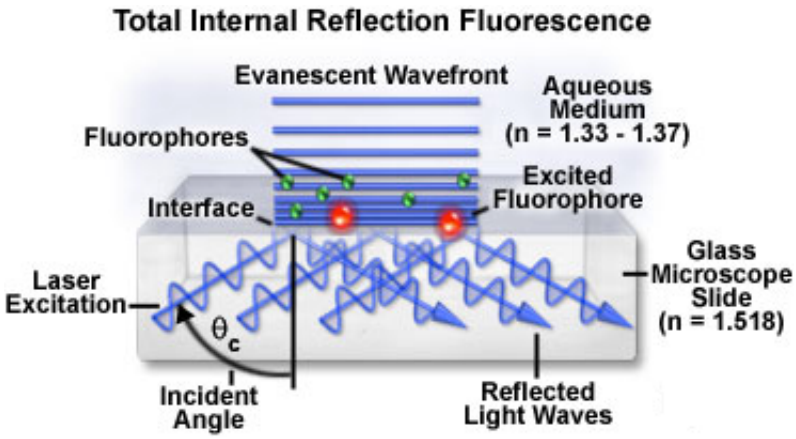


Figure 1.19: A cartoon showing the basic principle of TIRF microscopy. Totally internal reflected light waves generate an evanescent wavefront, which can excite fluorophores at the interface between two different media (in this case, water and glass). Taken from Nikon Microscopy U.

1.9 Aims of This Study

Given that the number of stators in a flagellar motor is variable, and that stators are capable of entering and leaving functioning motors, a question arises: how do *pmf* changes affect *E. coli* motor dynamics *in vivo*? The aims of this thesis were:

- To construct a pR-based *pmf* generation system which could be used for detailed investigations into motor function
- To test whether fine control of wild-type motors can be carried out *in vivo* by varying *pmf*
- To use this ability to investigate the relationship between stator binding and the *pmf* *in vivo*
- To directly monitor changes in the motor at different *pmf* levels by analysis of fluorescently-tagged motor components using TIRF microscopy.

Chapter 2

Materials and Methods

2.1 Strains and Plasmids

2.1.1 Bacterial Growth Conditions

The strains and plasmids used in this study are summarised in Tables 2.1 and 2.2 respectively. All *E. coli* strains were grown for propagation aerobically in Luria-Bertani medium (LB-broth) (Appendix A), with shaking, or on solid LB-agar plates (Appendix A) at 37 °C. Cells for motility experiments were grown aerobically in tryptone broth (TB) at 30 °C. Antibiotics, when required, were added to growth media at the following concentrations:

- Ampicillin 100 μg ml^{-1} in distilled water
- Chloramphenicol 34 μg ml^{-1} in ethanol
- Kanamycin 25 μg ml^{-1} in distilled water

***E. coli* Strain**	**Description**	**Source**
XL-1 Blue	Cloning strain for pUC19 and pBAD derivatives	Stratagene
BW25142	Strain used for cloning pDS132 and derivatives. *pir^{+} (-116)* mutant	[54]
RP437	Wild-type *E. coli* strain for chemotaxis.	[112]
RP5232	Δ*cheY* variant of RP437	[112]
JHC1	*gfp-motB* (parental strain RP437)	[79]
JPA945	*fliM-yPet* (parental strain RP437)	[36]
JPA941	*cyPet-MotB* (parental strain RP437)	[35]
MT02	*fliCst* (parental strain RP437)	This study
MT03	*fliCst* (parental strain RP5232)	This study
MT04	*fliCst* (parental strain JHC1)	This study
MT05	*fliCst* (parental strain JPA945)	This study
MT06	*MotA-eGFP* (parental strain RP437)	This study

Table 2.1: Strains used in this study.

Plasmid	Description	Source
pDS132	suicide vector, Cm^r; *sacB, repA* (R6K) origin of replication	[118]
pET28-pR	Expression vector containing *pRsar86*; Amp^r	Jan Liphardt
pBAD-HisC	pBR322-based expression vector; introduces a C-terminal × His-tag. Amp^r.	Invitrogen
pBAD-pR	*pRsar86* cloned into pBAD-HisC	This study
pQE-60	P_{tac}-based expression vector; introduces a C-terminal 6 × His-tag. Amp^r.	Qiagen
pQE-pR	*pRsar86* cloned into pQE-60	This study
pDS-*fliC*st	pDS132 carrying ∼500 bp upstream and downstream of the start and end of *fliC*st	This study
pEGFP-N1	Plasmid containing the gene for enhanced GFP (eGFP)	BD Biosciences
pDS-Mot-GFP-A	pDS132 variant which introduces *eGFP* after base 217 in *motA*	This study

Table 2.2: Plasmids used in this study

2.1.2 Storage of Strains

E. coli strains were preserved for long-term storage by making a 1:1 mixture of stationary-phase culture and 50 % sterile glycerol solution. Aliquots were flash-frozen in liquid nitrogen and stored at -80 °C.

2.2 Genetic Techniques

2.2.1 DNA Manipulation

DNA Preparation

Plasmid DNA was extracted from stationary-phase *E. coli* cultures using either the QIAPrep Spin Miniprep kit or the HiSpeed Plasmid Midiprep kit (both Qiagen), following the provided protocols. Chromosomal *E. coli* DNA was extracted using the GenElute Bacterial Genomic DNA Kit (Sigma), following the provided protocols.

Restriction Digests

All restriction digests were carried out using enzymes from New England Biolabs, following the protocols provided. A reaction mixture of 30-50 μl was made up containing 2-10 units of each enzyme, reaction buffer, DNA and BSA if required.

Gel Electrophoresis

Multi-purpose agarose (Roche) was made up between 0.8 % and 1.5 % in 0.5 × TBE buffer (Appendix A), depending on the sizes of fragments to be separated. Fragments were electrophoresed between 80-150 V. Gels were stained for 15 minutes in 1 ng ml^{-1} ethidium bromide and visualised on a UV transilluminator (λ_{max} 360 nm).

Purification of DNA Fragments

DNA fragments were purified from agarose gels or from solution using the GenElute Gel Extraction Kit (Sigma), following the protocols provided.

DNA Ligation

Insert and vector DNA were mixed in a 1:3 - 1:6 ratio with 1μl DNA ligase (NEB) and the appropriate buffer to a total reaction volume of 20 μl. The reaction mixture was incubated for 16 hours at 16 °C, then transformed into previously-prepared competent cells.

Polymerase Chain Reaction

Reactions contained 100 ng DNA template, 200 pmol of each primer (Sigma-Genosys), 25 nmol mixed dNTPs, and 10 units *pfu* DNA polymerase with provided buffer (Promega) to a volume of 50 μl. The following reaction program was run in a TC-3000 thermocycler (Techne):

1. Initial denaturation – 98 °C × 10 minutes
2. (a) Denaturation – 98 °C × 2 minutes
   (b) Annealing – 55 °C × 90 seconds
   (c) Extension – 72 °C × 1 minute per 500 bp amplified
3. Repeat Step 2 30 times

4. Final extension – 72 °C × 10 minutes
5. Hold at 4 °C

Overlap Extension PCR

Reactions were carried out as for conventional PCR, except that the template comprised two linear DNA strands from previous PCRs. The two linear DNA strands were designed to act as primers for each other, resulting in the synthesis of a single long DNA molecule. A visual representation of this method can be seen in Figure 2.1.

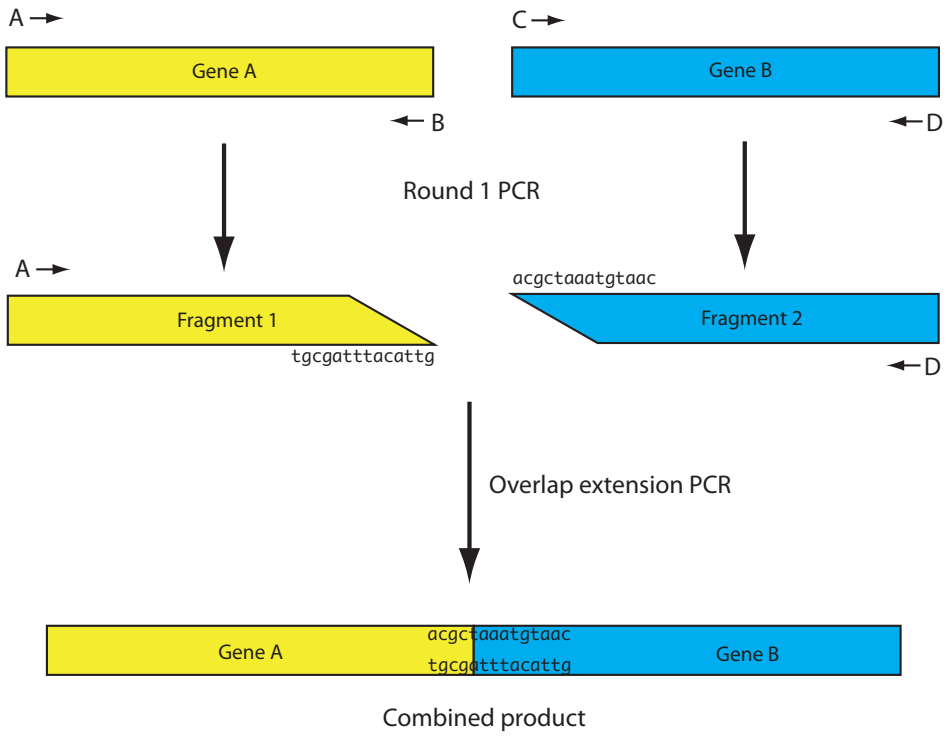


Figure 2.1: The principle of overlap extension PCR. In this example, a single PCR fragment containing two different genes is created. Round 1 amplifies the two genes using a standard PCR protocol. In overlap extension PCR primers B and C are designed to be palindromic with respect to one another; this allows fragments 1 and 2 to act as "super primers" for one another in a second PCR reaction which joins the two fragments together. The resulting product is a single DNA molecule which is a fusion of genes A and B.

DNA Sequencing

All DNA sequencing was done by the Automated DNA Sequencing Service provided by Geneservice (Source BioScience). The BigDye dye termination method (PE Biosystems) was used on a 3730 DNA sequencer (Applied Biosystems). Sequences were analysed using the Staden software package and analysed using Clone Manager (Sci Ed Central).

Preparation of Dioxygenin-Labelled Probes for Southern Blots

DNA fragments used as probes for Southern blots were purified as above and labelled using the DIG DNA Labelling Kit (Roche Diagnostics), following the provided protocol.

Southern Blots

E. coli chromosomal DNA was purified as above, digested with appropriate restriction enzymes and electrophoresed on a 1 % agarose gel. Separated DNA was then denatured, neutralised and transferred to a Hybond-N membrane by capillary transfer as described in [132]. Membrane containing DNA was dried, UV-fixed and pre-hybridised for 4 hours. Probe hybridisation was done in a hybridisation oven (Hybaid) at 68 °C overnight. Probe binding was visualised using the DIG Nucleic Acid Detection Kit (Roche Diagnostics) following the provided protocol.

2.2.2 Transforming *E. coli*

Chemically Transforming *E. coli* Strains

Transformation of DNA by the rubidium chloride method was used during cloning or to introduce expression vectors into *E. coli* cells.

To prepare RbCl-competent cells, 1 ml of *E. coli* stationary-phase starter culture was inoculated into 50 ml of LB-broth. The culture was incubated until OD_{600} 0.4, then transferred to a falcon tube and incubated on ice for 15-30 minutes. Cells were centrifuged at 1000 × *g* for 10 minutes at 4 °C, resuspended in 16 ml ice-cold TFB I (Appendix A) and incubated at 4 °C for 1 hour. Cells were centrifuged again at 750 × *g* for 10 minutes at 4 °C, then resuspended in 2 ml ice-cold TFB II (Appendix A). 200 μl aliquots of this mixture were flash-frozen in liquid nitrogen and stored at -80 °C.

RbCl-competent cells were transformed either with 0.5 μg plasmid DNA or, for ligations, the entire ligation mixture. DNA was incubated with an aliquot of competent cells for 30 minutes at 4 °C, then heat-shocked at 42 °C for 2 minutes. 1 ml of LB-broth was added to the transformation mix, which was then incubated at 37 °C for 1 hour. The transformation mix was then spread onto LB-agar plates containing appropriate antibiotics and incubated overnight at 37 °C.

Transforming *E. coli* Strains by Electroporation

Transformation of DNA by electroporation was used to introduce pDS132 derivatives into *E. coli* cells for gene replacement.

Electro-competent cells were prepared using the method described in [132], flash-frozen in liquid nitrogen and stored at -80 °C. Cells were transformed with 2-6 μg plasmid DNA. The cell-DNA mix was incubated at 4 °C for 2 minutes and transferred to a pre-chilled 2 mm electroporation cuvette (Geneflow). An electrical pulse of 2400 V, 25 μF and 200 Ω was applied to electroporate the cells. 1 ml SOC medium (Appendix A) was immediately added to the electroporation mix, which was then transferred to an Eppendorf tube and incubated at 37 °C for 2 hours. The electroporation mix was then spread onto LB-agar plates containing appropriate antibiotics and incubated for 36 hours at 37 °C.

2.2.3 Gene Replacement with pDS132

Cloning of pDS132 derivatives was carried out in strain BW25142, which is capable of replicating plasmids containing the R6K origin of replication [54]. pDS132 derivatives containing target sequences were transformed into the appropriate background strain by electroporation.

After electroporation and incubation, cells were grown on LB-agar plates with chloramphenicol at 37 °C for 36 hours. This step selected for vector integration onto the host cell chromosome. Resulting colonies were picked and subcultured in LB with chloramphenicol at 37 °C overnight. 5 μl of this culture was subcultured in LB-sucrose (Appendix A) overnight to stationary phase. The overnight culture was subcultured into fresh LB-sucrose three times in succession. This step selected for the second cross-over event, and ensured that cells excised the vector from the chromosome. 100 μl of the final overnight culture was serially diluted in 10 mM $MgSO_4$ and spread-plated on LB-sucrose agar plates, which were incubated overnight at 37 °C. 50 colonies from these plates were replica-plated on LB-agar with chloramphenicol

col and LB-sucrose plates to select again for vector excision. Gene replacement was tested for by Southern blotting and PCR, and confirmed by DNA sequencing of the relevant region. A visual representation of this method is shown in Figure 2.2.

2.3 Phenotypic Analysis of *E. coli* Strains

2.3.1 Soft Agar Swim Plates

Swarm plates were made using TB plus 0.25 % bacto-agar (BD Biosciences). Plates were poured and left to set at 30 °C 2 hours prior to inoculation. 5 μl drops of overnight cell culture were gently dropped onto the plate surface to inoculate, and plates were incubated at 30 °C. Swarm diameter was measured after 12 hours. All swarm, plate assays were conducted in triplicate, and comparisons between strains were only made between those inoculated on the same plate.

2.3.2 Preparing Cells for Microscopy

Preparing Motile Cells

E. coli cells were grown in TB at 30 °C to mid-log phase (OD_{600} 0.5 - 0.6). Cells were centrifuged and resuspended in an equal volume of *E. coli* motility buffer (Appendix A). 1 ml of cell suspension was forced 40 - 60 times between two syringes with 26-gauge needles connected by polyethylene tubing (12 cm long, 0.58 mm inner diameter). The turbulent flow inside the tubing shears cells' flagellar filaments at a random point along their length. This method allows cells to be attached to a glass slide by a single short filament, and ensures attached beads remain close to the cell body. After shearing, the cell suspension was centrifuged and resuspended in 0.2 - 1 ml motility buffer to remove flagellar fragments.

Tunnel Slides

Tunnel slides are glass slides where the coverslip is attached by a "tunnel" of two strips of adhesive running along the longitudinal axis. This allows different solutions to be flowed along the coverslip For a visual representation, see Figure 2.3. Two types of adhesives were used: double-sided sticky tape (3M) was used in slides for bead assays, and high vacuum grease (Dow Corning) was used in slides for fluorescence microscopy. Coverslips were cleaned by heating to remove organic matter, then placed on the adhesive and firmly pressed down, forming a tight seal.

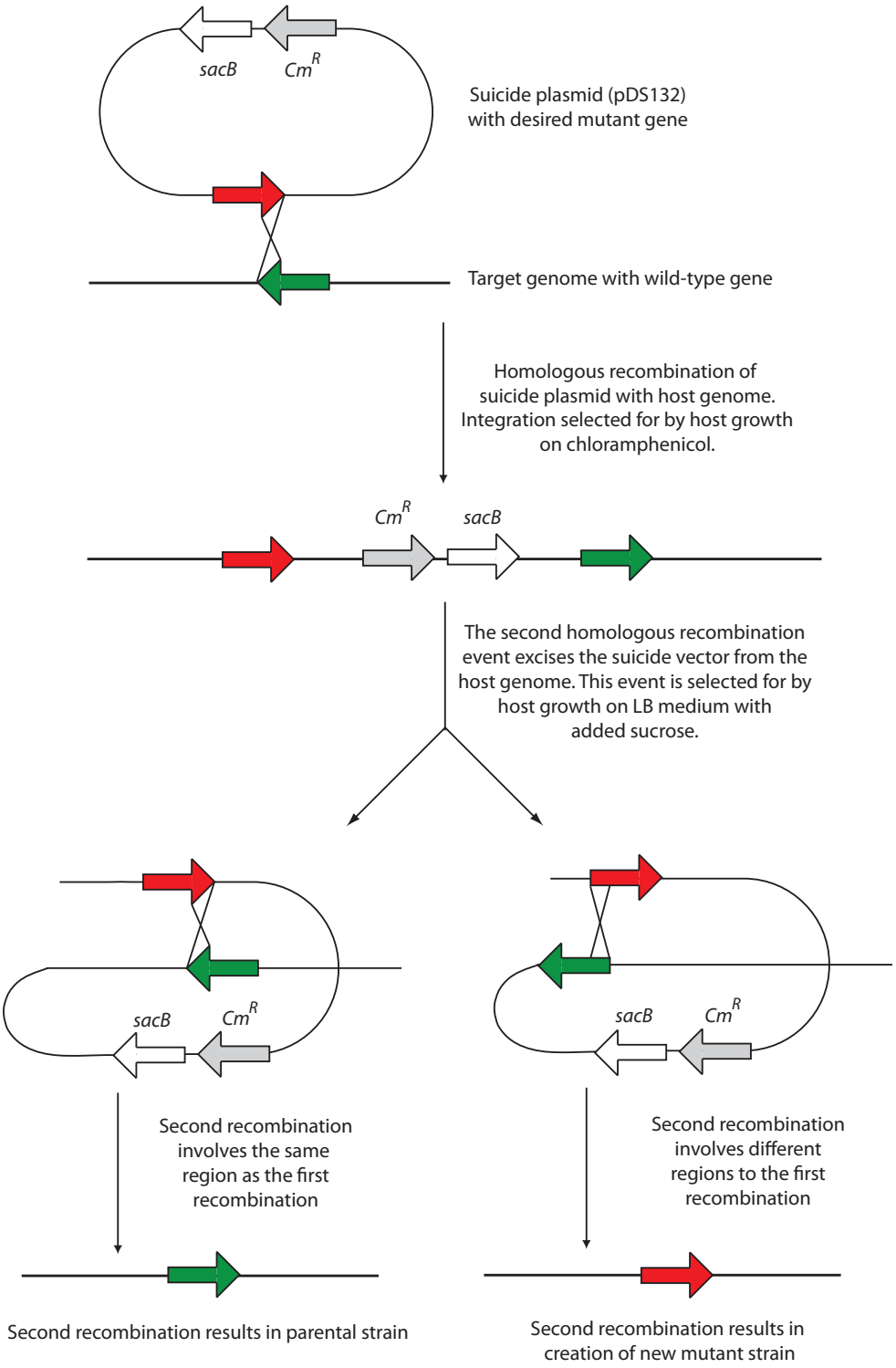


Figure 2.2: The process of gene replacement by homologous recombination in *E. coli*. There are two possible outcomes, both equally likely: either the desired gene is inserted onto the host chromosome, or the second round of homologous recombination results in reversion to the parental genotype.

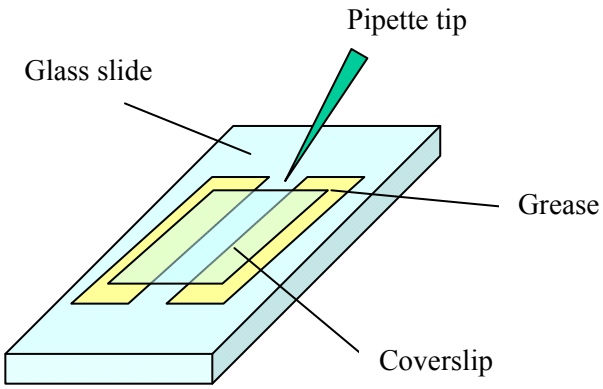


Figure 2.3: A diagram of a tunnel slide, with high-vacuum grease used as a seal. Typical tunnel volume is ~ 25 μl.

Flow Cells

Flow cells allow buffer exchange along the coverslip while attached cells are being observed. Two holes were drilled into a coverslip 20 mm apart. Teflon tubing was threaded through the holes, and fixed in place with epoxy resin. Excess tubing was removed with a razor. Slides for observation were made by forming a tunnel between the two holes with high vacuum grease. A clean glass coverslip was placed on the grease and firmly pressed down. Different solutions could then be flowed along the tunnel through the tubing, either by gravity flow or by attached syringes.

Tethered Cells

Strains used in tethered cell studies expressed the mutant flagellin protein FliCst [76], which enabled flagella to attach to glass coverslips. 50 μl of sheared cells were flowed through a tunnel slide or flow cell, which was inverted and left for 10 - 15 minutes. Motility buffer was then flushed through the slide to remove loose cells.

Bead Assay

All strains used in bead assay studies expressed mutant flagellin FliCst which enabled polystyrene beads to attach to flagellar stubs. 50 μl 0.1 % (w/w) poly-L-lysine (Sigma) was flushed through a tunnel slide and incubated for 2 minutes, after which 100 μl motility buffer was flushed through. This allowed cell bodies to attach to the glass coverslip. Sheared cells were flushed through the slide, which was inverted and left for 10 minutes. Motility buffer was flushed through to remove loose cells,

followed by a polystyrene bead solution (0.05 % w/w in motility buffer, Polybead Polysciences). This was left for 10 minutes to allow beads to attach to flagellar stubs. A final flush with motility buffer removed any unattached beads.

2.4 Microscopy

2.4.1 TIRF Microscopy

A home-built (by Dr Nicolas Delalez) inverted fluorescence microscope was used, with an Plan Fluor 1.45 NA oil-immersion 100 × objective lens (Nikon) and an E-503.00 piezoelectric *xyz* nanopositioning stage (Physik Instrumente). Bright-field illumination used a fibre-coupled lamp. Two different lasers were used for fluorophore excitation: for YPet excitation, a TEM00 plane-polarised continuous-wave 532 nm DPSS laser (Laser2000, UK), filtered, expanded three times and focused onto the back-focal plane of the microscope objective using a dichroic mirror (530 nm long pass) was used. For eGFP excitation, a COL-002 plane-polarised continuous-wave 473 nm DPSS laser (Laser2000, UK) was used. A photograph of the microscopic apparatus can be seen in Figure 2.4.

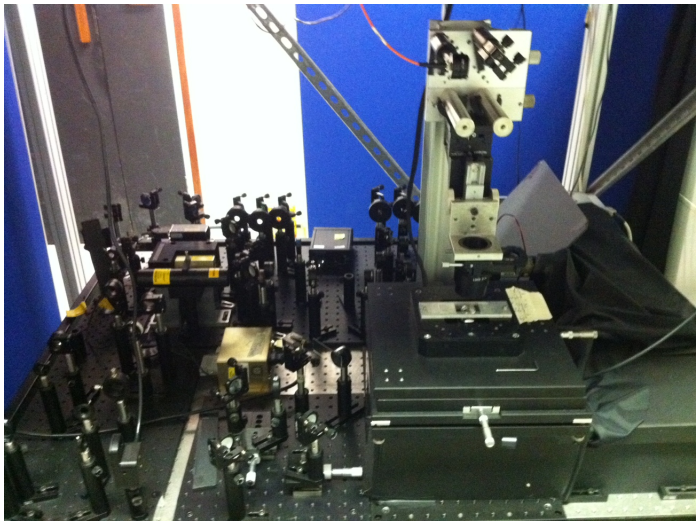


Figure 2.4: A photograph of the custom-built TIRF microscope used in this study.

2.4.2 Microscopy and BFP Interferometry of Attached Beads

The microscope apparatus used in these experiments was designed and built by Dr T Pilizota [119], comprising a home-built inverted microscope and a 1064 nm Ytterbium fibre laser (IPG Photonics). Bead detection was done by BFP (back-focal plane) interferometry, focussing the laser into the specimen plane using the objective with the condenser collimating the beam onto a quadrant photodiode in the BFP of the condenser. A DSP board installed in a host computer was used for data acquisition and laser control via acousto-optical deflectors (AODs). Sampling rate in all experiments described was 2000 Hz, giving a maximum time resolution of 0.5 ms. For a diagram of the apparatus used, see Figure 2.5. The microscope was adapted for experiments with pR-expressing cells by adding a 532 nm Nd:YVO_4 laser in line with the illumination path. A programmable shutter (Thorlabs) was installed in the laser path, allowing illumination to be controlled by computer.

2.4.3 Data Analysis

Motor Speed

Two methods were used to measure the rotation of beads attached to flagellar filaments. In the power-spectrum method, 1 second windows of Px and Py data were combined to form a complex signal every 0.1 s [129]. One consequence of using this method is that speeds are converted to absolute values, so that negative (CW) motor speeds are converted to positive speeds. Motor switching event therefore appear as transient ($\sim< 1ms$) motor stops. Speed resolution was 1 Hz with a time resolution of 0.1 s. The program used to convert Px and Py data to absolute speeds was written by Dr. Teuta Pilizota.

In the $d\theta/dt$ method, ellipses were fit to beads' trajectories using a downhill simplex method. This method relies on a regular bead trajectory for correct ellipse fitting; traces with irregular trajectories (judged by eye) were discarded. Angular velocity of beads (ω) was calculated from angle/time data ($\omega = d\theta/dt$), and fitted with a 1-200 point sliding window filter. The program used to convert Px and Py data to angle/time data was written by Dr. Richard Berry.

The $d\theta/dt$ method was used for the bead angle/time studies and resurrection averaging studies described in Chapter 5; all other studies used the power spectrum method to calculate motor speed.

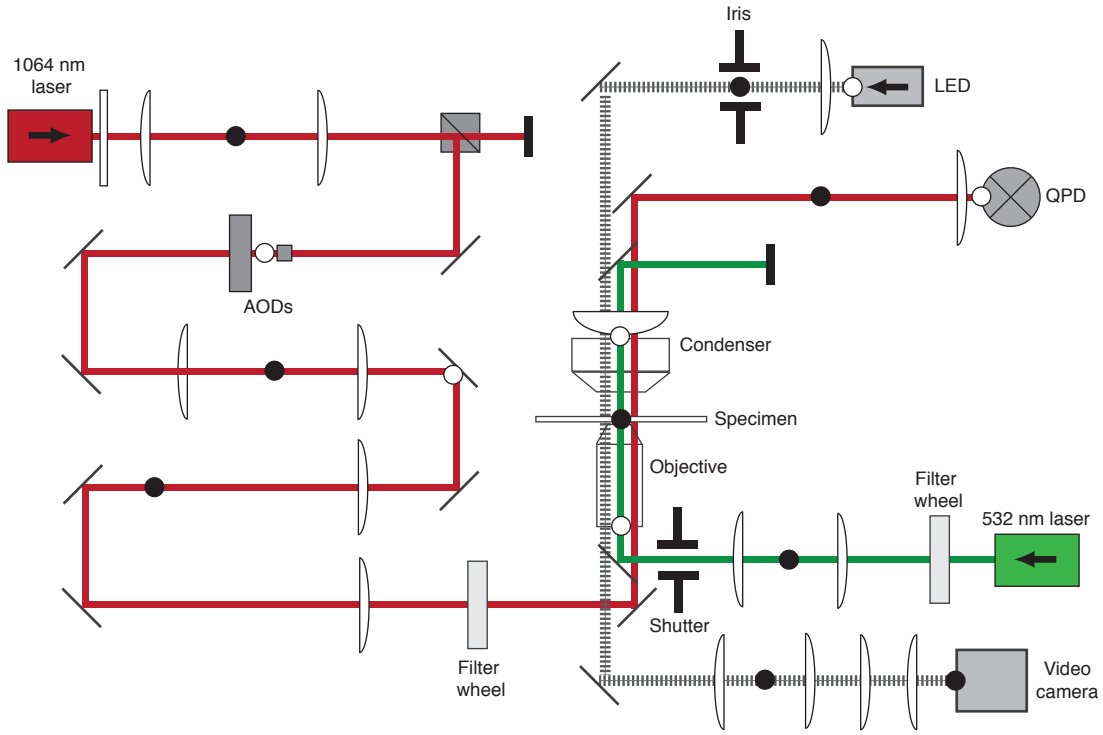


Figure 2.5: A diagram of the microscope apparatus used in these experiments. Bright-field imaging used an LED, high numerical-aperture condenser, 100× oil-immersion objective (both Nikon) and a high-sensitivity CCD video camera (Watec). BFP interferometry used the 1064 nm laser to generate a signal. Laser intensity was varied using the laser diode current and the inline ND filter wheel. For experiments with light-powered *E. coli*, illumination was provided using an attached 532 nm laser focussed on the specimen plane. Laser intensity was varied using the inline ND filter wheel. Illumination was controlled using a computer-controlled shutter in line with the laser path. Black and white circles on the diagram refer to the front and back image planes respectively.

Fluorescence Data

Image files from TIRF microscopy were analysed using the proprietary Andor iXon software, which allowed relative intensity of fluorescent spots and other regions of interest to be calculated and compared.

Chapter 3

Development of a pR-Based Motor Assay

3.1 AIMS

The flagellar motor relies on an ion-motive force (*imf*) as a power source to drive flagellar rotation. Previous studies into the relationship between *imf* and the *E. coli* motor have taken one of two approaches:

1. **Powering the motor with an external voltage source.** In this approach, filamentous *E. coli* cells are drawn into a micropipette and made permeable either by treatment with gramicidin S [48] or ablation of the cell membrane with a focused laser [50]. This method allows investigation of wild-type motors at well-defined *pmf*, but has several disadvantages. The invasiveness of this technique means that it is difficult to investigate the relationship between the motor and its parent cell. High-resolution analysis of motor behaviour is also difficult, as normal tethered cell or bead assays cannot be used in conjunction with the micropipette.

2. **Chimeric *E. coli* motors.** Chimeric motors are created by replacing the N-terminal transmembrane helix of *E. coli* MotB with its counterpart from *V. alginolyticus*, PomB. Expression of the resulting chimera, PotB, allows the *E. coli* motor to be powered by transit of sodium ions. Using this method, *smf* in intact cells can be easily varied by varying the Na^+ concentration of the external buffer. However, there are key differences between the wild-type and and chimeric motors: the chimeric motor generates much more torque, and protein copy numbers vary due to the necessity of plasmid expression. Changes in *smf* are also limited to the speed of buffer exchange, and the boundary between two different Na^+ concentrations is ill-defined. Recent data also suggests that chimeras are more unstable than native stators (R. Berry, personal communication).

In 2007, Walter *et al* showed that the light-driven proton pump proteorhodopsin (pR) could establish and maintain a *pmf* in intact wild-type cells. Native *pmf* generation was inhibited by oxygen depletion and addition of azide, and cells were induced to express pR from an IPTG-inducible expression system. In this way, pR was made to act as the sole *pmf* source for the cell. A diagram showing proton influx and efflux in cells where pR is the sole source of *pmf* can be seen in Figure 3.1. By expressing pR, "light-powered" cells could be made to start and stop their flagellar motors by variation of the illumination level. Investigation of the motor-*pmf* relationship using pR would potentially solve many problems with previous

methods. *pmf* could be quickly and reversibly altered in wild-type cells, under conditions where motor behaviour could be closely monitored using attached beads or a tethered cell assay.

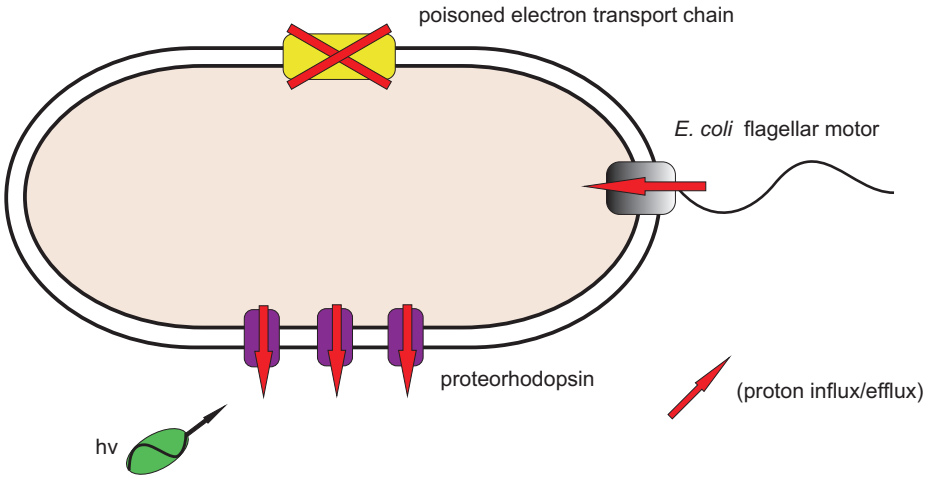


Figure 3.1: A cartoon diagram detailing how expression of pR can be used to power the flagellar motor. If a respiratory poison is used to inhibit native *pmf* generation, the flagellar motor rotates using only *pmf* generated by illuminated pR.

This chapter describes the creation of a pR-based control system for wild-type *E. coli* flagellar motors, compatible with the back-focal-plane interferometry techniques previously used to investigate motor behaviour.

3.2 Construction of Strains

E. coli strains used in flagellar motor studies often carry a deletion or transposon insertion of the wild-type *fliC* gene, which is complemented by expression of a mutant flagellin, FliCst, from an inducible plasmid [13] [125] [145]. *fliC*st is an engineered mutant gene which contains a deletion from bases 735 to 903 [76]. Expression of FliCst results in "sticky" flagella, which are hydrophobic due to an exposed flagellar filament core. "Sticky" flagella are able to bind to glass coverslips and polystyrene beads, allowing easy analysis of flagellar rotation by BFP interferometry or tethered cell analysis. The use of "sticky" flagellin is much more efficient and cost-effective than the alternative method, where wild-type flagella are made hydrophobic by binding antibodies raised against FliC.

The expression of FliCst from a plasmid, although effective, is sub-optimal. Care must be taken to ensure vector compatibility when planning experiments with other

inducible plasmids. The number of plasmid types which can be accommodated in a single strain is also limited. It was thought that these problems could be solved by replacing the wild-type *fliC* with chromosomal *fliC*st in the *E. coli* wild-type strain RP437 and its non-switching motor derivative, RP5232 ($\Delta cheY$). These strains could then be used in further studies, and could also be used as parent strains for later fluorescently-tagged mutants. A suicide vector, pDS-*fliC*st, had been designed in a previous study [25] to replace wild-type chromosomal *fliC* with *fliC*st, producing the "sticky" flagellin phenotype. However, this plasmid had since been lost and had to be reconstructed using the process described below.

3.2.1 Reconstruction of Plasmid pDS-*fliC*st

pDS-*fliC*st was reconstructed using the design of Chandler [25]. The *fliC*st gene was taken from *E. coli* strain PS2589. A region of the chromosome of *E. coli* strain PS2589 containing *fliC*st was amplified by PCR using primers *fliC1* and *fliC2* which were designed to anneal ∼500 bases upstream and downstream of *fliC*st. Primer sequences can be found in Appendix B. These adjacent regions of homology allow the construct to be inserted into the chromosome of the target strains by homologous recombination. The resulting PCR fragment was purified, digested with *Sph*I/*Sac*I and ligated into plasmid pDS132 cut with the same enzymes. A diagram of this process can be seen in Figure 3.2. The resulting plasmid, pDS-*fliC*st, was sequenced before being used to insert *fliC*st onto the genomes of RP437 and RP5232.

3.2.2 Incorporation of pDS-*fliC*st onto the Genome

Cells of strains RP437 and RP5232 were transformed with pDS-*fliC*st using the method described in Section 2.2.2. Successful incorporation of pDS-*fliC*st, and subsequent loss of the vector backbone, were selected for using the method described in Section 2.2.3. Briefly, pDS132 was introduced into the host strain by electroporation, where it incorporated onto the host genome by homologous recombination. Incorporation was selected for by testing for Cm-resistance. A second homologous recombination event (vector excision) was selected for by growing the cells in LB containing sucrose; cells which retained vector were killed, as pDS132 contains the *sacB* gene which confers sucrose toxicity.

Correct replacement of *fliC* with *fliC*st was tested for by Southern blotting using the protocol described in Section 2.2.1. Preparations of genomic DNA from 50 successful Cm^S Suc^R isolates of RP437 and RP5232 following gene replacement were

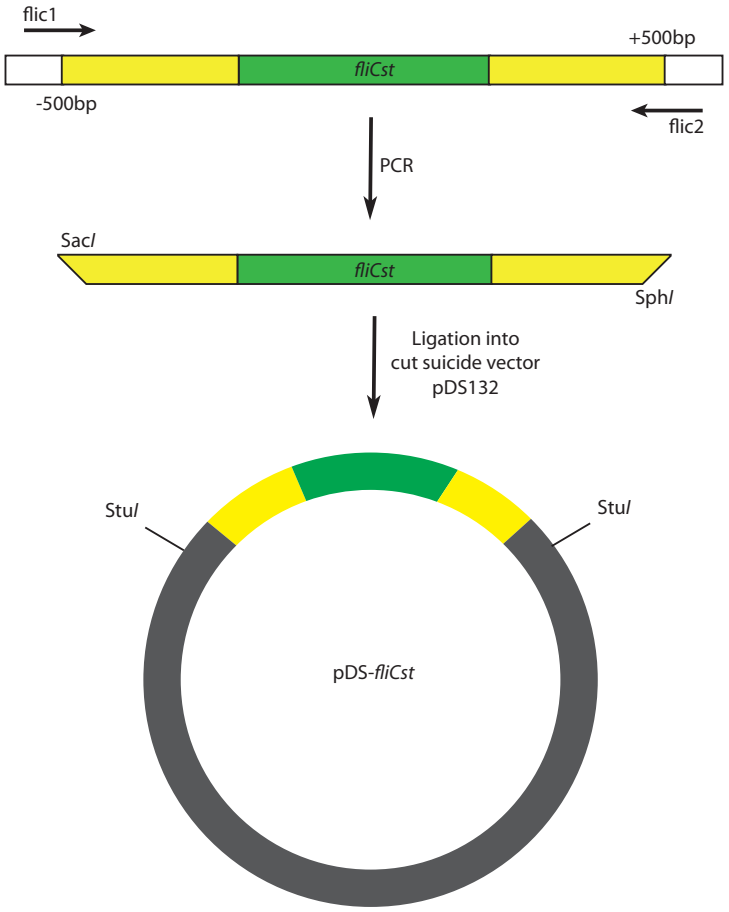


Figure 3.2: A diagram detailing the construction of pDS-*fliC*st, a suicide vector designed to replace wild-type *fliC* with the mutant variant *fliC*st. The gene was amplified with 500 bp flanking regions to enable insertion onto the host genome and ligated into the suicide vector pDS132.

digested with *Stu*I, producing a genomic fragment which contained most of the *fliC* gene. Digests were separated by gel electrophoresis and transferred to a membrane, which was hybridised by a 500 bp DNA probe constructed by digestion of pDS-*fliC*st with *Fsp*I/*Nde*I. A positive control of pDS-*fliC*st was run on all gels.

Successful integration resulted in observation of a band of the correct size (1230 bp) after probe development. After further confirmation of integration using DNA sequencing, the new strains MT02 (parental strain RP437, *fliC*st) and MT03 (parental strain RP5232, $\Delta cheY$ *fliC*st) were frozen and stored at -80 °C.

3.2.3 Phenotypic Characterisation of Strains MT02 and MT03

Motility of Strains MT02 and MT03

The motility of strains MT02 and MT03 was first tested using a standard soft agar swim plate analysis as described in Section 2.3.1. However, neither MT02 nor MT03 displayed any degree of swimming compared to RP437. A graph of mean swarm diameter after 12 hours for strains MT02, MT03 and RP437 can be seen in Figure 3.3. This was corroborated by observation of planktonic cells under a light light microscope, which appeared to move by Brownian motion only. Lack of swarming ability was unsurprising, as flagella composed of FliCst are more fragile than those composed of wild-type FliC and are less likely to form a correct flagellar bundle. An alternative method was therefore needed to investigate motor function.

FliCst is expressed to increase the tendency of flagellar filaments to tether to hydrophobic surfaces such as glass slides or polystyrene beads. Tethering ability was tested using a blind comparison between MT02, MT03, RP437 and RP5232. Cells were grown to mid log-phase aerobically with shaking at 30 °C. Tunnel slides containing tethered cells of MT02 and MT03 were prepared using the method described in Section 2.3.2. Briefly, 5 ml cell culture was resuspended in 1 μl motility buffer. Flagella in the resulting cell suspension were "sheared" by passing the suspension through thin tubing. The cell suspension was spun down and resuspended in an equal volume motility buffer; this was the flowed through the tunnel slide and incubated at room temperature for 15 minutes. The tunnel slide was flushed with 50 μl motility buffer to remove loose cells.

For RP437 and RP5232, cells were aerobically grown to mid-log phase in 5 ml TB at 30 °C, centrifuged at 1500 $\times$ g and resuspended in 1 ml motility buffer. Flagella in this cell suspension were sheared as described in Section 2.3.2. The resulting

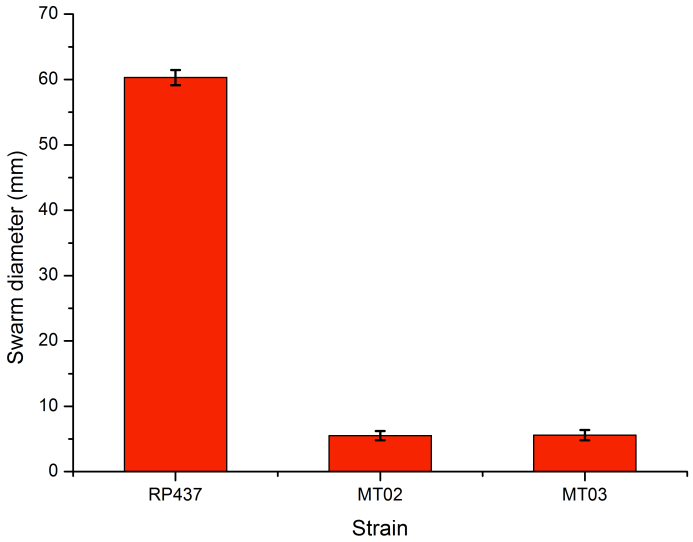


Figure 3.3: Results of soft agar swim plate analysis of MT02 and MT03 motility compared to the wild-type strain RP437, after 12 hours at 30 °C. Neither MT02 nor MT03 were capable of swarming on 0.25 % agar.

sheared cell suspension was centrifuged and resuspended in 1 ml motility buffer to remove sheared flagellar fragments. 200 μl of cell suspension was incubated with 20 μl anti-FliC antibodies (50x diluted in PBS) for 5 min on ice. This mixture was flowed through the tunnel slide, which was incubated and washed as described for MT02 and MT03.

"Tethered" cells are cells which are bound to a glass coverslip by their flagellar filaments. Since the motor continues to generate torque, the cell body can be seen to rotate around the stationary filament. The number of spinning cells in a field of view for each slide was counted for each slide (this was conducted "blind"; that is, the identity of the strain observed was unknown to the experimenter). A graph showing the number of spinning, tethered cells per field of view for each slide can be seen in Figure 3.4. Both MT02 and MT03 displayed a marked increase in tethering ability compared to their parent strains. This confirmed that the mutant flagellar filaments of MT02 and MT03 were able to bind to a hydrophobic surface (in this case, glass), and that the motors in these strains were functional – lack of movement through soft agar was a result of mutant filament expression, rather than a deficiency in flagellar motor itself.

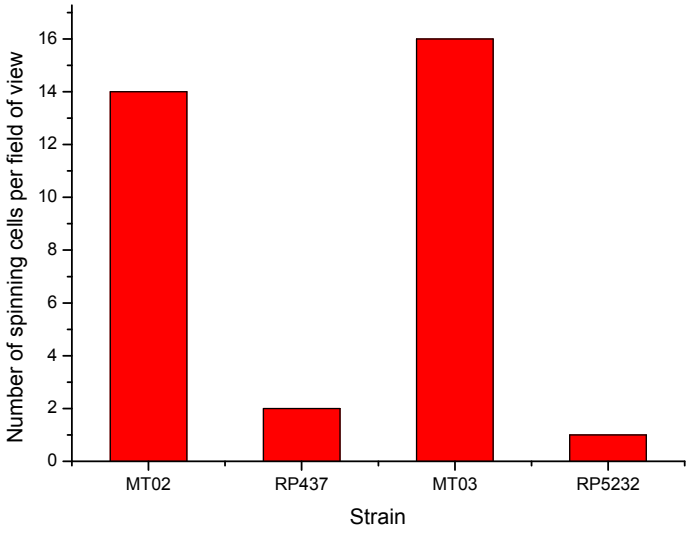


Figure 3.4: Results of test of tethering ability for MT02, MT03, RP437 and RP5232. MT02 and MT03 display much greater tethering ability compared to their wild-type counterparts. Motor speed was similar in all strains (data not shown).

3.2.4 Expression of pR in Experimental Strains

The pR variant used for these experiments was the well-characterised green-absorbing proteorhodopsin (GPR, gene *pRsar86*) from marine bacterial clade SAR86 (a gift from Jan Liphardt, UC-Berkeley). The ability of pR to generate a *pmf* when expressed in *E. coli* was shown by this group by using rotation of tethered cells as a demonstration of *pmf* generation.

pR, as a membrane protein, is potentially toxic when overexpressed – it was therefore important to find an expression system which would provide high yields of healthy motile cells for further analysis. To this end, *pRsar86* was amplified by PCR using primer pairs *pRpQE1-pRpQE2* and *pRpBAD1-pRpBAD2* (for sequences, see Appendix B) and cloned into two different expression vectors, pBAD-HisC and pQE-60. These vectors were chosen as they contain differing promoters: pBAD-HisC contains an *ara* promoter controlled by L-arabinose, while pQE-60 contains a *lac* promoter controlled by IPTG. After confirmation of successful cloning by DNA sequencing, the resulting plasmids pBAD-pR and pQE-60-pR were transformed into cultures of *E. coli* strain MT02.

To determine the optimal point of induction of each plasmid for motility studies, two cultures of each *E. coli* strain (MT02 containing pQE-pR and MT02 containing pBAD-pR) were set up by subculturing 100 μl of overnight culture in 5 ml TB medium. Cultures were grown aerobically at 30 °C with shaking. Since *E. coli* is

unable to synthesise the retinal cofactor required by pR, all-trans retinal was added to the growth medium to a final concentration of 10 μM. The time of induction was varied in the two test cultures of each strain: in one, inducer molecule (IPTG or L-ara) was immediately added, while in the other, cells were left to reach OD_{600} 0.4 before adding inducer.

Cells were prepared for a standard *E. coli* motor bead assay and examined. pR expression from pQE-60 resulted in low levels of motile cells when induced at culture start or at OD_{600} 0.4. The highest proportion of motile pR-expressing cells was found when L-arabinose was added to *E. coli* containing pBAD-pR at OD_{600} 0.4; this expression protocol was therefore used for all other studies involving *E. coli* and pR. Motor speed was later shown to be unaffected by pR expression (see Figure 3.5).

3.3 Light-Powering of *E. coli*

3.3.1 Inhibiting *pmf* Generation in *E. coli*

For pR to act as the sole source of *pmf* in intact *E. coli* cells, native *pmf* generation must be inhibited in some fashion. There are several means of disrupting *pmf* generation in *E. coli*: the membrane can be "short-circuited" by treating cells with a protonophore such as CCCP or FCCP, cells' respiratory apparatus can be inhibited with a poison such as sodium azide, or cells can be starved of small molecules vital for respiratory function (such as molecular oxygen). Consistent nutrient depletion is difficult in *E. coli*, due to its endogenous energy stores [12], and protonophore addition was judged to be unsuitable as it would prevent the cell membrane from supporting a *pmf* from any source. The use of a respiratory poison allows both the ATP synthase (in its role as a source of *pmf*) and the electron transport chain to be quickly and consistently inhibited, preventing native *pmf* generation. This was demonstrated by the original experiment into pR expression in *E. coli* [161].

For these reasons, sodium azide was used as an inhibitor of native *pmf* generation in all experiments which utilised pR as a sole *pmf* source. After cells had been bound to glass coverslips in a tunnel slide or flow cell for analysis, 20 mM sodium azide was flowed through. Motors began to slow down immediately after treatment, typically reaching a complete stop (suggesting complete loss of *pmf*, since *pmf* has been shown to be proportional to motor speed at high load) after 10 minutes. No recovery in motor speed was observed after motor stop, confirming that native *pmf*

generation was probably completely inhibited.

3.3.2 A pR-Based Cell Assay

pR, as a light-driven proton pump, requires constant illumination to maintain a *pmf* across a cell membrane. Illumination of cells for *pmf* generation must therefore be of sufficient intensity at the correct wavelength to maintain proton translocation. The pR variant used in this study, GPR, absorbs best in the green area of the spectrum with an absorption maximum of 540 nm.

The initial study into *E. coli* powered by pR [161] used a halogen lamp equipped with a 540 nm filter to provide the necessary illumination. This method is simple and effective, and can be easily added to a basic light microscopy setup such as that used by Walter *et al.* However, this approach proved to be incompatible with the BFP-interferometry setup which was to be used to measure motor behaviour at high resolutions (described in Section 2.4.2).

A solution was developed where a monochromatic 532 nm green laser was added to the illumination path of the BFP interferometry apparatus. A diagram of the laser path can be seen in Section 2.4.2. The laser was inserted in line with the pre-existing low-intensity lamp used for bright-field imaging, and focussed so that a large "patch" of the microscope field of view was illuminated with green light. A neutral density filter wheel was added so that light intensity at the sample could be easily varied.A wide range of illumination intensities were made possible using this method.

Cells of strains MT02 transformed with pBAD-pR were grown aerobically in TB with shaking at 30 °C. Once cells had reached OD_{600} 0.4, pR expression was induced by addition of L-arabinose to 1 mM and all-trans retinal to 10 μM to the growth culture. Cells were left for one hour (at 30 °C with shaking) to express pR, and then prepared for a standard *E. coli* bead assay (as described in Section 2.3.2). 1 μm polystyrene beads were used so that flagellar motors were subjected to a high-load regime. After preparation, the resulting tunnel slides with bound cells were checked using a bench-top light microscope for the presence of spinning beads attached to functioning motors. 20 mM sodium azide solution (dissolved in *E. coli* motility buffer) was then flowed through the tunnel slide containing cells for analysis, and the slide was immediately transferred to the microscope apparatus for further study.

The microscope field of view was illuminated with red light of intensity 0.1 W m^{-2}. Light of this intensity and colour was chosen as it did not excite pR. The installed 532 nm laser was used to illuminate a portion of the microscope field of view with

light of intensity 100 W m^{-2}. Beads attached to cells in the zone of illumination with 532 nm light rotated steadily, in a similar fashion to cells untreated with azide. Beads attached to cells outside the zone of illumination did not rotate, showing that motor rotation in illuminated cells was a direct consequence of *pmf* generation by pR.

To determine the effectiveness of pR-based *pmf* generation compared to the native *pmf* generation apparatus, the average motor speed of 18 cells powered by pR was measured over one minute by BFP interferometry, using the power spectrum method described in Section 2.4.3. These 18 cells were taken over several sessions to ensure experimental repeatability. Data windows of 1 s were used, giving a maximum speed resolution of 1 Hz.

The average speed over 1 minute of 50 unmodified ("wild-type") MT02 cells and 50 cells of MT02 expressing pR, but without illumination with 532 nm light were also taken. Comparison of motor speed under these three conditions tested whether overexpression of pR resulted in lowered motor speed, and whether pR-based *pmf* generation was capable of replacing the native *E. coli* respiratory apparatus completely in generating a *pmf*.

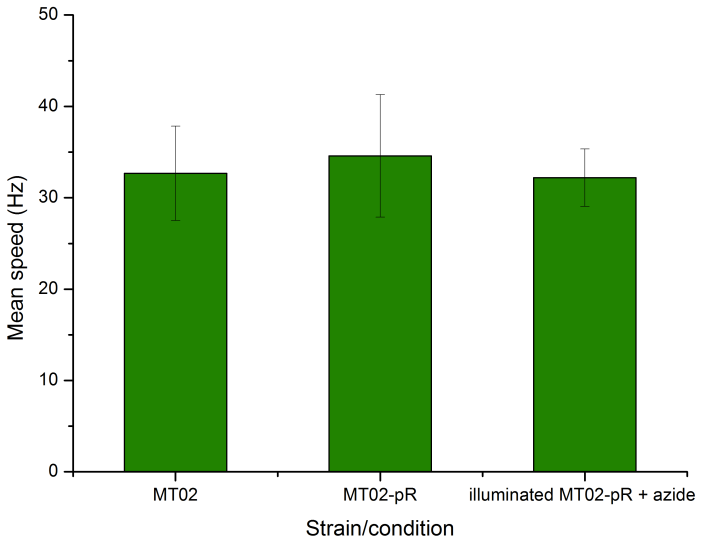


Figure 3.5: Mean speeds of motors in 18 MT02-pR cells where pR was the only source of *pmf* over 1 minute compared to the mean speeds of 50 cells of unmodified MT02 and 50 cells of MT02-pR expressing pR only (without illumination or poisoning).

The average motor speed in MT02 cells powered by pR was measured to be 32±3

Hz. This is similar to the mean motor speed of "wild-type" MT02, (32 ±5 Hz) and MT02 expressing pR without illumination (34±6 Hz). pR was therefore shown to be capable of powering a flagellar motor to the same extent as the native respiratory apparatus.

3.4 CONCLUSIONS

This chapter describes the successful creation of a pR-based *pmf* control system for *E. coli* compatible with the BFP interferometry techniques used to monitor motor behaviour. Three main steps were involved in the creation of this system. Firstly, the wild-type *E. coli* strain RP437, and its derivative RP5232, were modified to allow them to be used in motor bead assays without the need for expression vectors. Secondly, the expression of the light-driven proton pump pR was optimised to minimise adverse effects on motor speed. Thirdly, a BFP interferometry setup was modified to provide sufficient illumination for proton-pumping in pR-expressing *E. coli*.

Two model strains of *E. coli*, MT02 and MT03, were constructed and shown to function similarly to previously used *E. coli* test strains. Strains MT02 and MT03 were designed to preserve as many wild-type characteristics as possible whilst remaining usable for bead and tethered-cell assays. All motor components are expressed from the bacterial chromosome and remain unchanged from the parental strains. This allows any plasmid (such as the pR-expression vector) to be introduced without the problem of vector incompatibility. Additionally, strains MT02 and MT03 are also useful base strains for additional modifications such as fluorescently-tagged motor components, as increased tethering ability greatly improves experimental efficiency.

pR was expressed from two different expression vectors, pBAD-HisC (ara-inducible) and pQE-60 (IPTG-inducible). "Burst" expression of pR for 1 hour after induction from pBAD-HisC was shown not to interfere with motor function – motor speed was identical (within experimental error) in cells expressing pR compared to that of motors in unmodified cells.

The light-powering capabilities of pR were also shown to generate a *pmf* sufficient to drive a flagellar motor at similar speeds to wild-type cells, merely by illuminating cell bodies with light of the appropriate wavelength. This is an indication that pR is capable of completely replacing the native respiratory apparatus as a *pmf* source for flagellar motor studies. and allows pR to be used as an alternative source of

pmf for *in vivo* bioenergetic experiments. Importantly, pR-based *pmf* generation was shown to be compatible with laser-based BFP interferometry, allowing accurate measurements of motor speed and angle to be taken.

In the next two chapters, the effects of rapid and varied *pmf* changes on the motor are investigated using the pR-based *pmf* generation system.

Chapter 4

Motor Control with pR

4.1 Aims

The results of Chapter 3 showed that pR, when expressed in *E. coli*, was capable of maintaining a *pmf* which could drive the flagellar motor at similar rates to the native respiratory apparatus. Furthermore, this technique could be combined with the BFP interferometry techniques used to measure motor behaviour. This chapter describes the characterisation of the effects of pR-based *pmf* generation on flagellar motor behaviour.

4.2 Effects of Light-Powering *E. coli* Cells

Section 3.3.2 showed that motors powered exclusively by pR-based *pmf* generation spun at similar speeds to cells powered only by the native electron transport chain. To identify whether pR, as an independent source of *pmf*, could also act in conjunction with the native system – to examine this effect, motor response to pR-based *pmf* generation in "healthy" cells; that is,cells with their respiratory apparatus left intact, was examined.

Cells of *E. coli* strains MT02 transformed with pBAD-pR were grown for motility studies at 30 °C with shaking in TB. pR expression was induced by addition of L-arabinose to 1 mM and all-trans retinal to 10 μM when cells reached OD_{600} 0.4. After this time, cells were harvested and prepared for a standard *E. coli* bead assay using 1 μm polystyrene beads. Since motor response to an added *pmf* source *in vivo* was the subject of investigation, cells were *not* treated with sodium azide before observation.

The average motor speed over 1 minute was measured for 50 cells of *E. coli* strain MT02 expressing pR and illuminated with 100 W m^{-2} 532 nm light as described in Section 3.3.2. Speed was calculated using the power-spectrum method described in Section 2.4.2 with a window time of 1 second. Average motor speed in illuminated MT02-pR untreated with azide was measured to be 43 ± 7 Hz. This is notably faster than the average speed measured for wild-type MT02, which was measured to be 32 ± 5 Hz. A graph of mean cell speeds can be seen in Figure 4.1. Such a marked speed increase in illuminated cells is an unexpected result, as Walter *et al* did not observe such a speed increase in their observations of tethered RP437-pR cells when illuminated [161].

To further examine this speed increase, and to confirm that it was the effect of pR activity, the speed of individual cells of strain MT02 was measured in response to

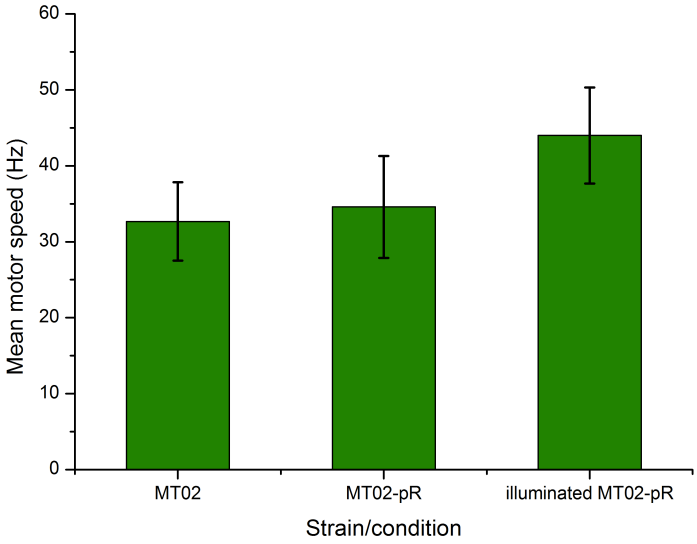


Figure 4.1: Increased motor speed after illumination in mid-log phase pR-expressing cells. A graph of mean motor speeds in MT02 under three conditions: unmodified MT02, MT02-pR and MT02 illuminated with 100 W m^{-2} 532 nm light. Motor speed was measured over 1 minute by BFP interferometry using the power-spectrum technique described in Section 2.4.3. Error bars are the standard deviation from the mean.

single-step changes in illumination with 532 nm light. pR-expressing cells were set up for a bead assay as before, and motor speed was measured using the power-spectrum method (described in Section 2.4.3) in individual cells as they were periodically exposed to 532 nm light. Illumination time was varied from 5-60 s.

In all cells observed, motor speed increased sharply after the start of illumination. Motors remained stable at the higher speeds during the experimental timeframe. After illumination was stopped, speed in motors measured decreased sharply to their initial value (i.e. the speed before illumination). An example trace of a motor subjected to several of these illumination events can be seen in Figure 4.2.

Since the time interval for the observed speed increase was too small to be visible in speed-time traces calculated from power spectra, motor angle over time during a speedup and slowdown event was calculated for the trace shown. This gave an angle/time resolution of 0.5 ms (from a BFP interferometry sampling rate of 2000 Hz). Angle/time traces of a speedup and slowdown event can be seen in Figures 4.3 and 4.4. No intermediate speed levels or gradual speed increases were seen at this resolution; instead, the speed increase occured on a time scale too short to be observed using this technique. There appeared, however, to be a short delay of 4 ms between start of illumination and the effect on the motor. This delay is due to the speed of operation of the shutter in the 532 nm laser path, which introduced a

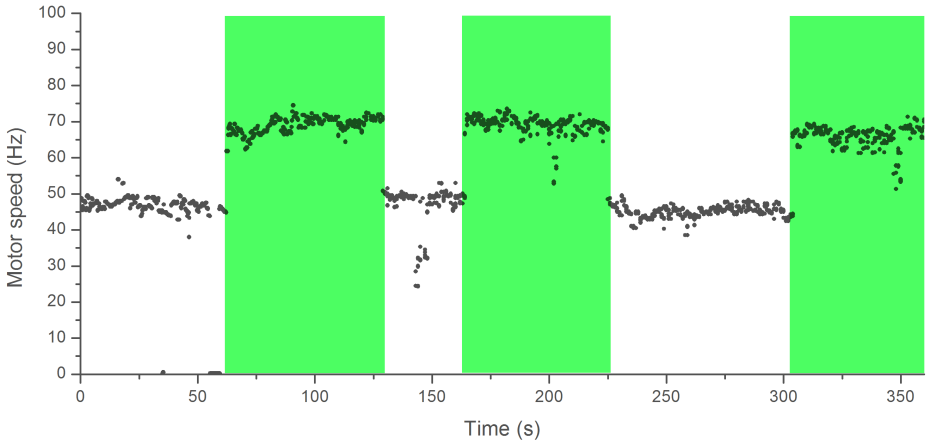


Figure 4.2: A speed-time trace of a motor from a pR-expressing MT02 cell. Motor speed was measured by BFP interferometry using the power-spectrum method described in Section 2.4.3. Green overlay shows the periods where the cell was illuminated with 100 W m^{-2} 532 nm light.

consistent 4 ms delay (see Figure 2.5).

These speed increases after illumination appear to be of a different type to the discrete speed increases observed during resurrection experiments with stopped motors. Typical speed increase was around 15 Hz, which is not a multiple of a typical speed increase due to stator binding (6-7 Hz) [125]. In resurrection experiments, speed increases in discrete increments as stator units begin to generate torque; in this experiment, motor speed increased in a single large step in a sub-millisecond timescale. The absence of any discrete increments suggests that this speed increase is not due to the binding of extra stators, but rather a response to a rapid increase in the *pmf*, specifically the electrical potential difference, across the bacterial membrane.

4.3 Effects of Different Illumination Levels on the Motor

One of the advantages of experiments using chimeric Na^+-driven motors to investigate motor function is the ability to set *imf* to an "intermediate" value between physiological and zero *smf* simply by varying the sodium concentration of the external buffer. It was thought that by changing illumination levels, an analogous effect could be produced in *E. coli*, with lowered light intensity resulting in lowered *pmf* generation. To test this, the effect of changes in light level on *E. coli* motors in

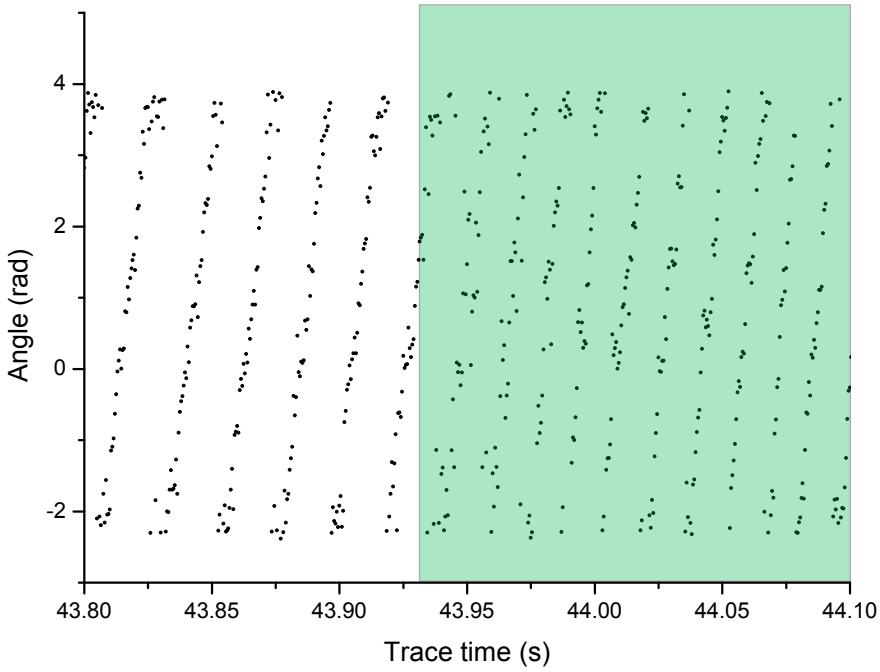


Figure 4.3: A graph of motor angle over time for a speed increase event in the trace seen in Figure 4.2, showing lack of intermediate steps in motor speed up on a millisecond timescale. Motor angle/time was calculated using the method described in Section 2.4.3. Green overlay shows periods of illumination.

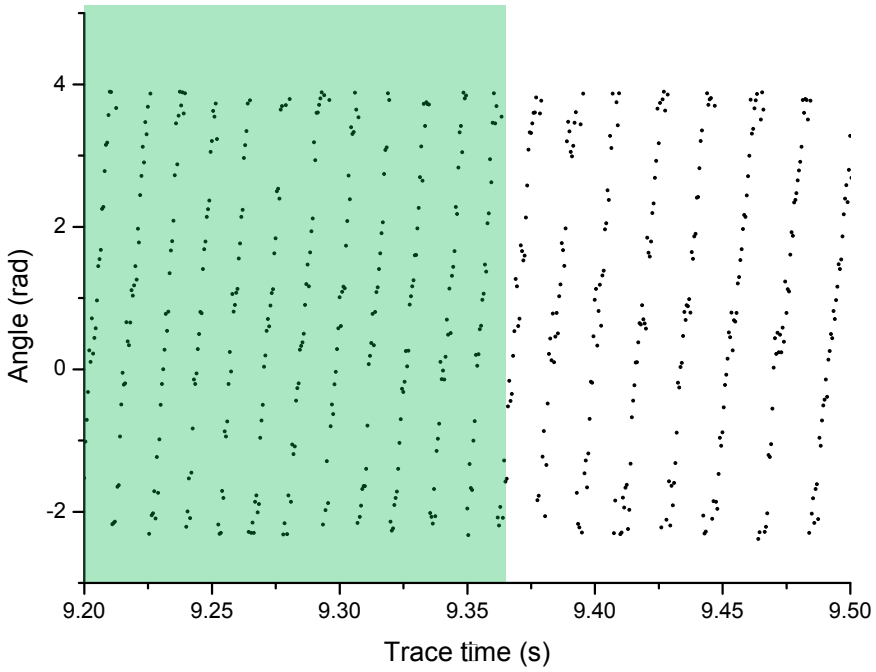


Figure 4.4: A graph of motor angle/time for a slowdown event in the trace shown in Figure 4.2. Motor angle/time was calculated using the method described in Section 2.4.3. The pattern of speed decrease mirrors that of speed increase seen in Figure 4.3. Green overlay shows periods of illumination.

cells powered by pR was investigated. *E. coli* cells of strains MT02 and MT03 were grown for a bead assay as described in Section 3.3.2, and prepared for a bead assay as described in 2.3.2. Motility buffer containing 20 mM sodium azide was flowed through the slide to inhibit native *pmf* generation.

Cells were initially illuminated with 100 W m^{-2} 532 nm light, resulting in motor speeds similar to untreated cells. The level of illumination was then decreased to 50 W m^{-2} by adding an ND filter to the 532 nm laser path. Reduction in light intensity resulted in a corresponding reduction in motor speed in all cells monitored; an example speed/time trace can be seen in Figure 4.5. A typical speed reduction under this regime was ∼10 Hz. All motors monitored were unstable under lowered illumination, with frequent motor stops and fluctuations between several speed levels. Restoration of illumination to its initial level resulted in a speed increase; however, as shown in the example trace, motors did not return to their initial speeds in the experimental timescale.

The cause of motor instability at reduced illumination levels is unclear. One possibility is that lowered *pmf* results in a lowered affinity of stator units for the flagellar motor; the effects of lowered *pmf* on stators is explored further in Chapters 5 and 6.

4.4 Investigating the Stepping Action of the *E. coli* Motor

Previous studies using chimeric Na^+-driven motors in *E. coli* demonstrated that the *E. coli* motor is a stepping motor [145]. By reducing *smf* by buffer exchange and the effects of photodamage, motors were made to rotate sufficiently slowly for individual steps in motor rotation to be seen. 26 steps in rotation were observed, corresponding to the potential stoichiometry of the motor FliG ring (see Section 1.3.5 and 1.4.2). It was thought that a pR-based *pmf* generation system could be used to investigate stepping of wild-type motors, confirming the symmetries in periodicity determined for the Na^+-driven chimera.

Cells of strain MT03 were grown and prepared for a *E. coli* bead assay using the pR-based *pmf* generation as described in Section 3.3.2. Strain MT03 ($\Delta cheY$) was used so that motors would consistently rotate in one direction only. Sodium azide solution was added to inhibit native *pmf* generation. Motors in selected cells were monitored to ensure good trajectory of attached beads and stable motor rotation. Illumination was then lowered to 10 W m^{-2} by adding an ND filter to the 532 nm

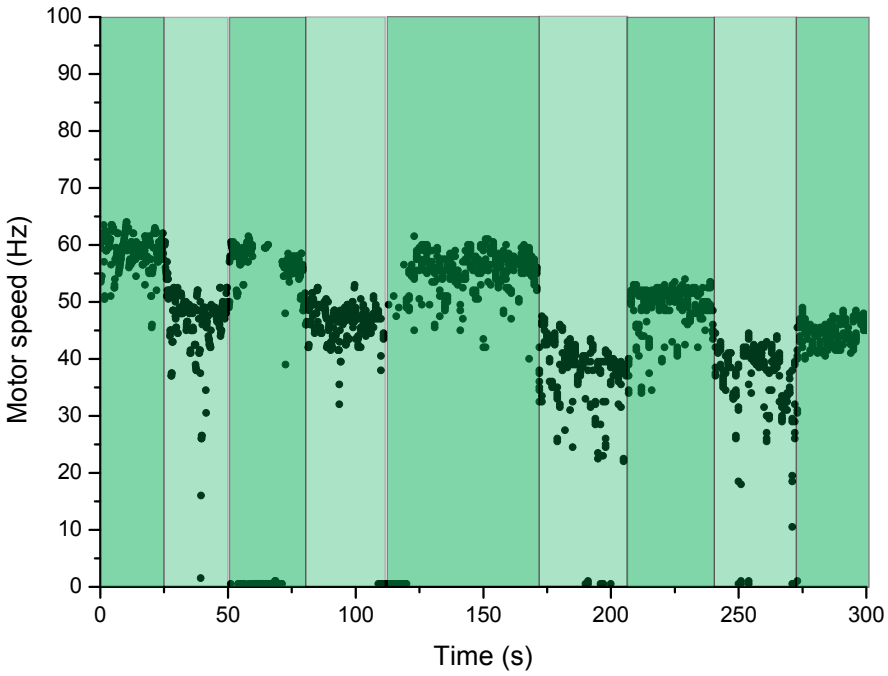


Figure 4.5: The effects of lowered illumination levels on *E. coli* motors powered by pR. A speed/time trace of a motor in a pR-expressing cell of strain MT02. Speed was calculated using the power-spectrum method described in Section 2.4.3. Dark green overlay shows periods where cells were illuminated with 100 W m^{-2} 532 nm light; lighter green where illumination was lowered to 50 W m^{-2}.

laser path. This caused motor speed to fall to around 1 Hz in cells monitored. Motors underwent several stop events at this very low *pmf* generation regime. Motor angle/time was calculated from bead BFP interferometry data as described in Section 2.4.3. A typical angle/time trace of a motor under this low *pmf* regime can be seen in Figure 4.6.

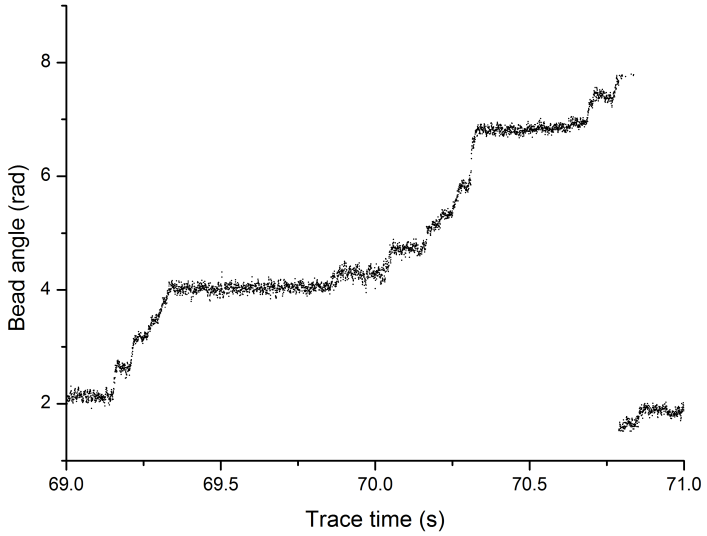


Figure 4.6: An angle/time trace of a cell subjected to a low *pmf* regime by illumination with 10 W m^{-2} 532 nm light. Motors can be seen to dwell at fixed angles between shorter periods of stepwise rotation. Angle/time data was calculated using the method described in Section 2.4.3. Time resolution is 0.5 ms.

The angle-time trace shows the irregular nature of rotation under this regime. Motors rotated for short periods of time, then stopped temporarily at a "dwell" angle before resuming rotation. Motors stopped at several different angles, indicating that motor stops were not an artefact of the measurement method – the laser used to measure bead rotation can optically trap beads attached to slowly rotating motors.

An attempt was made to calculate stepping periodicity with from this collection of stepping angle-time data with Dr Bradley Steel of the Department of Physics, using the step-finding method described in Little *et al* [83]. The aim was to find symmetries in motor rotation which corresponded to the periodicity of different motor components, such as potential stator binding sites or the FliG ring to which stators bind. Collections of angle-time data were used as inputs for an empirical distribution function (ECF)-based step smoothing and symmetry method. However, no clear symmetries corresponding to motor stoichiometries could be observed in any data analysed. The results of the ECF algorithm can be see in Figure 4.7. The cause

of the lack of clear motor symmetries is unclear; one possibility is that the stop-start nature of rotation prevents resolution of short motor steps compared to longer dwell times.

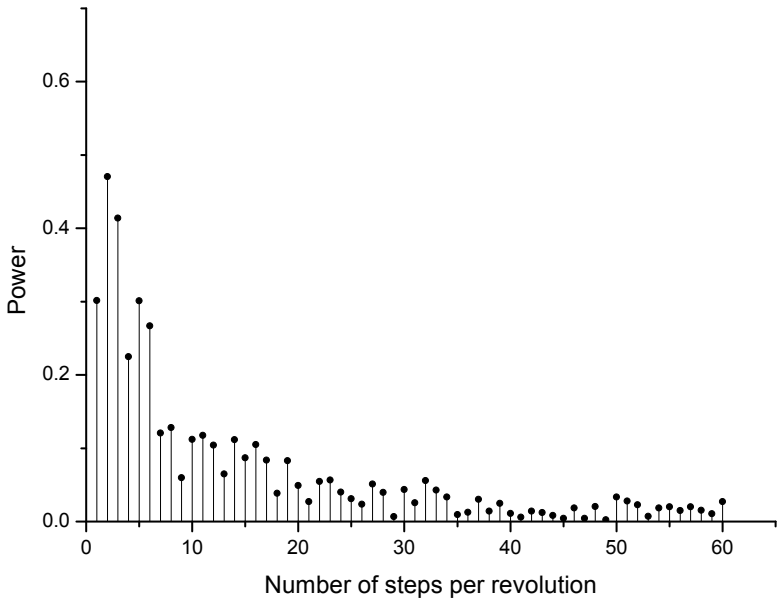


Figure 4.7: The results of analysis of 30 s of data from the trace shown in Figure 4.6 using an ECF-based symmetry finding algorithm. No periodicities corresponding to potential motor symmetries could be observed.

4.5 Discussion

The results in this chapter demonstrate how the wild-type *E. coli* motor responds to rapid *pmf* changes *in vivo*. In the first experiment, the effects of pR-based *pmf* generation on cells which retained native *pmf* generation were observed. Unexpectedly, wild-type *E. coli* motors were found to respond to increased *pmf* with an increase in speed; this directly contradicts the work of Walter *et al* [161], who observed no such effect in tethered RP437. This result represents the first observation of *E. coli* motor rotation powered by a *pmf* higher than the *in vivo* norm.

Motor efficiency is assumed to be almost 100 % efficient at high load and speed, with torque generation tightly coupled to ion transit (an equivalent statement is that stators have a high duty ratio). Increased motor speed in healthy cells under a higher *pmf* regime is therefore more likely to be due to an increased rate of proton translocation through stator units which are already bound to the motor, rather than recruitment of extra stators. Examination of motor angle over time during speedup

events showed that the timescale of motor speed increase upon light powering was < 1 ms, which is orders of magnitude faster than observed stator recruitment rates. The limiting factor for motor speed in the cell under these conditions is unknown. Two possible factors are that either voltage increases past the *E. coli* membrane's dielectric breakdown point, preventing further *pmf* increase, or that speed increase is limited by a rate-limiting step in proton translocation through bound stators. The latter hypothesis may be supported by the observation that Na^+-driven chimeric motors in *E. coli* rotate more quickly at any given *imf* compared to wild-type H^+-driven motors; increased efficiency in ion translocation may enable speed increase in chimeric motors.

By lowering illumination levels, the effects of lowered *pmf* on motor rotation and stability could be observed. Motor speed has been previously shown to be proportional to *imf* in both H^+- and Na^+-driven motors; therefore, the observation that lower light levels results in lowered motor output is unsurprising. Decreased motor stability could be due to an increase in stator turnover or a weakening of the stator-basal body interaction; alternatively, the relative speed reduction after restoration of illumination could be a side-effect of continuous *pmf* manipulation and laser photodamage, lowering the effective capacitance of the plasma membrane.

However, the pR-based *pmf* control system was also shown to be able to cause motors to rotate at sufficiently low rate for individual steps in rotation to be observed. Unfortunately, no symmetries in stepping behaviour could be found. The observation of transient stops during slow rotation is possible evidence of *pmf*-dependent stator disengagement from the motor, however – at the speed levels observed, motors are probably powered by one stator only, with others either disengaged or inactivated. Loss of torque generation from a single stator (either through natural turnover, or a *pmf*-dependent event) would cause the motor to stop at an arbitrary angle.

In the next chapter, Chapter 5, the effects of *pmf* disruption on the flagellar motor are examined using resurrection studies and fine *pmf* control.

Chapter 5

Resurrection Studies of Wild-Type *E. coli* Motors

Abolition of *pmf* causes disengagement in non-functional *E. coli* chimeric motors [47]. However, this phenomenon has not yet been investigated in wild-type *E. coli* motors. Additionally, the timescale for detachment is unknown. Is stator binding absolutely dependent on *pmf*, so that stators detach immediately after *pmf* loss? Or is stator detachment a more gradual process?

The experiment described in Section 4.2 demonstrated that pR-based *pmf* generation could affect the motor on sub-millisecond timescales. The use of pR also allowed for *pmf* to be reduced or removed completely for well-defined periods of time. Using this system, the potential consequences of sequential stator deactivation could be separated from shorter-scale effects of abolition of proton flow through the motor for the first time. In this chapter, the effects of *pmf* abolition on wild-type *E. coli* flagellar motors are investigated *in vivo*.

5.1 The Effects of *pmf* Loss on the Flagellar Motor

5.1.1 Characterising The Effects of *pmf* Loss on the Motor

Before the effects of *pmf* loss could be investigated, care had to be taken to ensure that all other sources of *pmf* in the cell were completely inhibited. Although azide effectively inhibits both the *E. coli* electron transport synthase and ATP synthase, this process is not immediate. Any effects of residual endogenous *pmf* generation would be noticeable in motors from cells shortly after their exposure to azide.

Cells of strain MT02 were grown and prepared for a standard pR-expressing bead assay as detailed in Section 3.3.2. Tunnel slides containing bound cells were treated with 20mM sodium azide solution before analysis; turnaround from addition of azide to the start of illumination was typically 20 s. Cells were illuminated with 100 W m^{-2} 532 nm light immediately after the tunnel slide was placed on the cell for analysis. Illumination was stopped by activation of the motorised shutter in the 532 nm laser path. Motor slowdown after illumination stop was monitored for two populations of cells: a) 27 cells where illumination was stopped less than 1 minute after addition of azide, and b) 24 illuminated cells which had been exposed to azide (while being illuminated to maintain *pmf*) for more than 15 minutes. Motor speed was measured using the angle/time method described in Section 2.4.3. A speed/time trace of each event can be seen in Figures 5.1 and 5.2.

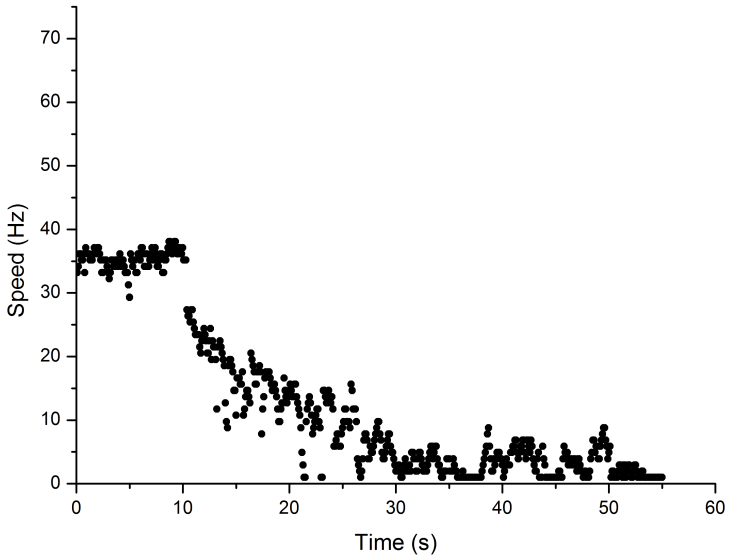


Figure 5.1: A speed/time trace of a motor slowdown event from a cell shortly after addition of azide. Motor speed was calculated using the power spectrum method. This cell took 55 seconds to reach a complete stop.

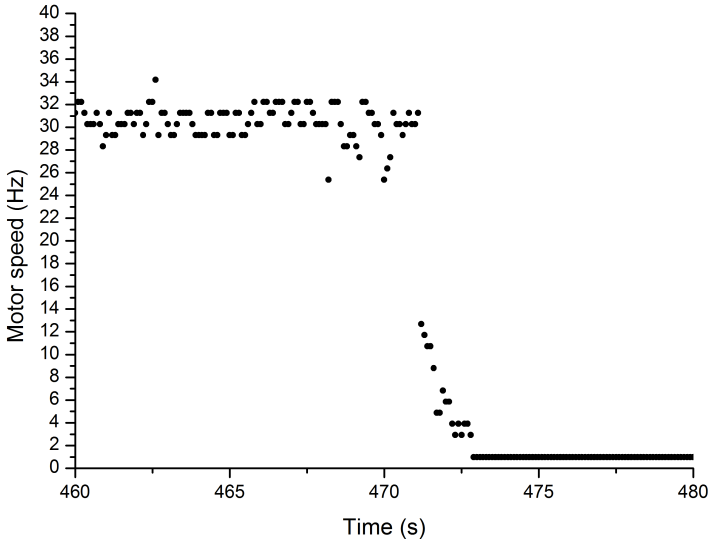


Figure 5.2: A speed/time trace of motor slowdown after an extended period of illumination, where pR was the only source of *pmf*. Note the rapid reduction in speed compared to the trace in Figure 5.1.1. Motor speed was calculated using the power-spectrum method, as described in Section 2.4.3.

To test for consistency in slowdown events, several measurements of motor speed decrease after loss of illumination were taken for the two populations. Since motor speed varied between individual cells, each slowdown event was normalised so that initial speed was set to "1" in all cases. The collection of normalised speeds for each slowdown event in each population were then averaged and plotted, resulting in graphs showing an average of many slowdowns from nominal speed "1" to a complete stop. Graphs of normalised mean speeds over time for cells which spent < 1 minute and > 15 minutes in azide can be seen in Figures 5.1.1 and 5.1.1. A collection of the individual speed/time traces can be seen in Appendix C.

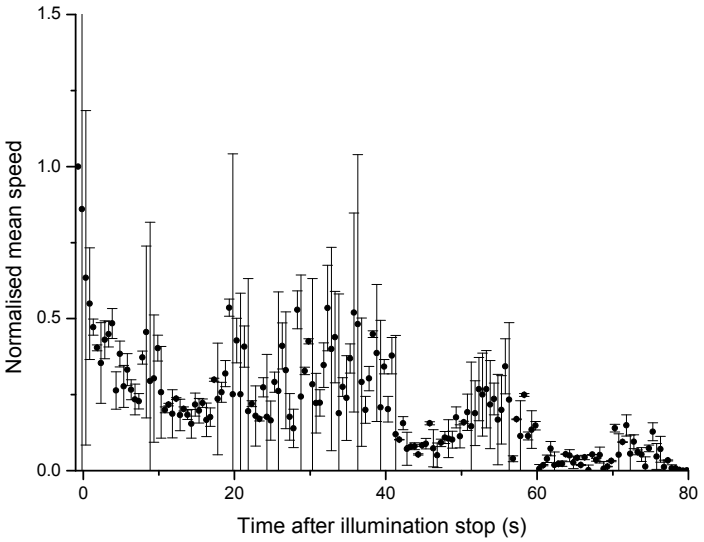


Figure 5.3: A normalised mean speed/time trace showing the average motor slowdown in 27 cells which had spent < 1 minute being illuminated after addition of azide. Motor speed was calculated using the angle-time method described in Section 2.4.3, and each individual trace making the average was normalised to the initial motor speed. Error bars show the standard deviation from the mean.

A marked difference in the nature of motor slowdown between the two populations was observed. Motors in cells which had been exposed to azide for a short period of time take a much longer time to reach zero speed compared cells exposed to azide for longer periods. Additionally, motor slowdown is much "noisier", with large speed variations as motors slow to a stop. The much longer time taken for motors to stop in cells shortly after poisoning is probably due to residual endogenous *pmf* generation by incompletely inhibited respiratory chains or ATP synthase. Such an effect would also account for the large variance in speeds observed during slowdown events.

Motors in cells subjected to extended periods of light-powering displayed a rapid

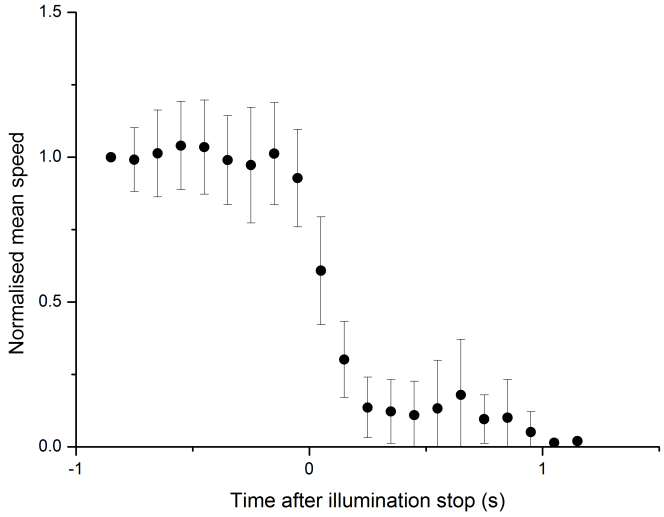


Figure 5.4: Normalised mean speed/time traces showing the average motor slowdown in 24 cells which had been illuminated for > 15 minutes after addition of azide . Motor speed was calculated using the angle-time method described in 2.4.3, and each individual trace making the average was normalised to the initial motor speed. Error bars show the standard deviation from the mean.

reduction in motor speed after illumination stop. This speed reduction appears to be in two stages. Illumination stop first causes a rapid drop (t < 0.1 s) in motor speed to ∼20 % of its initial value. This is followed by a more gradual reduction in speed, with motors reaching a complete stop within 1 s on average.

5.1.2 Time at Zero *pmf*: Effects on the Motor

Using the ability to rapidly lower *pmf* by stopping illumination, the behaviour of motors during transient *pmf* reductions was investigated. Cells of strain MT02 were grown and prepared for a standard pR-expressing bead assay as described in Section 3.3.2. Cells were light-powered for 15 minutes after addition of azide to ensure loss of endogenous *pmf* generation. Cells were then subjected to repeated stops in illumination of brief duration (time without light <1 s).

Motors responded to transient periods without illumination with a corresponding rapid reduction in motor speed. Restoration of illumination caused motors to rapidly return to their initial speeds. An example speed-time trace of a motor from a cell subjected to several of these transient illumination stops can be seen in Figure 5.5.

Speed-time traces for 28 of these events were calculated using the angle-time

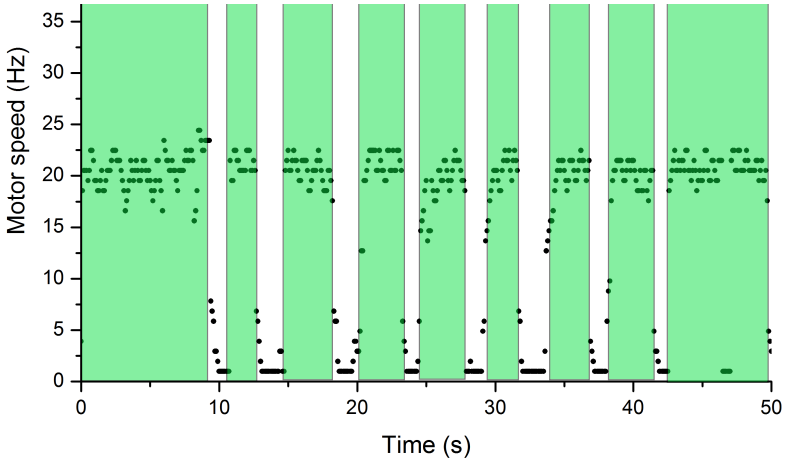


Figure 5.5: A speed/time trace of an *E. coli* motor subjected to repeated short transient *pmf* disruption events (time without light < 1 s) by rapid stops in illumination. Speed was calculated using the power spectrum method described in Section 2.4.3. Green overlay shows periods where cells were illuminated with 100 W m^{-2} 532 nm light.

method described in Section 2.4.3. The speed-time traces were then normalised to the motor speed before illumination stop (so that the speed before *pmf* disruption was set to "1") as before. The normalised traces were then averaged and plotted, giving the graph shown in Figure 5.6. Individual speed/time traces can be seen in Appendix C.

Motor speed did not reduce to zero in the experimental timescale for transient *pmf* disruption. This is consistent with the observation in Section 5.1.1, where motors took ∼1 s on average to reach a complete stop. To investigate motor behaviour more closely during motor slowdown and recovery, bead angle over time was calculated during a transient *pmf* disruption, providing a time resolution of 0.5 ms. A graph of bead angle over time can be seen in Figure 5.7.

The angle-time trace shown in Figure 5.7 shows that motor slowdown and recovery during transient *pmf* disruption events is a two-stage process, similar to the effects seen after *pmf* generation more generally (see Figure 5.1.1). After a short lag time (attributable to the time taken for the shutter controlling the 532 nm laser to shut completely), motor speed fell quickly (within 5 ms) to a small proportion of its initial speed, without stopping completely. Motor rotation appears to be unstable under the low-*pmf* regime, but without the dwelling at arbitrary angles observed at ultra-low *pmf* (see Section 4.4). Restoration of illumination caused a rapid (within 5 ms) restoration of motor speed to its initial value. No intermediate steps were observed during speed restoration; therefore, the speed increase is unlikely to be

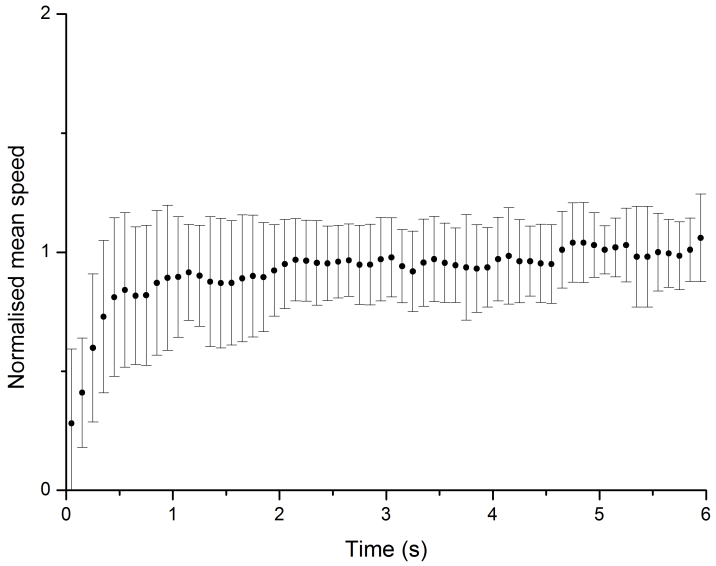


Figure 5.6: A graph showing the normalised average of the time taken for motors to return to initial speed after 28 short *pmf* disruption events in 7 cells *E. coli* strain MT02. Error bars show the standard deviation from the mean.

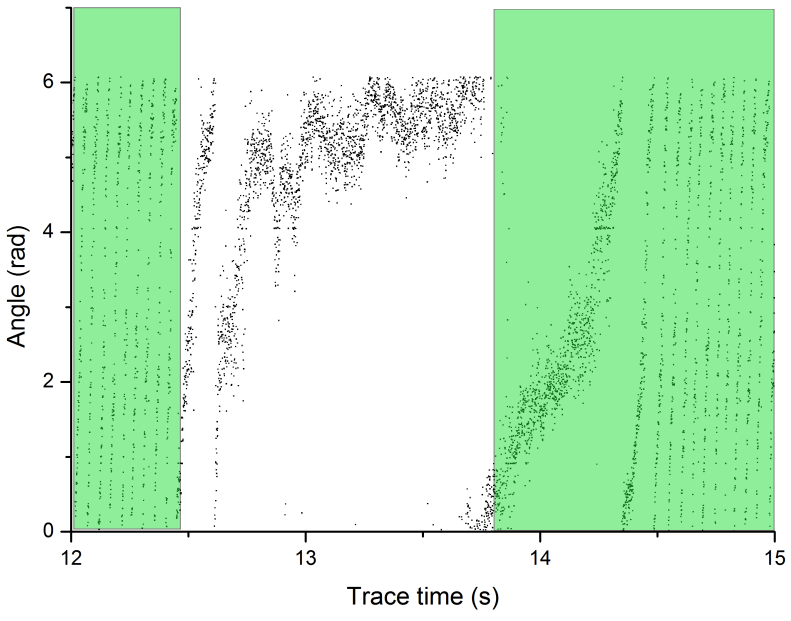


Figure 5.7: An angle/time trace of a bead attached to a motor during a transient *pmf* disruption event (the event seen at time point 12 s in Figure 5.5). Green overlay shows period where the cell was illuminated with 532 nm light. The bead can be seen to rotate at a much lower rate during illumination stop.

caused by re-activation of discrete stator units, but rather, a restoration of an electric potential across the *E. coli* inner membrane.

5.2 Motor Resurrection in De-Energised *E. coli*

In this experiment, "resurrection" of a wild-type motor after extended periods of *pmf* loss *in vivo* was examined, rather than the shorter periods investigated previously. Cells of strain MT03 transformed with pBAD-pR were grown for an *E. coli* bead assay as described in Section 3.3.2. Strain MT03 was used to minimise the effects of switching on speed analysis. Cells were prepared for am *E. coli* bead assay as described in Section 2.3.2 and treated with sodium azide solution to inhibit native *pmf* generation. Those cells in the zone of illumination maintained a *pmf* (as shown by continued motor rotation), while those outside gradually slowed down to a complete stop.

Once the motors of cells outside the zone of illumination had completely stopped (indicating complete loss endogenous *pmf* generation in those cells), illumination was stopped by closing the electromechanical shutter in the 532 nm laser path (see Figure 2.5). Stopping illumination caused cells to slow down to a complete stop due to loss of *pmf*. After rotation had ceased entirely, cells were left at a complete stop for a long period of time (over 2 minutes). Illumination was then restored, allowing pR to re-establish a *pmf* across the membrane.

Figure 5.2 shows an example trace of a cell of strain MT03. While under illumination this flagellar motor maintained a consistent speed of 42 Hz. After illumination was stopped, motor speed gradually reduced, reaching 0 Hz after $\sim$ 60 s. The motor was then left at a complete stop for 40 s. After this time, illumination was restored, and after a delay of $\sim$5 s, the motor began to rotate again. A new maximum speed of 32 Hz was reached after $\sim$3 minutes. The motor did not return to its initial speed in the experimental timeframe.

The speed/trace shown in Figure 5.2 shows a stepwise resurrection pattern, with speed increasing from a complete motor stop in discrete increments. Five clear jumps in motor speed can be easily observed, with the first step being roughly twice the size of the others. This is consistent with previous resurrection studies where *imf* was disrupted: chimeric motors expressed in *E. coli* show this characteristic resurrection pattern after disruption of *smf* [145] as do *E. coli* motors powered by an external voltage source [48].

To further investigate the nature of these steps, the mean difference between

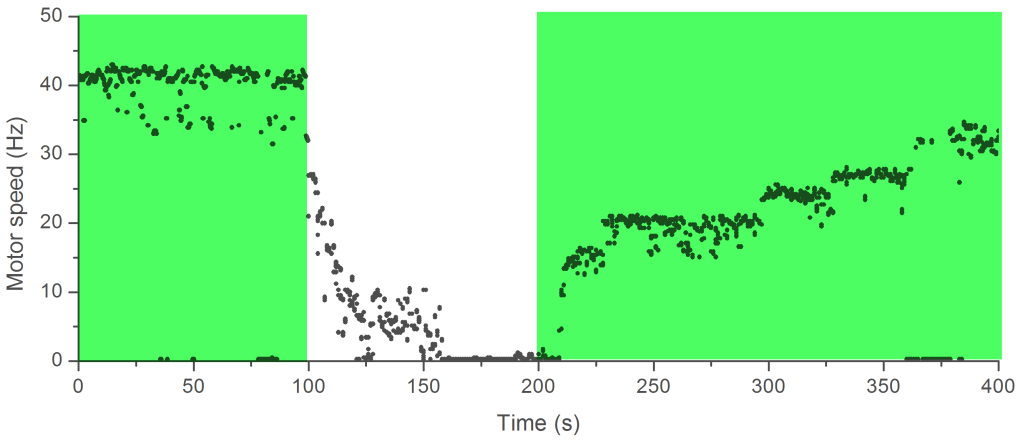


Figure 5.8: A speed/time trace of a resurrection of a *E. coli* cell powered by pR-based *pmf* generation, strain MT03. Motor speed was measured by monitoring position change of a 1 μm polystyrene bead attached to a flagellar stub. The cell was treated with 20 mM sodium azide solution to inhibit native respiratory electron transport chain; *pmf* was generated by pR through illumination with 532 nm light. The green overlay shows periods where the cell was illuminated.

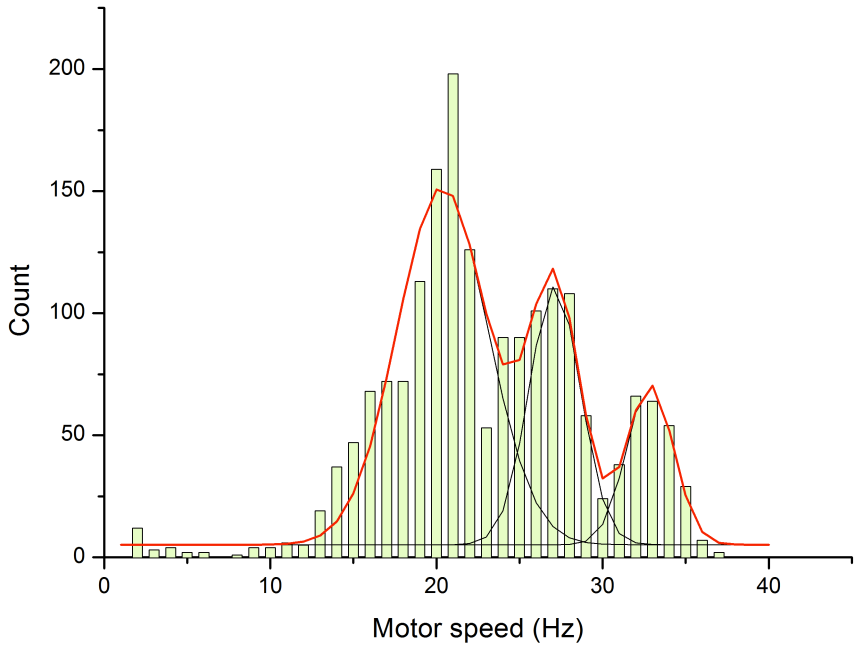


Figure 5.9: A histogram of 1 second speed windows taken from the trace seen in Figure 5.2. 1 Hz bins were used. The large peaks seen correspond to the long motor dwell times observed at speed levels 2, 3 and 4. Black lines show Gaussian curves fit to the histogram; the red line is a summation of the curves. Distance between the three peaks is 6.3 $\pm$ 0.5 Hz.

the steps in motor speed was calculated. Average motor speeds using a 1 s rolling average were calculated for the trace seen in Figure 5.2. The list of mean speeds from this trace was then sorted into a histogram using 1 Hz bins (the maximum speed resolution). A plot of this histogram can be seen in Figure 5.9. The three clear observable peaks on the histogram correspond to the intermediate speed levels 2, 3 and 4 observable on the speed/time trace. Peaks corresponding to other speed levels are not distinguishable on the histogram due to the shorter dwell times at these speeds.

Multiple Gaussian curves were fitted to the histogram peaks, using the OriginPro graphing software (Origin). By measuring the distance between the peaks of the Gaussian curves, the mean step size between speed levels 3, 4 and 5 during resurrection was calculated to be 6.3 ± 0.5 Hz. This figure corresponds well to the contribution of individual wild-type *E. coli* stator units to motor speed under 1-μm load regimes, which was previously calculated to be 6.9 ± 0.4 Hz by Reid *et al* [125]. Observation of individual speed increases of these size are therefore strong evidence of sequential stator activation in the *E. coli* motor after extended periods at zero *pmf*.

To compare the time taken for recovery of motor speed in cells de-energised for long periods of time and cells subjected to transient *pmf* disruption,"de-energised" cells were defined as those whose motors had stopped for at least 20 s. Only traces where motor speed reached its initial value during the experimental timeframe were used, to allow comparisons of "complete" motor resurrections for the two populations. 37 resurrection events in de-energised cells were measured, and speed/time traces for the resurrections were calculated using the bead angle-time method. Traces were normalised to the initial motor speed before de-energisation and averaged. A graph of the normalised average speed-time trace is shown in Figure 5.10.

The mean time for complete motor speed recovery after extended time in the dark was ∼60 s, with a large degree of variance in intermediate speeds (as indicated by the error bars in Figure 5.10.). This variance is due to differing responses to similar *pmf* loss between different traces; although stepwise recovery was observed in many cases, the dwell time at intermediate speed levels was different for each motor. However, recovery time is consistently longer in motors after extended time at zero *pmf*, compared to recovery time for motors after transient *pmf* reductions.

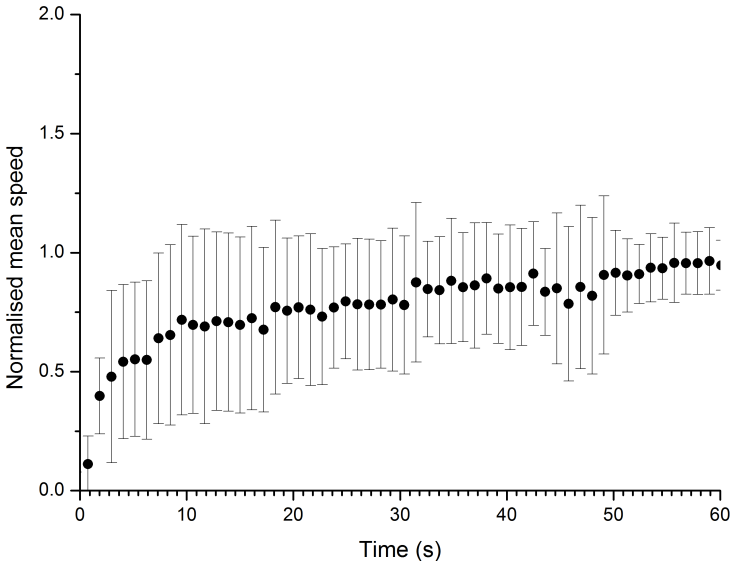


Figure 5.10: A graph showing the normalised average of 37 resurrection events from motors in cells subjected to extended times (> 20 s) at zero *pmf*. Note the time for motor recovery compared to Figure 5.6; motors take 1 minute on average to reach their initial speed, rather than 2-3 s. Error bars show the standard deviation from the mean.

5.3 DISCUSSION

This chapter shows that motor resurrection after extended disruption of *pmf* is stepwise, with motor speed increasing in discrete increments after *pmf* restoration. The size of these steps is consistent with the previously calculated value for the contribution of individual stator units at this load. This study represents the first observation of such steps in wild-type motors with stators expressed at wild-type levels *in vivo*, and further confirms the hypothesis that stator interaction in the motor is dependent on *pmf*.

Interestingly, after stepwise resurrection, motors did not always return to their previous speeds after stepwise resurrection, but instead settled at a lower stable speed. This speed difference cannot be ascribed to a difference in *pmf*, as illumination levels were the same before and after resurrection. Instead, the limiting factor for motor speed under these conditions may be the organisation of stators bound to the basal body. Steric hindrance between bound stator units may result in fewer free sites for subsequent stators. One consequence of steric hindrance would be that although 11 wild-type stators can fit around the motor basal body, fewer than this would be bound on average to a wild-type motor at physiological *pmf* after resurrection. As stators are constantly dissociating and re-associating with the motor,

fitting the maximum number of stators to the motor may not be possible even under "ideal" conditions.

Comparison of recovery time for motors subject to short and long periods of time at a zero *pmf* regime gave an approximate timescale for stator unbinding from the motor. Stators do not leave the motor immediately after loss of *pmf*, as stepwise motor recovery is not observed after transient *pmf* disruptions. The effects of stator behaviour on motor output are therefore apparent on a timescale of seconds, rather than milliseconds. Stators remain bound to the motor for a time after *pmf* loss, with extended periods at zero *pmf* resulting in complete disengagement.

A surprising finding was the observation of two distinct stages in speed reduction after stopping illumination in cells powered by pR. Motor speed first drops to around 20 % of the initial speed on a millisecond timescale (as can be observed in Figure 5.7), then decreases more slowly. What is the cause of this? The lack of observable steps (however short) during motor recovery suggests that this effect is not due to any reversible change in conformation of stators bound to the motor. Instead, it is more likely to be a consequence of *pmf* dynamics across the plasma membrane. Motors are capable of making use of both the ΔpH and membrane voltage components of the *pmf*, and motor speed is proportional to *pmf* at the loads used in this experiment [90]. Since the capacitance of the *E. coli* inner membrane is relatively low (0.7 μF cm^{-2}) [8], any voltage across the membrane would collapse quickly after illumination stop. This voltage collapse would cause motors to rapidly drop to a speed proportional to the strength of the remaining *pmf* generated by the ΔpH gradient only. Using the Nernst equation (see Section 1.6.1), the contribution of the pH gradient to the overall *pmf* can be calculated. Assuming a *pmf* of -150 mV and a difference between the periplasm and cytoplasm of -0.6 $(7.0 - 7.6)$, the *pmf* generated by the pH gradient only is ~ -35 mV, 24 % of the total *pmf*. This figure agrees well with the speed drop observed immediately after illumination stop. Future work could confirm this by abolishing the pH gradient in light powered cells with an antibiotic such as nigericin. Under these conditions, pR-powered cells would reach a stop immediately after illumination stop.

The results in this chapter provided strong indirect evidence for the hypothesis that wild-type motor integrity is dependent on the *pmf in vivo*. In the next chapter, fluorescence microscopy techniques are used to investigate motor integrity and *pmf* directly.

Chapter 6

Visualising Motor Integrity

6.1 Aims

The work described in Chapter 5 provided a strong indication that stator units underwent reversible inactivation process after *pmf* disruption *in vivo*. This deactivation could take several forms: stators could change confirmation with respect to the switch complex or basal body, or could physically disengage from the flagellar motor with falling *pmf*. Previously, work using fluorescently-tagged MotB proteins in functioning stators [79], demonstrated turnover of stator units at physiological *pmf*. Stators could be seen to physically leave and re-enter functioning flagellar motors, exchanging with a membrane "pool" of unattached stators. Other motor components have also been shown to display a degree of turnover; studies with fluorescently-tagged FliM showed the presence of two populations of FliM in the motor switch complex; one which underwent turnover and one which did not [36].

The ability to image fluorescently-tagged stator units allows stator dynamics at varying *pmf* levels to be observed directly. If stators do indeed physically disengage with the motor under a zero *pmf* regime, motor "spots" of fluorescently-tagged stators bound to rotating motors might be seen to disperse and reform as *pmf* is disrupted and restored.

In this chapter, the dependence of *E. coli* motor integrity on *pmf* is tested by monitoring the behaviour of fluorescently-tagged motor components at differing *pmf* levels. Additionally, an attempt to create a novel GFP-MotA fusion is described, in an effort to enable a range of new experiments into motor component stoichiometry and co-localisation.

6.2 Strain Construction

Expression of tagged motor proteins from the genome presents several advantages compared to over-expression from plasmids. This method ensures that introduced genes are expressed at wild-type levels, as expression is controlled by native promoters, and that genes are co-transcribed and translated with others encoded on the same operon. Since expression levels are the same as wild-type, examination of protein dynamics and copy numbers gives an accurate representation of motor behaviour.

Tagging individual components of large protein complexes such as the flagellar motor is difficult, as insertion of a fluorophore can disrupt the delicate and intricate interactions between components required for correct function. Several functioning

fluorescently-tagged motor protein fusions have been created, such as GFP-MotB [25] and YPet-FliM [35]. However, no functioning fusion has been created for the stator protein MotA. Neither N-terminal nor C-terminal GFP-MotA fusions display a motile phenotype, although the C-terminal fusion is fluorescent and localises to the flagellar motor. Construction of a functioning GFP-MotA fusion would be useful for several reasons. MotA copy number in the motor is twice that of MotB, due to the stoichiometry of the stator unit (MotA4:MotB2); the corresponding increase in brightness would increase the signal to noise ratio of motor stoichiometry experiments. MotA-GFP fusions could also act as FRET donors or acceptors for experiments into co-localisation of motor components. Finally, the integrity of the stator unit during stator turnover could be investigated in more detail.

6.2.1 Construction and Testing of Strains MT04 and MT05

The previously-made strains JHC1 (*gfp-motB*) and JPA945 (*yPet-fliM*) were adapted for efficient tethered cell and bead analysis by chromosomal replacement of the wild-type flagellin gene *fliC* with *fliC*st, which produces "sticky" flagellar filaments when expressed. Chromosomal replacement was carried out by plasmid pDS-*fliC*st, using the protocol described in Section 3.2.2. Correct replacement of *fliC* with *fliC*st was confirmed by Southern blotting and DNA sequencing. The resulting strains, MT04 (*gfp-motB*, *fliC*st) and MT05(*fliM-yPet*, *fliC*st) were frozen and stored at -80 °C.

Motility of MT04 and MT05

The addition of fluorescent protein tags to MotB and FliG has been shown to reduce cell motility. GFP-MotB expressing strains retain 25 % swarming ability compared to wild-type RP437, while the YPet-FliM expressing strain JPA945 retains 80 % of wild-type swarming ability. Since FliCst-expressing cells do not swarm on soft agar (see Section 3.2.3), a beaded-cell assay was used to test motor function in these strains.

Cells of strains MT04 and MT05 were grown and prepared for an *E. coli* bead assay as described in 2.3.2. Motor speed in 15 cells of MT04 and MT05 was measured over 1 minute using BFP interferometry (described in Section 2.4.2). Both MT04 and MT05 were shown to be motile, but with some impairment in speed compared to the wild-type motor. Mean motor speed in MT04 was 13.2± 6.8 Hz (37 % of wild-type), while mean motor speed in MT05 was 24.3 ± Hz (68 % of wild-type). These speeds are comparable to the motility impairment seen in swarm plate assays

of the parent strains JHC1 and JPA945 [25] [35].

Fluorescence Microscopy of MT04 and MT05

The fluorescence ability of strains MT04 and MT05 was verified using TIRF microscopy. Cells were prepared for imaging as follows: single colonies of each strain were picked and grown aerobically with shaking overnight in LB at 37 °C. The next morning, 100 μl of overnight culture of each strain was subcultured into 5 ml TB, and grown to OD_{600} 0.6 at 30 °C. 1 ml of each culture was then centrifuged and resuspended in an equal volume of motility buffer. Flagella in suspended cells were sheared as described in Section 2.3.2). The sheared cell suspension was centrifuged and resuspended in 200 μl motility buffer. 50 μl of sheared cell suspension was then passed through a tunnel slide and incubated for 15 minutes, allowing cells to tether by their flagella, before being flushed with 200 μl motility buffer.

Bright-field imaging of tunnel slides of MT04 and MT05 showed many rotating cells which were tethered to the coverslip by their flagellar filaments. TIRF microscopy was then used to image expressed fluorophores in each strain. A home-built TIRF microscope was used in this and all further experiments (described in Section 2.4.1. Excitation wavelengths for GFP (expressed in MT04) and YPet(expressed in MT05) were 488 and 532 nm respectively. Both MT04 and MT05 showed similar fluorescence to their parent strains JHC1 and JPA945, with characteristic motor "spots" of concentrated fluorophores observed at the centre of rotation. False-colour TIRF images of each strain can be seen in Figure 6.1.

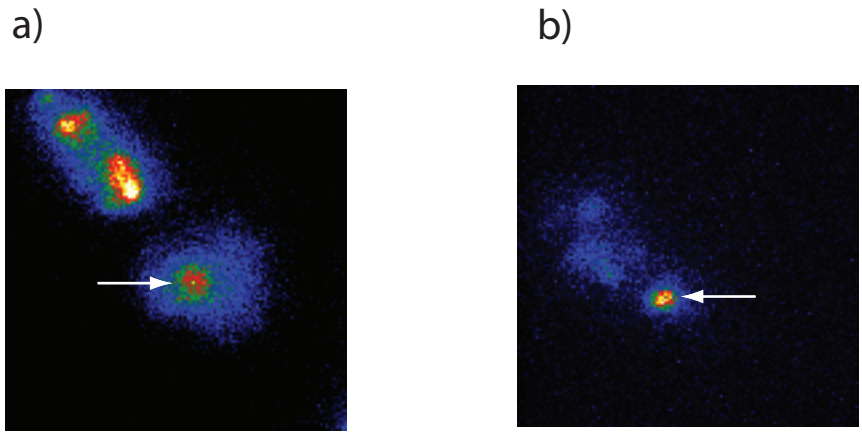


Figure 6.1: TIRF images of cells of (a)MT04 and (b)MT05, showing concentration of fluorophores in motor "spots" around the centre of rotation (as shown by the arrows).

6.2.2 Construction and Testing of Strain MT06

Construction of MT06

As N- and C-terminal GFP-MotA fusions were both shown to be non-functional, a new tagging approach was attempted: the creation of an "in-loop" GFP-MotA fusion. In this method of tagging, the gene for a fluorescent protein is inserted into the middle of the gene encoding the target protein. Expression of the resulting mutant gene results in a single long polypeptide, with GFP independently folding into an extra domain in the protein. Creation of such fusions has proven to be a successful technique for tagging membrane proteins such as the "Shaker" voltage-gated ion channel [139], where addition of N- or C-terminal tags would disrupt correct protein folding and function.

MotA contains a single cytoplasmic loop between residues 45 and 178 (see Figure 6.2) which connects transmembrane helices TM1 and TM2. This loop contains the functionally important residues Arg90 and Glu98, which interact with charged residue on FliG and are vital for torque generation. Insertion of GFP would necessarily need to avoid disruption of this MotA-FliG interface.

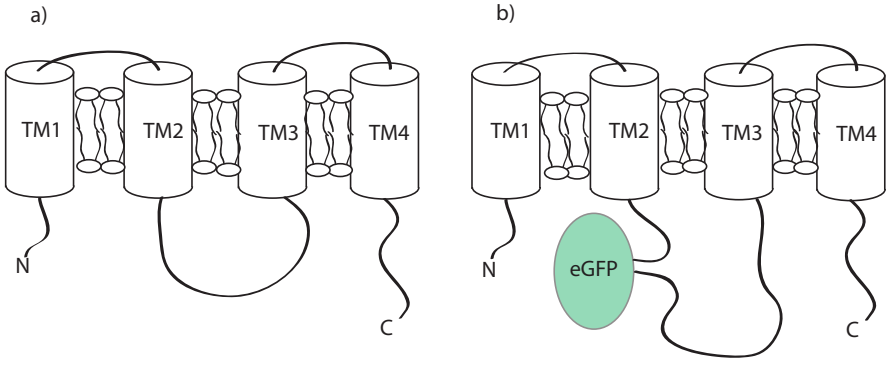


Figure 6.2: A cartoon diagram showing the positioning of eGFP in Mot-GFP-A. *(a)* The helix architecture of wild-type MotA, showing the positioning of the cytoplasmic and periplasmic loop domains. *(b)* The "in loop" GFP-MotA fusion. eGFP was inserted after residue 72 in the cytoplasmic loop between helices 1 and 2, with 5 amino acid linkers either side of the new GFP domain.

To enable this, construct "pDS-Mot-GFP-A" was made, which was designed to replace chromosomal wild-type *motA* with a mutant variant, *mot-GFP-A*. This mutant would add an extra GFP domain (flanked by 5 linker amino acids) to MotA after residue 72 on the cytoplasmic loop between transmembrane helices 1 and 2. It was hypothesised that addition of a GFP domain to this section of the cytoplasmic loop would minimally hinder the MotA-FliG interface.

The process of constructing pDS-Mot-GFP-A is summarised in Figure 6.3. Construction used the following protocol (for primer sequences, see Appendix B:

1. In the first step, the 500 bases upstream of base 217 *motA* were amplified by PCR from the RP437 chromosome using primers *gfp-mota1* and *gfp-mota2*, producing Fragment 1. *gfp-mota1* was designed to add an *Sph*I restriction site at the 5' end of Fragment 1, while *gfp-mota2* was designed to add the 15 bases which encoded the linker between the cytoplasmic loop and the fluorophore at the 3' end.

2. In the second step, *egfp* was amplified from plasmid pEGFP using primers *gfp-mota3* and *gfp-mota4*, producing Fragment 2. *gfp-mota3* was designed to add 15 bases to the 5' end of Fragment 2, producing a complementary sequence to the 3' end of Fragment 1. *gfp-mota4* was designed to remove the stop codon of *gfp* and replace it with 15 bases encoding the second linker between the fluorophore and the cytoplasmic loop at the 3' end.

3. In the third step, the 500 basepairs downstream of *motA* base 217 (including the base itself) was amplified from the RP437 chromosome using primers *gfp-mota5* and *gfp-mota6*. *gfp-mota5* was designed to add 15 bases to the 5' end of Fragment 3, producing a complementary sequence to the 3' of Fragment 2. *gfp-mota6* added a *Sac*I restriction site to the 3' end.

4. The fourth step used overlap-extension PCR (see Section 2.2.1 to ligate Fragments 1 and 2 together, producing a long fragment 4 which had an *Sph*I site at the 5' end and a 3' end which was complementary to Fragment 3.

5. Finally, overlap extension PCR was used to ligate Fragments 3 and 4 together, producing a single long DNA fragment (Fragment 5) with *Sph*I and *Sac*I restriction sites at the 5' and 3' ends respectively. This was digested and ligated into cut vector pDS132, producing pDS-Mot-GFP-A.

Plasmid pDS-Mot-GFP-A was transformed into *E. coli* strain MT02 by electroporation using the method described in Section 2.2.2. Successful incorporation and subsequent loss of vector backbone was selected for using the method described in Section 2.2.3. Correct replacement of *motA* with *mot-gfp-a* was tested for by Southern blotting using a hybridisation probe constructed from *egfp*. Successful integration resulted in observation of a 750 bp band after Southern blot probe development. After further confirmation of integration by DNA sequencing, the new strain MT06 was frozen and stored at -80 °C.

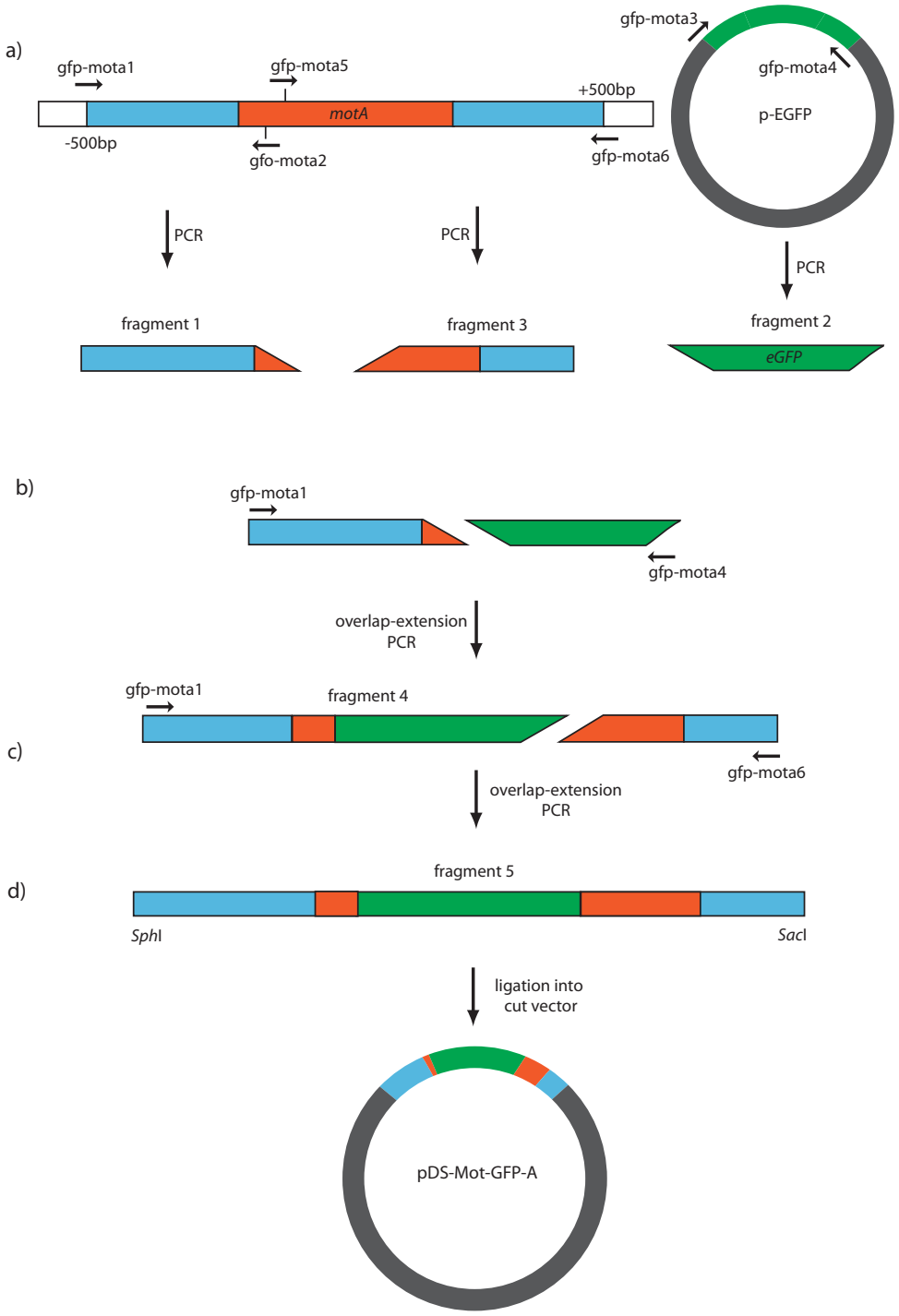


Figure 6.3: A diagram showing the creation process of plasmid pDS-GFPMotA, using two rounds of overlap-extension PCR. *(a)* 500 bp fragments upstream and downstream of codon 216 in *motA* were amplified from the RP437 genome, producing fragments 1 and 3. *egfp* was amplified from plasmid pEGFP, producing fragment 2. *(b)* Fragments 1 and 2 were amplified together using overlap-extension PCR (described in 2.2.1, producing fragment 4. *(c)* Fragments 3 and 4 were amplified together using overlap-extension PCR, producing long fragment 5. *(d)* Fragment 5 was digested using *Sac*I and *Sph*I and ligated into pDS132.

Motility and Fluorescence of Strain MT06

The motility of strain MT06 was tested using a standard *E. coli* bead assay. Cells were grown to OD_{600}0.5 and prepared for a bead assay as described in Section 2.3.2. However, no rotating beads were observed. Cells prepared for a tethered-cell assay (as described in Section 2.3.2) likewise did not display any motility.

The fluorescence of tethered, non-motile cells of strain MT06 was tested using TIRF microscopy. No fluorescence spots were observed in any cells monitored. Background fluorescence in MT04 cells was similar to that of MT02, suggesting that eGFP had failed to fold correctly. Strain MT06 was therefore judged to be unsuitable for further experimental work.

6.3 Motor Integrity and *pmf*

6.3.1 Adaptation of the pR System for Fluorescence Microscopy

The original experimental plan was to use the pR-based *pmf* generation system described in Chapter 3 and utilised in Chapters 4 and 5 to provide a *pmf* for motor function. *pmf* generation would be simultaneous with fluorescence imaging by TIRF microscopy, allowing the effects of rapid *pmf* changes on motor integrity to be monitored. Unfortunately, the use of pR proved to be incompatible with fluorescence imaging of motor components.

The absorption spectrum of pR, although with a clear absorption peak at ∼530 nm, absorbs well at wavelengths from 475-560 nm. This wavelength range overlaps with the absorbance or emission spectra of almost all known fluorescent protein variants. A graph showing the absorbance spectra of example fluorescent proteins and GPR can be seen in Figure 6.4. Illumination with 532 nm light of the intensity required for powering the flagellar motor was found to lead to rapid photobleaching of fluorescent proteins, preventing imaging of tagged motor components.

An alternative method of *pmf* control is to reversibly inhibit the *E. coli* electron transport chain by addition and removal of a respiratory poison. Although this method does not provide the fine time resolution which the pR system makes possible, it does not interfere with the fluorescence techniques used to image tagged motor components. This technique was therefore used to control cellular *pmf* during experiments which used TIRF microscopy to investigate the relationship between motor integrity and *pmf*.

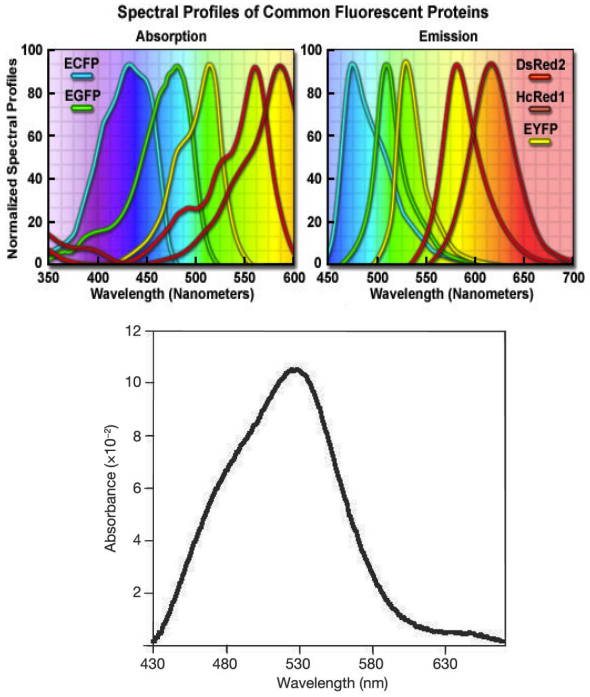


Figure 6.4: A graph comparing the GPR absorption spectrum to several fluorescent proteins. Fluorescence absorption/emission chart was taken from Nikon Microscopy U. (http://www.microscopyu.com/)

6.3.2 Analysis of MT04 Motor Integrity

In this experiment, the dynamics of fluorescently-tagged stator units was examined as physiological *pmf* was lowered to zero and restored by addition and removal of the respiratory poison sodium azide.

Cells of strain MT04 (*gfp-motB, fliC*st) were grown for tethered-cell fluorescence analysis. A colony of MT04 was picked and used to inoculate 5 ml of LB medium. This culture was grown overnight aerobically at 37 °C with shaking. 100 μl of the overnight culture was used to inoculate 5 ml of TB medium; this culture was grown aerobically with shaking until it reached OD_{600}0.6. 1 ml of culture was centrifuged and resuspended in 5 ml *E. coli* motility buffer. Flagella in the resulting cell suspension were sheared as described in Section 2.3.2. The sheared cell suspension was centrifuged and resuspended in 200 μl motility buffer.

The concentrated sheared cell suspension was passed through a flow cell (described in Section 2.3.2), which allowed buffer exchange to be carried out while cells were being imaged. Cells were incubated for 15 minutes, allowing their flagella to tether to the glass coverslip, before the chamber was flushed with 250 μl motility buffer.

Bright-field imaging of the tunnel slide revealed many spinning cells tethered by their flagella. TIRF microscopy revealed the presence of motor spots, corresponding to a concentration of fluorophores at the motor site. An example fluorescence image can be see in Figure 6.5(a).

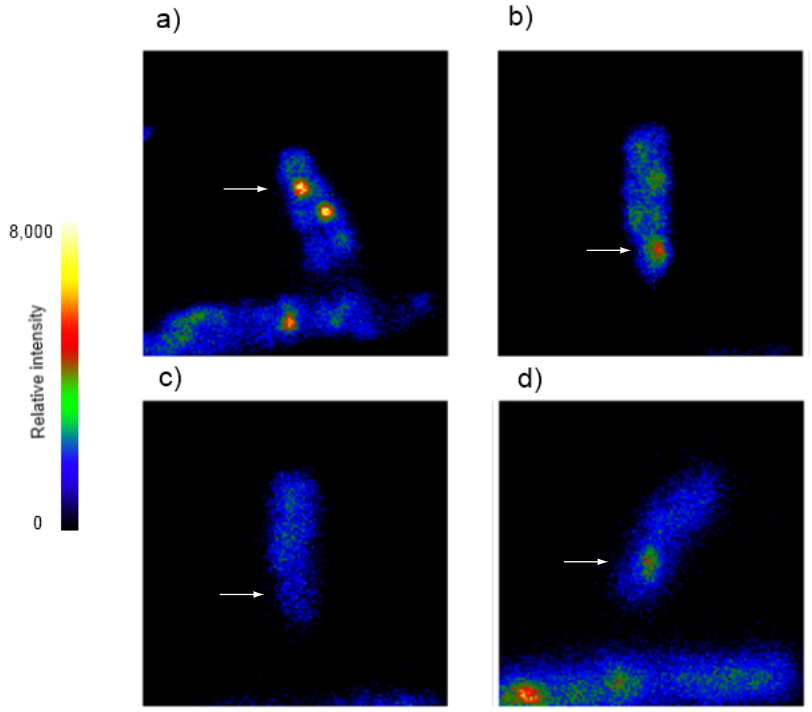


Figure 6.5: Images of *E. coli* strain MT04 taken with TIRF microscopy, showing the effects of *pmf* loss on motor integrity. *(a)* A tethered, rotating cell, showing a discrete GFP-MotB motor spot at the centre of rotation. *pmf* was maintained by the native electron transport chain. *(b)* An image of the same cell 15 seconds after motor stop. A GFP-MotB motor spot remains visible at the former centre of rotation. *(c)* The same cell, 6 minutes after exposure to sodium azide. No motor spot can be observed. *(d)* An image of the same cell 2 minutes after removal of sodium azide. The cell has resumed rotation, and a reformed motor spot, comprising recruited stator units, has appeared at the centre of rotation.

Cells which were tethered by a single flagellum located roughly in the centre of the cell were subjected to further analysis. 1 ml of 20 mM sodium azide solution was passed through the flow cell, causing cells to slow down and gradually reach a complete stop. Complete *pmf* disruption was assumed to occur after complete motor stop, as motor speed is proportional to *pmf* at high load. During this process, motor spot integrity was monitored by the taking of TIRF images every 30 s after addition of azide. Exposure time was 0.1 s. This time interval was chosen to minimise GFP photobleaching, which was a constant risk due to the small numbers of GFP-MotB

present in the cell (∼200 [79]).

Gradual motor spot dissipation was observed after cells had stopped rotating. Figures 6.5(b) and 6.5(c) shows gradual spot disruption after *pmf* loss in the same cell. Motor spots persisted for some time after rotation had ceased, with a gradual loss of intensity over time. However, all motor spots were observed to dissipate completely after 6 minutes. Spot dissipation caused an increase in background fluorescence of cell bodies (the fluorescence intensity of areas without motor spots), indicating that stators had dispersed throughout the plasma membrane. A graph of background fluorescence in *pmf*-disrupted MT04, compared to that of untreated MT04 and MT03 can be seen in Figure 6.6.

After complete motor spot dissipation had been observed, 1 ml of *E. coli* motility buffer was passed through the flow cell, removing sodium azide. This allowed cells to regenerate native *pmf* generation through the electron transport chain. After around 2 minutes, cells could be observed to rotate again, indicating restoration of motor function. Subsequent imaging of the resurrected motor by TIRF microscopy (that is, after motor rotation had resumed) showed the restoration of a discrete motor spot at the centre of rotation, indicating that stators had reattached to the motor after *pmf* restoration. Figure 6.5(c) shows return of a fluorescent spot after return of rotation in the cell observed previously.

6.3.3 Analysis of MT05 Motor Integrity

The experiment described in Section 6.3.2 showed that stator binding was disrupted after *pmf* disruption *in vivo*. To test whether the integrity of the flagellar motor switch complex was affected by loss of *pmf*, YPet-FliM dynamics were monitored as *pmf* was disrupted and restored by addition and removal of sodium azide. Since FliM is not directly involved in *pmf*-dependent torque generation, it was thought maintenance of spot integrity would be independent of cellular *pmf*.

Cells of strain MT05 (*yPet-FliM*, *fliC*st) were grown and prepared for a tethered-cell assay using a similar protocol as that used for preparation of strain MT04. Cells were grown to OD_{600}0.6 in TB medium at 30 °C with shaking. 1 ml of culture was centrifuged and resuspended in 1 ml *E. coli* motility buffer. Flagellar filaments of cells in suspension were sheared, and the sheared cell suspension was centrifuged and resuspended in 200 μl motility buffer.

This concentrated sheared cell suspension was passed through a tunnel slide. The slide was incubated for 15 minutes to allow cells to bind to the glass via their flagella. 200 μl motility buffer was passed through the slide to remove loose cells.

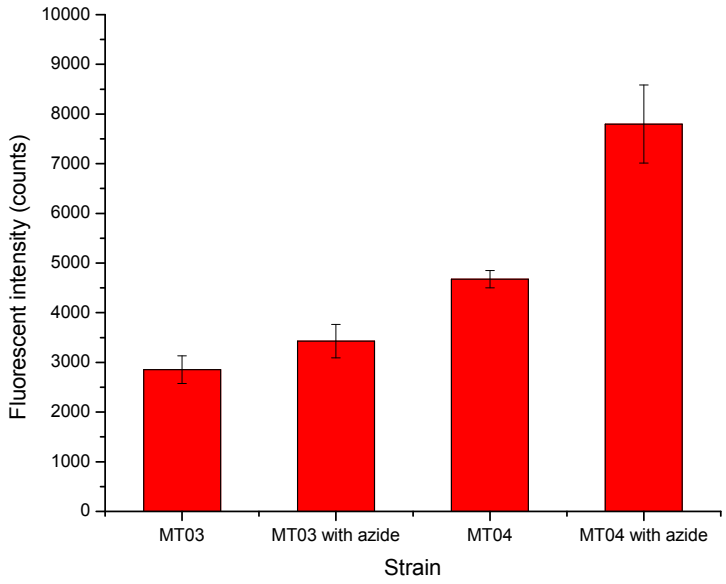


Figure 6.6: A graph comparing background fluorescence (at 473 nm) of 25 cells of strains MT03 and MT04 at physiological and zero *pmf*. Background fluorescence intensity of strain MT04 increased with loss of *pmf* – this is probably a consequence of stators leaving the motor and entering the membrane pool under these conditions.

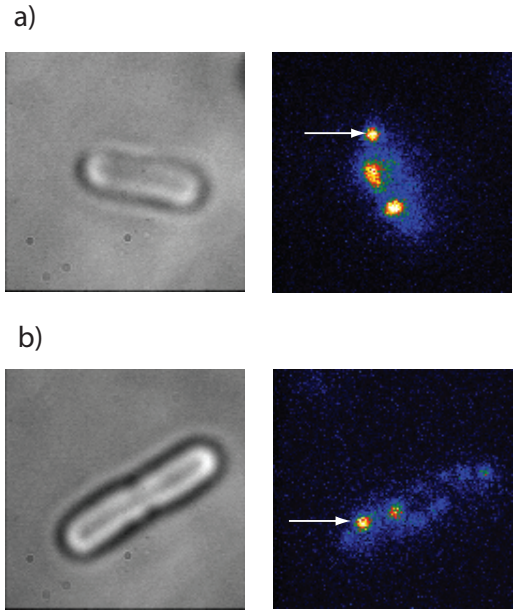


Figure 6.7: Two cells of strain MT05 (*yPet-fliM, fliC*st), imaged using TIRF microscopy. *(a)* A tethered, rotating cell of strain MT05, showing a motor spot at the centre of rotation. *(b)* A tethered cell which had been exposed to 20 mM sodium azide, imaged 5 minutes after it had ceased rotating. Arrows show centre of rotation. Note persistence of discrete FliMN fluorescence 5 minutes after azide exposure in contrast to the previous result for MotB.

Immediately before analysis, 50 μl of 20 mM sodium azide solution was passed through the tunnel slide. Bright-field imaging of tethered cells showed gradual cell slowdown as *pmf* generation was inhibited by sodium azide. Once cells had reached a complete stop, they were left for 5 minutes to allow any YPet-FliM dispersal to take place. Imaging of cells after 10 minutes revealed the presence of persistent YPet-FliM motor spots, indicating that FliM binding did not depend on the presence of *pmf*. Example images of MT05 cells before and after treatment with sodium azide can be seen in Figure 6.7.

6.4 CONCLUSIONS

In this chapter, fluorescently-tagged *E. coli* strains MT04 (*gfp-motB, fliCst*) and MT05 (*yPet-fliM, fliCst*) were created by replacing chromosomal *fliC* with *fliCst*. These strains were used to investigate the effects of *pmf* loss on the integrity of the flagellar motor. Additionally, the creation of a novel MotA-GFP fusion was attempted, but the resulting strain (MT06) was shown to be non-functional.

The results in this chapter demonstrate that stator binding to functional *E. coli* motors *in vivo* is dependent on the presence of a *pmf*. Stator binding has previously been shown to be non-permanent and reversible [79], with stator complexes capable of entering and leaving the motor. This work shows stator attachment to be a dynamic, *pmf*-dependent process – as *pmf* decreases, stator binding weakens, with stators eventually leaving the motor entirely and entering the membrane pool. Stator loss corresponded with an increase in cellular background fluorescence. *pmf*-dependent stator loss was shown to be reversible, as removal of sodium azide resulted in motor resurrection and return of a fluorescent motor spot.

GFP-MotB spot persistence was observed after motor stop in experiments investigating the effects of *pmf* loss in strain MT04. Assuming that motor speed is directly proportional to *pmf*, stator dissociation must be slower than the rate of *pmf* loss. Motors were shown to stop in seconds, while stator detachment appears to take place on a timescale of minutes. This result agrees well with the speed/time studies in Chapter 5 (described in Section 5.2), where motors subjected to longer periods at zero *pmf* took much longer to recover in speed than those subjected to shorter periods. The existence of a delay between loss of *pmf* and loss of stators implies that some kind of conformational change must take place in the stator before it is able to leave the motor entirely.

Such a confomational change has already been proposed to account for the open-

ing of the stator ion channel upon stator binding to the motor basal body. In stators not attached to flagellar motors, the peptidoglycan-binding (PGB) domain of MotB is thought to act as a "plug domain", preventing ion translocation and so preventing "short-circuiting" of *pmf* across the plasma membrane. Upon stator binding, the PGB domain of MotB has been proposed to move 100 Å, binding to peptidoglycan upon stator attachment to the motor and opening the stator ion channel [59] citeKojima:2009p1040. Such an interaction may be the limiting step in stator attachment and detachment to the flagellar motor. Further work into the rates and mechanisms of stator binding would provide needed detail on this process.

pmf-dependent changes in integrity were not observed for the switch complex protein FliM, which forms a 34-mer complex as part of the motor C-ring. This protein undergoes a limited degree of turnover in *E. coli*; however, the results of this study show that *pmf* loss does not result in complete disintegration of the FliM ring. Such a result is consistent with the role of FliM; it is not involved in ion translocation and does not play a direct role in motor torque generation.

Chapter 7

Discussion and Future Work

It is tempting when thinking of the bacterial flagellar motor to think of it as a singular device which is built and used, in a similar fashion to its man-made counterparts. However, a growing series of studies are beginning to explore the dynamic nature of the motor. Different motor components, such as the torque-generating stators, have been shown to constantly diffuse in and out of the membrane pool, transiently binding to and leaving functioning motors. In a way, there is no such thing as a "finished" flagellar motor – different components enter, leave, bind to and are released from the motor depending on the state of the cell and its surroundings.

This work aimed to investigate the relationship between the flagellar motor and its source of power, the ion-motive force. In Chapter 3, a novel system for investigating motor output with *pmf* was developed, which used the relatively newly-discovered light-driven proton pump proteorhodopsin (pR) to generate a *pmf* sufficient to drive the motor at wild-type levels *in vivo*. This system was designed to be compatible with BFP interferometry techniques, allowing motor output to be precisely measured.

Although the system developed in Chapter 3 is robust and effective, further improvements could be made. Changing light intensity during experiments is an unwieldy process, involving manually changing the position of a filter wheel. By adding an optional second path for the 532 nm laser, intensity could be quickly switched between two different (and non-zero) values. This could be relatively easily accomplished by adding a semi-silvered mirror to split the path, with output controlled by a programmable shutter.

The pR-based *pmf* generation system need not be exclusively used to study the *E. coli* motor. Proteorhodopsin is expressible in many different organisms, allowing experiments of this type to be carried out in other organisms such as *Salmonella* and *Rhodobacter*. pR-based *pmf* generation could be used to investigate other *pmf*-dependent processes, such as *Myxococcus* gliding motility or solute transport.

In Chapter 4, the pR-based *pmf* generation system was used to characterise the effects of *pmf* changes on the motor. The flagellar motor was shown to respond to *pmf* levels above the physiological norm with a corresponding increase in motor speed. This speed increase was very fast, on the order of a millisecond, with strong evidence that it was not due to binding of additional torque-generating units to the flagellar motor (see 4.2). Lowered *pmf* was shown to reduce stability of motor speed *in vivo*. Using the pR-based *pmf* generation, the motor could be forced to

slow down to ∼3 % of its normal speed, showing the stepping action of the flagellar motor. Motors were observed to dwell at different stop angles between periods of more stable rotation.

The work described in this thesis dealt with *pmf* values relative to motor output, such as "full" and "zero" *pmf*. By using voltage-sensitive Nernstian membrane dyes such as TMRM, absolute values for pR output under various conditions could be obtained. pR itself has recently been shown to be weakly fluorescent, with fluorescence depending on the membrane voltage gradient; the relationship between membrane voltage and motor output could be further investigated by using pR in a dual role to both generate and measure membrane voltage.

Motors behave differently depending on the load placed on them. All of the experiments in this thesis deliberately minimised any load-dependent effects, by ensuring that motors were always subjected to high-load regimes. The pR-based *pmf* system could be used to investigate the effects of *pmf* changes on motors at lower loads using smaller polystyrene or gold nanobeads, examining the limiting factors on motor speed under this regime.

Chapter 5 investigated the effects of *pmf* loss on the motor. Motors were shown to display a two-stage decrease in speed upon *pmf* disruption, reducing to a small proportion (∼20 %) of the initial speed within milliseconds, and subsequently decreasing more slowly to a complete stop. This speed decrease was shown to be separate to the effects of cell poisoning. Transient *pmf* disruption was shown not to result in stator loss *in vivo*, with motors rapidly recovering after *pmf* restoration. Inactivation of stators was shown to be a time-dependent process. By subjecting cells to extended periods at zero *pmf*, sequential activation of stators could be observed *in vivo* in a manner similar to classical motor resurrection experiments.

The results in this chapter show that stators begin to leave the flagellar motor over a timescale of several seconds, rather than dispersing instantly upon *pmf* loss. Further work would aim to quantify the rates of stator loss and stator binding, allowing the stator binding constant at physiological *pmf* to be determined. Given that the motor appears to become unstable at lower *pmf*, future work could investigate the possible relationship between *pmf* and the affinity of stator units for the motor.

If the two stages of speed reduction after *pmf* disruption are a result of loss of the two components of *pmf* at different rates (first $\Delta\psi$, then ΔpH), the two could be separated by using nigericin and valinomycin to disrupt each component indi-

vidually. One would expect to see no rapid loss in speed after *pmf* disruption in valinomycin-treated cells; with nigericin treatment, motors should stop immediately once illumination is ended in pR-powered cells.

The effects of *pmf* loss and restoration on the motor were directly observed in Chapter 6 using TIRF microscopy to image the positioning of fluorescently-tagged functional stators at physiological *pmf*. Stator units could be seen to physically leave the motor on a timescale of minutes, returning to the motor to generate torque after restoration of *pmf*. Motors were observed to rotate before complete return of the motor spot, showing that individual stators can drive the rotation of the entire motor. This effect was not seen in the switch complex protein FliM, which is not directly involved in torque generation.

Further work in this area would aim to quantify the rates of stator loss to the membrane pool, providing independent confirmation of a constant for stator binding at physiological *pmf*. Work is also ongoing to modify the TIRF microscopy system so that illumination for pR-based *pmf* generation can be combined with fluorescence microscopy; this system would allow stator behaviour to be directly examined at much higher time resolution.

The central aim of this project was to develop a novel pR-based motor assay, and use it to investigate the relationship between the motor and the *pmf* which drives it. Individual *E. coli* cells were modified by expressing the light-driven proton pump proteorhodopsin, allowing them to generate enough useful energy from a single light source to power the flagellar motor. Using this system, motors could be shown to be started, stopped, slowed down and sped up beyond the physiological norm simply by changing the degree of illumination. A series of "resurrection" experiments showed that stator units in the motor deactivated after *pmf* loss *in vivo* in a time-dependent fashion. Finally, the integrity of the motor itself was shown to be dependent on the presence of a *pmf*, as stator units seem to require active movement of protons to maintain their position around the motor basal body.

Bibliography

[1] Anand, G. S., Goudreau, P. N., Lewis, J. K., and Stock, A. M. Evidence for phosphorylation-dependent conformational changes in methylesterase CheB. *Protein Science 9*, 5 (May 2000), 898–906.

[2] Andersson, M., Malmerberg, E., Westenhoff, S., Katona, G., Cammarata, M., Wöhri, A. B., Johansson, L. C., Ewald, F., Eklund, M., Wulff, M., Davidsson, J., and Neutze, R. Structural dynamics of light-driven proton pumps. *Structure/Folding and Design 17*, 9 (Sep 2009), 1265–1275.

[3] Armitage, J. P., and Macnab, R. M. Unidirectional, intermittent rotation of the flagellum of *Rhodobacter sphaeroides*. *J Bacteriol 169*, 2 (Feb 1987), 514–8.

[4] Armstrong, J. B., and Adler, J. Complementation of nonchemotactic mutants of *Escherichia coli*. *Genetics 61*, 1 (Jan 1969), 61–6.

[5] Asai, Y., Yakushi, T., Kawagishi, I., and Homma, M. Ion-coupling determinants of Na^+-driven and H^+-driven flagellar motors. *J Mol Biol 327*, 2 (Mar 2003), 453–63.

[6] Axelrod, D. Total internal reflection fluorescence microscopy in cell biology. *Traffic 2*, 11 (Jan 2001), 764–774.

[7] Bai, F., Branch, R. W., Nicolau, D. V., Pilizota, T., Steel, B. C., Maini, P. K., and Berry, R. M. Conformational spread as a mechanism for cooperativity in the bacterial flagellar switch. *Science 327*, 5966 (Feb 2010), 685–9.

[8] Bai, W., Zhao, K. S., and Asami, K. Dielectric properties of *E. coli* cells as simulated by the three-shell spheroidal model. *Biophys Chem 122*, 2 (Jul 2006), 136–42.

[9] Bardy, S. L., Ng, S. Y., and Jarrell, K. F. Recent advances in the structure and assembly of the archaeal flagellum. *J Mol Microbiol Biotechnol 7*, 1-2 (Jan 2004), 41–51.

[10] Behe, M. *Darwin's Black Box: the Biochemical Challenge to Evolution*. Free Press, 1996.

[11] Béjà, O., Aravind, L., Koonin, E. V., Suzuki, M. T., Hadd, A., Nguyen, L. P., Jovanovich, S. B., Gates, C. M., Feldman, R. A., Spudich, J. L., Spudich, E. N., and DeLong, E. F. Bacterial rhodopsin: Evidence for a new type of phototrophy in the sea. *Science 289*, 5486 (09 2000), 1902–1906.

[12] Berg, H. C., and Tedesco, P. M. Transient response to chemotactic stimuli in *Escherichia coli*. *Proc Natl Acad Sci USA 72*, 8 (Aug 1975), 3235–9.

[13] Berg, H. C., and Turner, L. Torque generated by the flagellar motor of *Escherichia coli*. *Biophys J 65*, 5 (Nov 1993), 2201–16.

[14] Bergo, V. B., Sineshchekov, O. A., Kralj, J. M., Partha, R., Spudich, E. N., Rothschild, K. J., and Spudich, J. L. His-75 in proteorhodopsin, a novel component in light-driven proton translocation by primary pumps. *J Biol Chem 284*, 5 (Jan 2009), 2836–43.

[15] Berry, R. M. Torque and switching in the bacterial flagellar motor. an electrostatic model. *Biophys J 64*, 4 (Apr 1993), 961–73.

[16] Berry, R. M., and Armitage, J. P. Response kinetics of tethered *Rhodobacter sphaeroides* to changes in light intensity. *Biophys J 78*, 3 (Nov 2000), 1207–1215.

[17] Berry, R. M., and Berg, H. C. Torque generated by the flagellar motor of *Escherichia coli* while driven backward. *Biophys J 76*, 1 (Nov 1999), 580–587.

[18] Bertin, P., Terao, E., Lee, E., Lejeune, P., Colson, C., Danchin, A., and Collatz, E. The h-ns protein is involved in the biogenesis of flagella in *Escherichia coli*. *J Bacteriol 176*, 17 (Sep 1994), 5537–5540.

[19] Blair, D. F., and Berg, H. C. Restoration of torque in defective flagellar motors. *Science 242*, 4886 (Dec 1988), 1678–81.

[20] Block, S. M., Segall, J. E., and Berg, H. C. Adaptation kinetics in bacterial chemotaxis. *J Bacteriol 154*, 1 (Apr 1983), 312–23.

[21] Boehm, A., Kaiser, M., Li, H., Spangler, C., Kasper, C. A., Ackermann, M., Kaever, V., Sourjik, V., Roth, V., and Jenal, U. Second messenger-mediated adjustment of bacterial swimming velocity. *Cell 141*, 1 (Apr 2010), 107–16.

[22] Borkovich, K. A., and Simon, M. I. The dynamics of protein phosphorylation in bacterial chemotaxis. *Cell 63*, 6 (Dec 1990), 1339–48.

[23] Brown, P., and Hill, C. Crystal structure of the middle and C-terminal domains of the flagellar rotor protein FliG. *EMBO J* (Jan 2002).

[24] Brown, P., Mathews, M. A. A., Joss, L. A., Hill, C. P., and Blair, D. F. Crystal structure of the flagellar rotor protein FliN from *Thermotoga maritima*. *Journal of Bacteriology 187*, 8 (Apr 2005), 2890–902.

[25] Chandler, J. H. *Characterisation of the Stator Complexes of the Escherichia coli flagellar motor*. PhD thesis, University of Oxford, 2006.

[26] Charon, N. W., and Goldstein, S. F. Genetics of motility and chemotaxis of a fascinating group of bacteria: The *Spirochetes*. *Annu. Rev. Genet. 36*, 1 (Dec 2002), 47–73.

[27] Cluzel, P., Surette, M., and Leibler, S. An ultrasensitive bacterial motor revealed by monitoring signaling proteins in single cells. *Science 287*, 5458 (Mar 2000), 1652–5.

[28] Cohen-Ben-Lulu, G. N., Francis, N. R., Shimoni, E., Noy, D., Davidov, Y., Prasad, K., Sagi, Y., Cecchini, G., Johnstone, R. M., and Eisenbach, M. The bacterial flagellar switch complex is getting more complex. *EMBO J 27*, 7 (Apr 2008), 1134–44.

[29] Cohen-Krausz, S., and Trachtenberg, S. The structure of the archeabacterial flagellar filament of the extreme halophile halobacterium salinarum R1M1 and its relation to eubacterial flagellar filaments and type IV pili. *J Mol Biol 321*, 3 (Aug 2002), 383–395.

[30] Cohen-Krausz, S., and Trachtenberg, S. The flagellar filament structure of the extreme acidothermophile *Sulfolobus shibatae* B12 suggests that archaeabacterial flagella have a unique and common symmetry and design. *J Mol Biol 375*, 4 (Jan 2008), 1113–24.

[31] Craggs, T. D. Green fluorescent protein: structure, folding and chromophore maturation. *Chem. Soc. Rev. 38*, 10 (Jan 2009), 2865.

[32] Craig, L., Pique, M. E., and Tainer, J. A. Type IV pilus structure and bacterial pathogenicity. *Nat Rev Micro 2*, 5 (May 2004), 363–378.

[33] Crespi, M., and Gálvez, S. Molecular mechanisms in root nodule development. *J Plant Growth Regul 19*, 2 (Jun 2000), 155–166.

[34] Deckert, G., Warren, P. V., Gaasterland, T., Young, W. G., Lenox, A. L., Graham, D. E., Overbeek, R., Snead, M. A., Keller, M., Aujay, M., Huber, R., Feldman, R. A., Short, J. M., Olsen, G. J., and Swanson, R. V. The complete genome of the hyperthermophilic bacterium *Aquifex aeolicus*. *Nature 392*, 6674 (Mar 1998), 353–8.

[35] Delalez, N. J. *Dynamics of Flagellar Motor Proteins*. PhD thesis, University of Oxford, Nov 2009.

[36] Delalez, N. J., Wadhams, G. H., Rosser, G., Xue, Q., Brown, M. T., Dobbie, I. M., Berry, R. M., Leake, M. C., and Armitage, J. P. Signal-dependent turnover of the bacterial flagellar switch protein FliM. *Proc Natl Acad Sci USA 107*, 25 (Jun 2010), 11347–51.

[37] DePamphilis, M. L., and Adler, J. Fine structure and isolation of the hook-basal body complex of flagella from *Escherichia coli* and *Bacillus subtilis*. *Journal of Bacteriology 105*, 1 (Jan 1971), 384–95.

[38] Dioumaev, A. K., Brown, L. S., Shih, J., Spudich, E. N., Spudich, J. L., and Lanyi, J. K. Proton transfers in the photochemical reaction cycle of proteorhodopsin. *Biochemistry 41*, 17 (Apr 2002), 5348–58.

[39] Djordjevic, S., and Stock, A. M. Chemotaxis receptor recognition by protein methyltransferase CheR. *Nat Struct Biol 5*, 6 (Jun 1998), 446–50.

[40] Doyle, J. J. The rest of the iceberg: Legume diversity and evolution in a phylogenetic context. *Plant Physiology 131*, 3 (Mar 2003), 900–910.

[41] Duke, T., Novère, N. L., and Bray, D. Conformational spread in a ring of proteins: a stochastic approach to allostery. *J Mol Biol 308*, 3 (May 2001), 541–553.

[42] Fan, F., and Macnab, R. M. Enzymatic characterization of FliI. An ATPase involved in flagellar assembly in salmonella typhimurium. *J Biol Chem 271*, 50 (Dec 1996), 31981–8.

[43] Francis, N. R., Irikura, V. M., Yamaguchi, S., DeRosier, D. J., and Macnab, R. M. Localization of the *Salmonella typhimurium* flagellar switch protein FliG to the cytoplasmic M-ring face of the basal body. *Proc Natl Acad Sci USA 89*, 14 (Jul 1992), 6304–8.

[44] Friedrich, T., Geibel, S., Kalmbach, R., Chizhov, I., Ataka, K., Heberle, J., Engelhard, M., and Bamberg, E. Proteorhodopsin is a light-driven proton pump with variable vectoriality. *J Mol Biol 321*, 5 (Aug 2002), 821–38.

[45] Frigaard, N.-U., Martinez, A., Mincer, T. J., and Delong, E. F. Proteorhodopsin lateral gene transfer between marine planktonic Bacteria and Archaea. *Nature 439*, 7078 (Feb 2006), 847–850.

[46] Fukuoka, H., Inoue, Y., Terasawa, S., Takahashi, H., and Ishijima, A. Exchange of rotor components in functioning bacterial flagellar motor. *Biochemical and Biophysical Research Communications 394*, 1 (Mar 2010), 130–135.

[47] Fukuoka, H., Wada, T., Kojima, S., Ishijima, A., and Homma, M. Sodium-dependent dynamic assembly of membrane complexes in sodium-driven flagellar motors. *Molecular Microbiology 71*, 4 (Feb 2009), 825–835.

[48] Fung, D. C., and Berg, H. C. Powering the flagellar motor of *Escherichia coli* with an external voltage source. *Nature 375*, 6534 (Jun 1995), 809–12.

[49] Gabel, C. V., and Berg, H. C. The speed of the flagellar rotary motor of *Escherichia coli* varies linearly with protonmotive force. *Proc Natl Acad Sci USA 100*, 15 (Jul 2003), 8748–51.

[50] Gauthier, M., Truchon, D., and Rainville, S. Taking control of the flagellar motor. *Proceedings of SPIE 7099* (Jan 2008), 70990F–70990F–6.

[51] Ghosh, A., Hartung, S., Does, C. V. D., Tainer, J. A., and Albers, S. Archaeal flagellar ATPase motor shows ATP-dependent hexameric assembly and activity stimulation by specific lipid binding. *Biochem. J. 437*, 1 (Jun 2011), 43–52.

[52] Giovannoni, S. J., Bibbs, L., Cho, J.-C., Stapels, M. D., Desiderio, R., Vergin, K. L., Rappé, M. S., Laney, S., Wilhelm, L. J., Tripp, H. J., Mathur, E. J., and Barofsky, D. F. Proteorhodopsin in the ubiquitous marine bacterium SAR11. *Nature 438*, 7064 (Nov 2005), 82–85.

[53] Gómez-Consarnau, L., Akram, N., Lindell, K., Pedersen, A., Neutze, R., Milton, D. L., González, J. M., and Pinhassi, J. Proteorhodopsin phototrophy promotes survival of marine bacteria during starvation. *PLoS Biol 8*, 4 (Apr 2010), e1000358.

[54] Haldimann, A., and Wanner, B. L. Conditional-replication, integration, excision, and retrieval plasmid-host systems for gene structure-function studies of bacteria. *Journal of Bacteriology 183*, 21 (Nov 2001), 6384–93.

[55] Hazelbauer, G. L., Falke, J. J., and Parkinson, J. S. Bacterial chemoreceptors: high-performance signaling in networked arrays. *Trends Biochem Sci 33*, 1 (Jan 2008), 9–19.

[56] Henderson, G. P., and Jensen, G. J. Three-dimensional structure of Mycoplasma pneumoniae's attachment organelle and a model for its role in gliding motility. *Molecular Microbiology 60*, 2 (Apr 2006), 376–385.

[57] Hirano, T., Minamino, T., Namba, K., and Macnab, R. M. Substrate specificity classes and the recognition signal for *Salmonella* type III flagellar export. *Journal of Bacteriology 185*, 8 (Apr 2003), 2485–92.

[58] Hirano, T., Yamaguchi, S., Oosawa, K., and Aizawa, S. Roles of FliK and FlhB in determination of flagellar hook length in *Salmonella typhimurium*. *Journal of Bacteriology 176*, 17 (Sep 1994), 5439–49.

[59] Hosking, E. R., Vogt, C., Bakker, E. P., and Manson, M. D. The *Escherichia coli* MotAB proton channel unplugged. *J Mol Biol 364*, 5 (Dec 2006), 921–37.

[60] Inoue, Y., Lo, C.-J., Fukuoka, H., Takahashi, H., Sowa, Y., Pilizota, T., Wadhams, G. H., Homma, M., Berry, R. M., and Ishijima,

A. Torque-speed relationships of Na^+-driven chimeric flagellar motors in *Escherichia coli*. *J Mol Biol 376*, 5 (Mar 2008), 1251–9.

[61] Irie, Y., and Parsek, M. R. Quorum sensing and microbial biofilms. *Curr Top Microbiol Immunol 322* (Jan 2008), 67–84.

[62] Jarrell, K. F., and Mcbride, M. J. The surprisingly diverse ways that prokaryotes move. *Nat Rev Micro 6*, 6 (Jun 2008), 466–476.

[63] Jones, C. J., Macnab, R. M., Okino, H., and Aizawa, S. Stoichiometric analysis of the flagellar hook-(basal-body) complex of *Salmonella typhimurium*. *J Mol Biol 212*, 2 (Mar 1990), 377–87.

[64] Josenhans, C., and Suerbaum, S. The role of motility as a virulence factor in bacteria. *Int J Med Microbiol 291*, 8 (Mar 2002), 605–14.

[65] Kaiser, D. *Myxococcus* - from single-cell polarity to complex multicellular patterns. *Annu. Rev. Genet. 42*, 1 (Dec 2008), 109–130.

[66] Kamiya, R., Asakura, S., Wakabayashi, K., and Namba, K. Transition of bacterial flagella from helical to straight forms with different subunit arrangements. *J Mol Biol 131*, 4 (Jul 1979), 725–42.

[67] Kim, E. A., Price-Carter, M., Carlquist, W. C., and Blair, D. F. Membrane segment organization in the stator complex of the flagellar motor: implications for proton flow and proton-induced conformational change. *Biochemistry 47*, 43 (Oct 2008), 11332–9.

[68] Kim, K. K., Yokota, H., and Kim, S. H. Four-helical-bundle structure of the cytoplasmic domain of a serine chemotaxis receptor. *Nature 400*, 6746 (Aug 1999), 787–92.

[69] Klare, J. P., Chizhov, I., and Engelhard, M. Microbial rhodopsins: scaffolds for ion pumps, channels, and sensors. *Results Probl Cell Differ 45* (Jan 2008), 73–122.

[70] Klyszejko, A. L., Shastri, S., Mari, S. A., Grubmüller, H., Muller, D. J., and Glaubitz, C. Folding and assembly of proteorhodopsin. *J Mol Biol 376*, 1 (Feb 2008), 35–41.

[71] Koerdt, A., Gödeke, J., Berger, J., Thormann, K. M., and Albers, S.-V. Crenarchaeal biofilm formation under extreme conditions. *PLoS ONE 5*, 11 (Nov 2010), e14104.

[72] Kojima, S., Imada, K., Sakuma, M., Sudo, Y., Kojima, C., Minamino, T., Homma, M., and Namba, K. Stator assembly and activation mechanism of the flagellar motor by the periplasmic region of MotB. *Molecular Microbiology 73*, 4 (Aug 2009), 710–718.

[73] Komeda, Y., Suzuki, H., ichi Ishidsu, J., and Iino, T. The role of cAMP in flagellation of *Salmonella typhimurium*. *Molecular and General Genetics MGG 142*, 4 (Dec 1975), 289–298.

[74] Kralj, J. M., Hochbaum, D. R., Douglass, A. D., and Cohen, A. E. Electrical spiking in *Escherichia coli* probed with a fluorescent voltage-indicating protein. *Science 333*, 6040 (Jul 2011), 345–348.

[75] Kudo, S., Magariyama, Y., and Aizawa, S. Abrupt changes in flagellar rotation observed by laser dark-field microscopy. *Nature 346*, 6285 (Aug 1990), 677–80.

[76] Kuwajima, G. Construction of a minimum-size functional flagellin of *Escherichia coli*. *Journal of Bacteriology 170*, 7 (July 1988), 3305–3309.

[77] Larsen, S. H., Adler, J., Gargus, J. J., and Hogg, R. W. Chemomechanical coupling without ATP: the source of energy for motility and chemotaxis in bacteria. *Proc Natl Acad Sci USA 71*, 4 (Apr 1974), 1239–43.

[78] Läuger, P. Torque and rotation rate of the bacterial flagellar motor. *Biophys J 53*, 1 (Jan 1988), 53–65.

[79] Leake, M. C., Chandler, J. H., Wadhams, G. H., Bai, F., Berry, R. M., and Armitage, J. P. Stoichiometry and turnover in single, functioning membrane protein complexes. *Nature 443*, 7109 (Sep 2006), 355–8.

[80] Lee, L. K., Ginsburg, M. A., Crovace, C., Donohoe, M., and Stock, D. Structure of the torque ring of the flagellar motor and the molecular basis for rotational switching. *Nature 466*, 7309 (Aug 2010), 996–1000.

[81] Lichstein, H. C., and Soule, M. H. Studies of the effect of sodium azide on microbic growth and respiration: IV. The effect of sodium azide on glucose fermentation and lactic acid production by *Streptococci* and *Lactobacilli*. *Journal of Bacteriology 47*, 3 (Mar 1944), 253–7.

[82] Lippincott-Schwartz, J., and Patterson, G. Development and use of fluorescent protein markers in living cells. *Science 300*, 5616 (Apr 2003), 87–91.

[83] Little, M. A., Steel, B. C., Bai, F., Sowa, Y., Bilyard, T., Mueller, D. M., Berry, R. M., and Jones, N. S. Steps and bumps: Precision extraction of discrete states of molecular machines. *Biophys J 101*, 2 (Jul 2011), 477–485.

[84] Lloyd, S. A., and Blair, D. F. Charged residues of the rotor protein FliG essential for torque generation in the flagellar motor of *Escherichia coli*. *J Mol Biol 266*, 4 (Mar 1997), 733–44.

[85] Lo, C.-J., Leake, M. C., Pilizota, T., and Berry, R. M. Nonequivalence of membrane voltage and ion-gradient as driving forces for the bacterial flagellar motor at low load. *Biophys J 93*, 1 (Jul 2007), 294–302.

[86] Macnab, R. How bacteria assemble flagella. *annualreviews.org 57* (Jan 2003), 77–100.

[87] Macnab, R. M., and Ornston, M. K. Normal-to-curly flagellar transitions and their role in bacterial tumbling. Stabilization of an alternative quaternary structure by mechanical force. *J Mol Biol 112*, 1 (May 1977), 1–30.

[88] Magariyama, Y., Sugiyama, S., Muramoto, K., Maekawa, Y., Kawagishi, I., Imae, Y., and Kudo, S. Very fast flagellar rotation. *Nature 371*, 6500 (Oct 1994), 752.

[89] Manson, M. D., Tedesco, P., Berg, H. C., Harold, F. M., and der Drift, C. V. A protonmotive force drives bacterial flagella. *Proc Natl Acad Sci USA 74*, 7 (Jul 1977), 3060–4.

[90] Manson, M. D., Tedesco, P. M., and Berg, H. C. Energetics of flagellar rotation in bacteria. *J Mol Biol 138*, 3 (Apr 1980), 541–61.

[91] Martinez, A., Bradley, A. S., Waldbauer, J. R., Summons, R. E., and DeLong, E. F. Proteorhodopsin photosystem gene expression enables photophosphorylation in a heterologous host. *Proc Natl Acad Sci USA 104*, 13 (Mar 2007), 5590–5.

[92] Mattick, J. S. Type IV pili and twitching motility. *Annu Rev Microbiol 56*, 1 (Oct 2002), 289–314.

[93] Mauriello, E. M. F., Mignot, T., Yang, Z., and Zusman, D. R. Gliding motility revisited: How do the *Myxobacteria* move without flagella? *Microbiology and Molecular Biology Reviews 74*, 2 (Jun 2010), 229–249.

[94] Meacci, G., Lan, G., and Tu, Y. Dynamics of the bacterial flagellar motor: The effects of stator compliance, back steps, temperature, and rotational asymmetry. *Biophys J 100*, 8 (Apr 2011), 1986–1995.

[95] Meacci, G., and Tu, Y. Dynamics of the bacterial flagellar motor with multiple stators. *Proc Natl Acad Sci USA 106*, 10 (Mar 2009), 3746–51.

[96] Meister, M., Caplan, S. R., and Berg, H. C. Dynamics of a tightly coupled mechanism for flagellar rotation. Bacterial motility, chemiosmotic coupling, protonmotive force. *Biophys J 55*, 5 (Oct 1989), 905–914.

[97] Meister, M., Lowe, G., and Berg, H. C. The proton flux through the bacterial flagellar motor. *Cell 49*, 5 (Jun 1987), 643–50.

[98] Merritt, P. M., Danhorn, T., and Fuqua, C. Motility and chemotaxis in *Agrobacterium tumefaciens* surface attachment and biofilm formation. *J Bacteriol 189*, 22 (Nov 2007), 8005–8014.

[99] Miller, L. D., Yost, C. K., Hynes, M. F., and Alexandre, G. The major chemotaxis gene cluster of *Rhizobium leguminosarum bv. viciae* is essential for competitive nodulation. *Molecular Microbiology 63*, 2 (Nov 2006), 348–362.

[100] Minamino, T., Imada, K., and Namba, K. Mechanisms of type III protein export for bacterial flagellar assembly. *Mol. BioSyst. 4*, 11 (Jan 2008), 1105.

[101] Minamino, T., Imada, K., and Namba, K. Molecular motors of the bacterial flagella. *Curr Opin Struct Biol 18*, 6 (Dec 2008), 693–701.

[102] Minamino, T., and Namba, K. Distinct roles of the FliI ATPase and proton motive force in bacterial flagellar protein export. *Nature 451*, 7177 (Jan 2008), 485–488.

[103] Miyata, M. Centipede and inchworm models to explain *Mycoplasma* gliding. *Trends Microbiol 16*, 1 (Jan 2008), 6–12.

[104] Nakamoto, R. K., Scanlon, J. A. B., and Al-Shawi, M. K. The rotary mechanism of the ATP synthase. *Arch Biochem Biophys 476*, 1 (Aug 2008), 43–50.

[105] Nan, B., Chen, J., Neu, J. C., Berry, R. M., Oster, G., and Zusman, D. R. *Myxobacteria* gliding motility requires cytoskeleton rotation powered by proton motive force. *Proc Natl Acad Sci USA 108*, 6 (Feb 2011), 2498–2503.

[106] Ng, S. Y., Chaban, B., and Jarrell, K. F. Archaeal flagella, bacterial flagella and type IV pili: A comparison of genes and posttranslational modifications. *J Mol Microbiol Biotechnol 11*, 3-5 (Jan 2006), 167–191.

[107] Nicholls, D. G., and Ferguson, S. J. *Bioenergetics*, 3rd ed. Academic Press, 2002.

[108] Ottemann, K. M., and Lowenthal, A. C. *Helicobacter pylori* uses motility for initial colonization and to attain robust infection. *Infect Immun 70*, 4 (Apr 2002), 1984–90.

[109] Pallen, M. J., and Matzke, N. J. From the origin of species to the origin of bacterial flagella. *Nature reviews Microbiology 4*, 10 (Oct 2006), 784–790.

[110] Pallen, M. J., Penn, C. W., and Chaudhuri, R. R. Bacterial flagellar diversity in the post-genomic era. *Trends Microbiol 13*, 4 (Apr 2005), 143–9.

[111] Park, S.-Y., Lowder, B., Bilwes, A. M., Blair, D. F., and Crane, B. R. Structure of FliM provides insight into assembly of the switch complex in the bacterial flagella motor. *Proc Natl Acad Sci USA 103*, 32 (Aug 2006), 11886–91.

[112] Parkinson, J. Complementation analysis and deletion mapping of *Escherichia coli* mutants defective in chemotaxis. *Journal of Bacteriology 135* (Jan 1978), 45–53.

[113] Paul, K., and Blair, D. F. Organization of FliN subunits in the flagellar motor of *Escherichia coli*. *J Bacteriol 188*, 7 (Apr 2006), 2502–11.

[114] Paul, K., Brunstetter, D., Titen, S., and Blair, D. A molecular mechanism of direction switching in the flagellar motor of Escherichia coli. *Proceedings of the National Academy of Sciences 108*, 41 (Oct 2011), 17171–17176. 10.1073/pnas.1110111108.

[115] Paul, K., Erhardt, M., Hirano, T., Blair, D. F., and Hughes, K. T. Energy source of flagellar typeIII secretion. *Nature 451*, 7177 (Jan 2008), 489–492.

[116] Paul, K., Nieto, V., Carlquist, W. C., Blair, D. F., and Harshey, R. M. The c-di-GMP binding protein YcgR controls flagellar motor direction and speed to affect chemotaxis by a "backstop brake" mechanism. *Mol Cell 38*, 1 (Apr 2010), 128–39.

[117] Paulick, A., Koerdt, A., Lassak, J., Huntley, S., Wilms, I., Narberhaus, F., and Thormann, K. M. Two different stator systems drive a single polar flagellum in *Shewanella oneidensis* mr-1. *Molecular Microbiology 71*, 4 (Feb 2009), 836–850.

[118] Philippe, N., Alcaraz, J.-P., Coursange, E., Geiselmann, J., and Schneider, D. Improvement of pCVD442, a suicide plasmid for gene allele exchange in bacteria. *Plasmid 51*, 3 (May 2004), 246–55.

[119] Pilizota, T. *A programmable optical angle clamp for rotary molecular motors*. PhD thesis, University of Oxford, 2006.

[120] Pilizota, T., Brown, M. T., Leake, M. C., Branch, R. W., Berry, R. M., and Armitage, J. P. A molecular brake, not a clutch, stops the *Rhodobacter sphaeroides* flagellar motor. *Proc Natl Acad Sci USA 106*, 28 (Jul 2009), 11582–7.

[121] Pohlschroder, M., Ghosh, A., Tripepi, M., and Albers, S.-V. Archaeal type IV pilus-like structures - evolutionarily conserved prokaryotic surface organelles. *Current Opinion in Microbiology 14* (Apr 2011), 357–363.

[122] Porter, S. L., Wadhams, G. H., and Armitage, J. P. *Rhodobacter sphaeroides*: complexity in chemotactic signalling. *Trends Microbiol 16*, 6 (Jun 2008), 251–60.

[123] Porter, S. L., Wadhams, G. H., and Armitage, J. P. Signal processing in complex chemotaxis pathways. *Nature reviews Microbiology* (Feb 2011).

[124] Purcell, E. Life at low Reynolds number. *Am. J. Phys* (Jan 1977).

[125] Reid, S. W., Leake, M. C., Chandler, J. H., Lo, C.-J., Armitage, J. P., and Berry, R. M. The maximum number of torque-generating units in the flagellar motor of *Escherichia coli* is at least 11. *Proc Natl Acad Sci USA 103*, 21 (May 2006), 8066–71.

[126] Rowe, A. D. *Rotation of the sodium-driven bacterial flagellar motor.* PhD thesis, University of Oxford, 2005.

[127] Rowe, A. D., Leake, M. C., Morgan, H., and Berry, R. M. Rapid rotation of micron and submicron dielectric particles measured using optical tweezers. *Journal of Modern Optics 50*, 10 (Jan 2003), 1539–1554.

[128] Royant, A., and Noirclerc-Savoye, M. Stabilizing role of glutamic acid 222 in the structure of enhanced green fluorescent protein. *Journal of Structural Biology 174*, 2 (May 2011), 385–390.

[129] Ryu, W. S., Berry, R. M., and Berg, H. C. Torque-generating units of the flagellar motor of *Escherichia coli* have a high duty ratio. *Nature 403*, 6768 (Jan 2000), 444–7.

[130] Sabehi, G., Massana, R., Bielawski, J. P., Rosenberg, M., Delong, E. F., and Béjà, O. Novel proteorhodopsin variants from the Mediterranean and Red Seas. *Environ Microbiol 5*, 10 (Oct 2003), 842–9.

[131] Sako, Y., and Uyemura, T. Total internal reflection fluorescence microscopy for single-molecule imaging in living cells. *Cell Struct Funct 27*, 5 (Oct 2002), 357–65.

[132] Sambrook, J., and Russell, D. *Molecular cloning: a laboratory manual*, 3rd ed. Cold Spring Harbor Laboratory Press, 2001.

[133] Sato, K., and Homma, M. Functional reconstitution of the Na^+-driven polar flagellar motor component of *Vibrio alginolyticus*. *Journal of Biological Chemistry 275*, 8 (Feb 2000), 5718–5722. 10.1074/jbc.275.8.5718.

[134] Schmitt, R. Helix rotation model of the flagellar rotary motor. *Biophys J 85*, 2 (Dec 2003), 843–852.

[135] Segall, J. E., Block, S. M., and Berg, H. C. Temporal comparisons in bacterial chemotaxis. *Proc Natl Acad Sci USA 83*, 23 (Dec 1986), 8987–91.

[136] Shaner, N. C., Steinbach, P. A., and Tsien, R. Y. A guide to choosing fluorescent proteins. *Nature Methods 2*, 12 (Dec 2005), 905–909.

[137] Shestopalov, A. I., Bogachev, A. V., Murtazina, R. A., Viryasov, M. B., and Skulachev, V. P. Aeration-dependent changes in composition of the quinone pool in *Escherichia coli*. Evidence of post-transcriptional regulation of the quinone biosynthesis. *FEBS Lett 404*, 2-3 (Mar 1997), 272–4.

[138] Shimomura, O. The discovery of aequorin and green fluorescent protein. *J Microsc 217*, Pt 1 (Jan 2005), 1–15.

[139] Siegel, M. S., and Isacoff, E. Y. A genetically encoded optical probe of membrane voltage. *Neuron 19*, 4 (Oct 1997), 735–41.

[140] Silversmith, R. E. Auxiliary phosphatases in two-component signal transduction. *Current Opinion in Microbiology 13*, 2 (Apr 2010), 177–183.

[141] Slamovits, C. H., Okamoto, N., Burri, L., James, E. R., and Keeling, P. J. A bacterial proteorhodopsin proton pump in marine eukaryotes. *Nature Communications 2* (Feb 2011), 183–6.

[142] Sourjik, V., and Berg, H. C. Receptor sensitivity in bacterial chemotaxis. *Proc Natl Acad Sci USA 99*, 1 (Jan 2002), 123–7.

[143] Sowa, Y., and Berry, R. M. Bacterial flagellar motor. *Q Rev Biophys 41*, 2 (May 2008), 103–32.

[144] Sowa, Y., Hotta, H., Homma, M., and Ishijima, A. Torque-speed relationship of the Na^+-driven flagellar motor of *Vibrio alginolyticus*. *J Mol Biol 327*, 5 (Apr 2003), 1043–51.

[145] Sowa, Y., Rowe, A. D., Leake, M. C., Yakushi, T., Homma, M., Ishijima, A., and Berry, R. M. Direct observation of steps in rotation of the bacterial flagellar motor. *Nature 437*, 7060 (Oct 2005), 916–9.

[146] Spormann, A. M. Gliding motility in bacteria: insights from studies of *Myxococcus xanthus*. *Microbiology and Molecular Biology Reviews 63*, 3 (Sep 1999), 621–41.

[147] Spudich, J. L. The multitalented microbial sensory rhodopsins. *Trends Microbiol 14*, 11 (Nov 2006), 480–7.

[148] Stolz, B., and Berg, H. C. Evidence for interactions between MotA and MotB, torque-generating elements of the flagellar motor of *Escherichia coli*. *Journal of Bacteriology 173*, 21 (Nov 1991), 7033–7.

[149] Streif, S., Staudinger, W. F., Marwan, W., and Oesterhelt, D. Flagellar rotation in the archaeon *Halobacterium salinarum* depends on ATP. *J Mol Biol 384*, 1 (Dec 2008), 1–8.

[150] Sun, M., Wartel, M., Cascales, E., Shaevitz, J. W., and Mignot, T. Motor-driven intracellular transport powers bacterial gliding motility. *Proc Natl Acad Sci USA 108*, 18 (May 2011), 7559–7564.

[151] Suzuki, H., Yonekura, K., and Namba, K. Structure of the rotor of the bacterial flagellar motor revealed by electron cryomicroscopy and single-particle image analysis. *J Mol Biol 337*, 1 (Mar 2004), 105–13.

[152] Szabo, Z., Sani, M., Groeneveld, M., Zolghadr, B., Schelert, J., Albers, S.-V., Blum, P., Boekema, E. J., and Driessen, A. J. M. Flagellar motility and structure in the hyperthermoacidophilic archaeon *Sulfolobus solfataricus*. *J Bacteriol 189*, 11 (Jun 2007), 4305–4309.

[153] Terahara, N., Krulwich, T. A., and Ito, M. Mutations alter the sodium versus proton use of a *Bacillus clausii* flagellar motor and confer dual ion use on bacillus subtilis motors. *Proc Natl Acad Sci USA 105*, 38 (Sep 2008), 14359–64.

[154] Terashima, H., Fukuoka, H., Yakushi, T., Kojima, S., and Homma, M. The *Vibrio* motor proteins, MotX and MotY, are associated with the basal body of Na^+-driven flagella and required for stator formation. *Molecular Microbiology 62*, 4 (Nov 2006), 1170–1180.

[155] Thomas, N. A., Bardy, S. L., and Jarrell, K. F. The archaeal flagellum: a different kind of prokaryotic motility structure. *FEMS Microbiol Rev 25*, 2 (Apr 2001), 147–74.

[156] Thomas, N. A., Chao, E. D., and Jarrell, K. F. Identification of amino acids in the leader peptide of *Methanococcus voltae* preflagellin that

are important in posttranslational processing. *Archives of Microbiology 175*, 4 (Apr 2001), 263–269.

[157] Turner, L., Ryu, W. S., and Berg, H. C. Real-time imaging of fluorescent flagellar filaments. *J Bacteriol 182*, 10 (May 2000), 2793–801.

[158] Unden, G., and Bongaerts, J. Alternative respiratory pathways of *Escherichia coli*: energetics and transcriptional regulation in response to electron acceptors. *Biochim Biophys Acta 1320*, 3 (Jul 1997), 217–34.

[159] Vladimirov, N., and Sourjik, V. Chemotaxis: how bacteria use memory. *Biological Chemistry 390*, 11 (Nov 2009), 1097–1104.

[160] Wadhams, G. H., and Sowa, Y. Bacteria flagella: Flagella motor. *eLS* (September 2009).

[161] Walter, J. M., Greenfield, D., Bustamante, C., and Liphardt, J. Light-powering *Escherichia coli* with proteorhodopsin. *Proc Natl Acad Sci USA 104*, 7 (Feb 2007), 2408–12.

[162] Walz, D., and Caplan, S. R. An electrostatic mechanism closely reproducing observed behavior in the bacterial flagellar motor. *Biophys J 78*, 2 (Feb 2000), 626–51.

[163] West, I. C., and Mitchell, P. Proton/sodium ion antiport in *Escherichia coli*. *Biochem J 144*, 1 (Oct 1974), 87–90.

[164] Wood, T. K., Barrios, A. F. G., Herzberg, M., and Lee, J. Motility influences biofilm architecture in *Escherichia coli*. *Appl Microbiol Biotechnol 72*, 2 (Sep 2006), 361–367.

[165] Xing, J., Bai, F., Berry, R., and Oster, G. Torque-speed relationship of the bacterial flagellar motor. *Proc Natl Acad Sci USA 103*, 5 (Jan 2006), 1260–5.

[166] Yakushi, T., Yang, J., Fukuoka, H., Homma, M., and Blair, D. F. Roles of charged residues of rotor and stator in flagellar rotation: comparative study using H^+-driven and Na^+-driven motors in *Escherichia coli*. *Journal of Bacteriology 188*, 4 (Feb 2006), 1466–72.

[167] Yang, F., Moss, L. G., and Phillips, G. N. The molecular structure of green fluorescent protein. *Nat Biotechnol 14*, 10 (Oct 1996), 1246–51.

[168] Yonekura, K., Maki, S., Morgan, D. G., DeRosier, D., Vonderviszt, F., Imada, K., and Namba, K. The bacterial flagellar cap as the rotary promoter of flagellin self-assembly. *Science 290*, 5499 (Dec 2000), 2148–2152.

[169] Yonekura, K., Maki-Yonekura, S., and Namba, K. Complete atomic model of the bacterial flagellar filament by electron cryomicroscopy. *Nature 424*, 6949 (Aug 2003), 643–50.

[170] Youderian, P., Burke, N., White, D. J., and Hartzell, P. L. Identification of genes required for adventurous gliding motility in *Myxococcus xanthus* with the transposable element mariner. *Mol Microbiol 49*, 2 (Jun 2003), 555–570.

[171] Young, G. M., Schmiel, D. H., and Miller, V. L. A new pathway for the secretion of virulence factors by bacteria: the flagellar export apparatus functions as a protein-secretion system. *Proc Natl Acad Sci USA 96*, 11 (May 1999), 6456–61.

[172] Yuan, J., and Berg, H. C. Resurrection of the flagellar rotary motor near zero load. *Proc Natl Acad Sci USA 105*, 4 (Jan 2008), 1182–5.

[173] Yuan, J., Fahrner, K. A., Turner, L., and Berg, H. C. Asymmetry in the clockwise and counterclockwise rotation of the bacterial flagellar motor. *Proc Natl Acad Sci USA 107*, 29 (Jul 2010), 12846–9.

[174] Zhai, Y. F., Heijne, W., and Saier, M. H. Molecular modeling of the bacterial outer membrane receptor energizer, ExbBD/TonB, based on homology with the flagellar motor, MotAB. *Biochim Biophys Acta 1614*, 2 (Aug 2003), 201–10.

[175] Zhang, P., Khursigara, C. M., Hartnell, L. M., and Subramaniam, S. Direct visualization of *Escherichia coli* chemotaxis receptor arrays using cryo-electron microscopy. *Proc Natl Acad Sci USA 104*, 10 (Mar 2007), 3777–81.

[176] Zhou, J., Lloyd, S. A., and Blair, D. F. Electrostatic interactions between rotor and stator in the bacterial flagellar motor. *Proc Natl Acad Sci USA 95*, 11 (May 1998), 6436–41.

[177] Zhou, J., Sharp, L. L., Tang, H. L., Lloyd, S. A., Billings, S., Braun, T. F., and Blair, D. F. Function of protonatable residues in the flagellar motor of *Escherichia coli*: a critical role for Asp32 of MotB. *Journal of Bacteriology 180*, 10 (May 1998), 2729–35.

[178] Zolghadr, B., Klingl, A., Koerdt, A., Driessen, A. J. M., Rachel, R., and Albers, S.-V. Appendage-mediated surface adherence of *Sulfolobus solfataricus*. *J Bacteriol 192*, 1 (Jan 2010), 104–110.

Appendix A

Media Recipes and Reagents

LB-Broth

Bacto-tryptone 10 g l^{-1}
Yeast extract 5 g l^{-1}
NaCl 5 g l^{-1}
pH 7.0

LB Agar (LBA)

Bacto-tryptone 10 g l^{-1}
Yeast extract 5 g l^{-1}
NaCl 5 g l^{-1}
Agar 20 g l^{-1}
pH 7.0

Tryptone Broth(TB)

Bacto-tryptone 10 g l^{-1}
NaCl 5 g l^{-1}

E. coli Motility Buffer

Potassium phosphate 10 mM
EDTA 0.1 mM
pH 7.0

SOB medium

NaCl 0.5 g l^{-1}
Bacto-tryptone 20 g l^{-1}
Yeast extract 5 g l^{-1}

SOC Medium

Glucose 20 mM
MgCl 10 mM
$MgSO_4$ 10 mM
NaCl 10 mM
Bacto-tryptone 20 g l^{-1}
Yeast extract 5 g l^{-1}
pH 7.0

TFB I

KCH_3COO 30 mM
RbCl 100 mM
$CaCl_2 \cdot 2\,H_2O$ 10 mM
$MnCl_2 \cdot 4\,H_2O$ 50 mM
Glycerol 15 % (v/v)
pH to 5.8 by adding 0.2 M acetic acid, then filter sterilise

TFB II

PIPES 10 mM
$CaCl_2 \cdot 2\,H_2O$ 75 mM
$RbCl_2$ 10 mM
Glycerol 15 % (v/v)
pH to 6.8 by adding 0.1 M HCl, then filter sterlise

10 × TBE (for DNA electrophoresis)

TRIS base 108 g l^{-1}
Boric acid 55 g l^{-1}
EDTA 7.4 g l^{-1}
pH 8.3

5 × DNA loading dye (for DNA electrophoresis)

Glycerol 70 % (w/v)
TRIS base 30 % (w/v)
Bromophenol blue 0.25 % (w/v)
Xylene cyanol 0.25 % (w/v)

Appendix B

Primer Sequences

Name	**Sequence**	**Restriction Site**
fliCst1	GCGCGAGCTCTGCTGCTGGTGGTGCTGG	*Sac*I
fliCst2	GCGCGCATGCGTCATAGCGTTCGACG	*Sph*I
pRpQE1	GCGTCCATGGGTAAATTATTACTG	*Nco*I
pRpQE2	GCGCAGATCTACCGGTACGCGTAGAATCGAG	*Xba*I
pRpBAD1	GCGTCCATGGGTAAATTATTACTG	*Nco*I
pRpBAD2	GCGTGGTACCACCGGTACGCGTAGAATCGAG	*Kpn*I
gfp-mota1	GCGTCCATGGCGTTCATGCTTCGATGTTCTG	*Sph*I
gfp-mota2	CAGCTCCTCGCCCTTGCTCACGTCGCTCCAAATACACCAAA	-
gpf-mota3	TTTGGTGTATTTGGAGCGACGTGAGCAAGGGCGAGGAGCTG	-
gfp-mota4	CCAGCAGATCCATATACATTGCCTTGTACAGCTCGTCCATGCCG	-
gfp-mota5	CGGCATGGACGAGCTGTACAAGGCAATGTATATGGATCTGCTGG	-
gfp-mota6	GCGTGAGCTCGACATCGGCACTGCCGGTTC	*Sac*I

Table B.1: Primer sequences used in this project. Restriction sites are underlined.

Appendix C

Supplementary Data

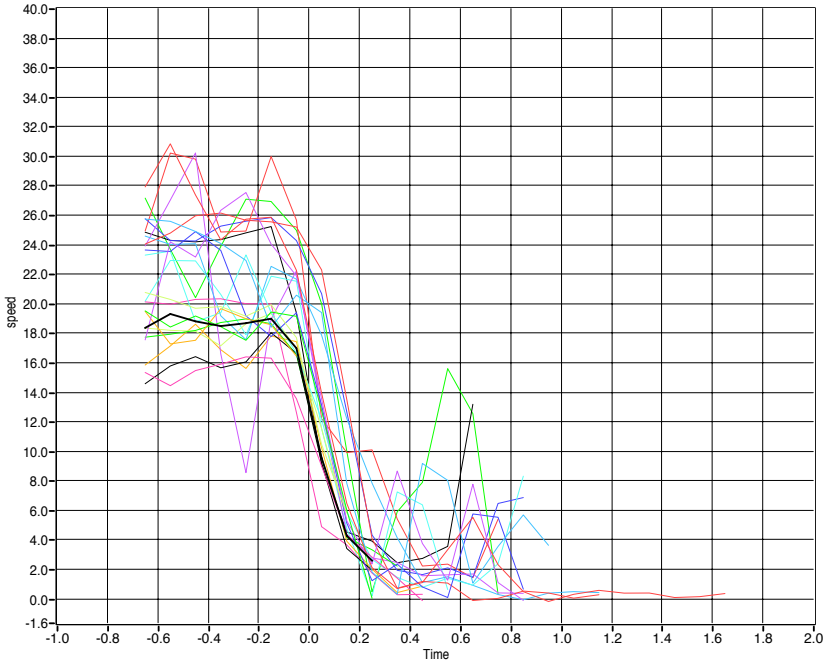


Figure C.1: A collection of 24 speed/time traces, showing motor slowdown after illumination stop in cells which had been illuminated for > 15 minutes after addition of azide.

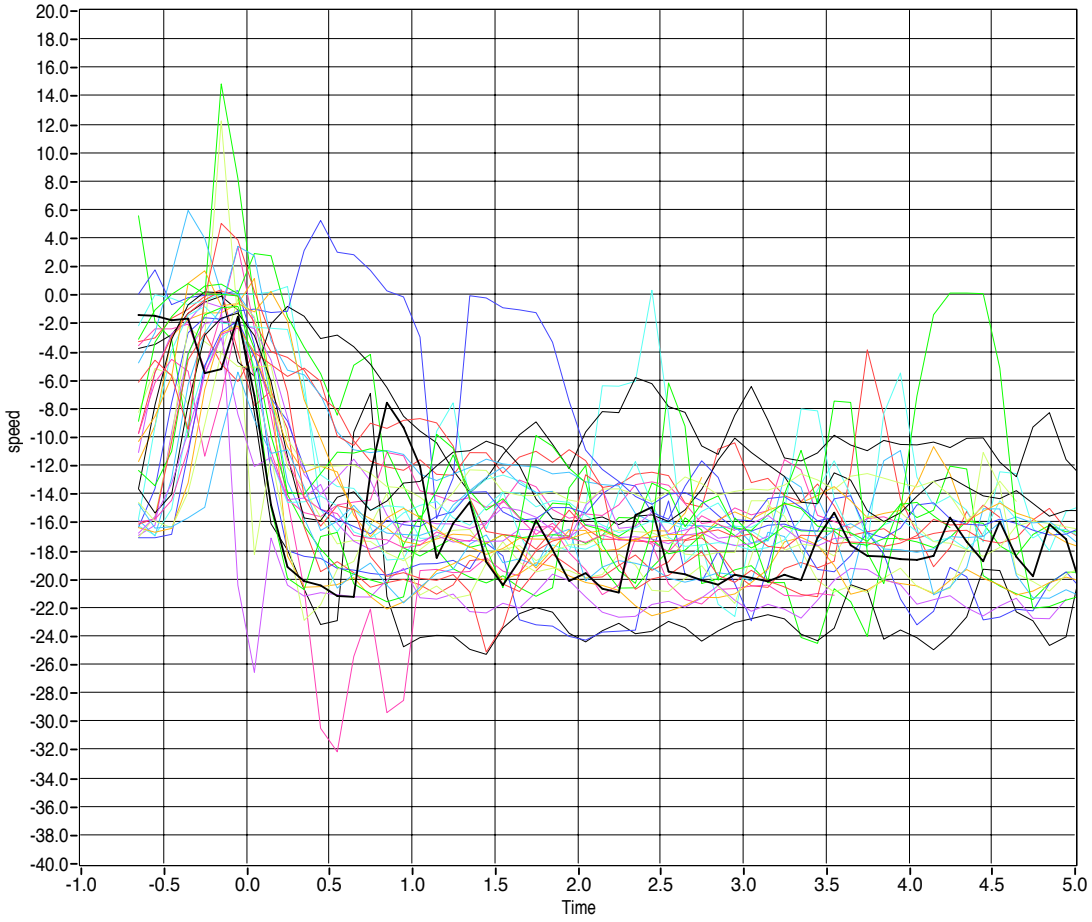


Figure C.2: A collection of 28 speed/time traces of motor speedup in cells which had been subjected to short times (< 1 s) at a zero-*pmf* regime.

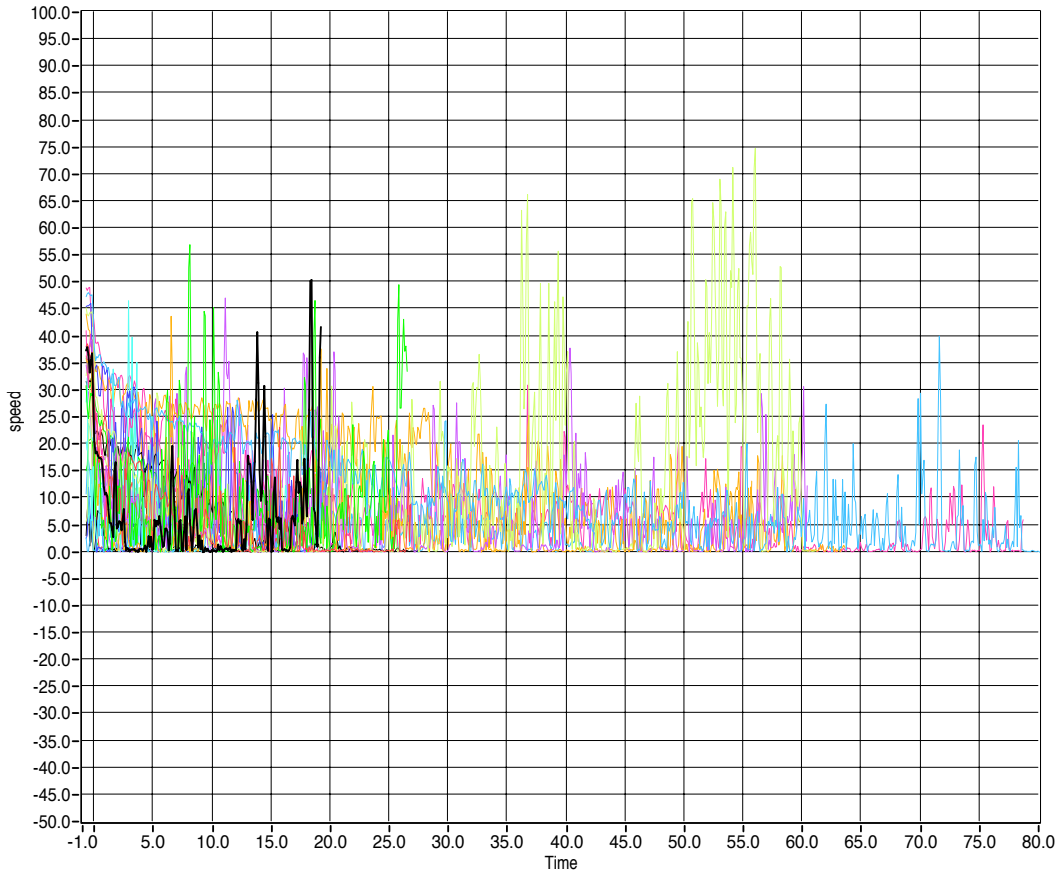


Figure C.3: A collection of 27 speed/time traces, showing motor slowdown after illumination stop in cells which had been illuminated for < 1 minute after addition of azide

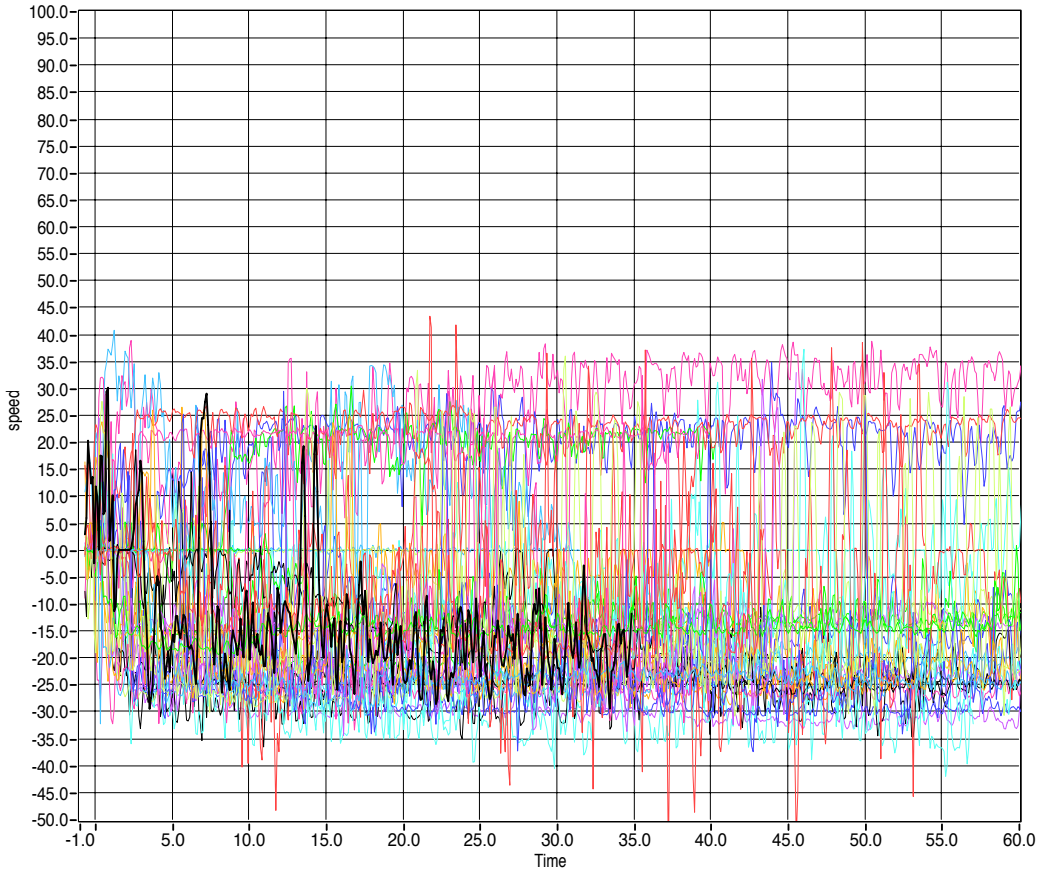


Figure C.4: A collection of 37 speed/time traces of motor speedup in cells which had been subjected to more than 20 s at a zero-*pmf* regime. Positive and negative speeds are due to use of the bidirectional strain MT02.